

# The modern era of light kaonic atom experiments

Catalina Curceanu,\* Carlo Guaraldo, and Mihail Iliescu

*INFN, Laboratori Nazionali di Frascati, CP 13, Via E. Fermi 40, I-00044, Frascati (Roma), Italy*

Michael Cargnelli, Ryugo Hayano, Johann Marton, and Johann Zmeskal

*Stefan Meyer Institute for Subatomic Physics, Boltzmannngasse 3, A-1090 Vienna, Austria*

Tomoichi Ishiwatari

*I's factory, Muneyasu 2nd building, 1-33 Kanda-Nishikicho Chiyoda, Tokyo, Japan*

Masa Iwasaki and Shinji Okada

*RIKEN, Institute of Physical and Chemical Research, 2-1 Hirosawa, Wako, Saitama 351-0198, Japan*

Diana Laura Sirghi

*INFN, Laboratori Nazionali di Frascati, CP 13, Via E. Fermi 40, I-00044, Frascati (Roma), Italy and Horia Hulubei National Institute of Physics and Nuclear Engineering (IFIN-HH), Str. Reactorului no. 30, P.O. BOX MG-6, Bucharest - Magurele, Romania*

Hideyuki Tatsuno

*Lund Univeristy, Box 117, SE-221 00, Lund, Sweden*

 (published 20 June 2019)

This review covers the modern era of experimental kaonic atom studies, encompassing 20 years of activity, defined by breakthroughs in technological developments which allowed performing a series of long-awaited precision measurements. Kaonic atoms are atomic systems where an electron is replaced by a negatively charged kaon, containing the strange quark, which interacts in the lowest orbits with the nucleus also by the strong interaction. As a result, their study offers the unique opportunity to perform experiments equivalent to scattering at vanishing relative energy. This allows one to study the strong interaction between the antikaon and the nucleon or the nucleus “at threshold,” namely, at zero relative energy, without the need of *ad hoc* extrapolation to zero energy, as in scattering experiments. The fast progress achieved in performing precision light kaonic atom experiments, which also solved long-pending inconsistencies with theoretical calculations generated by old measurements, relies on the development of novel cryogenic targets, x-ray detectors, and the availability of pure and intense charged kaon beams, which propelled an unprecedented progress in the field. Future experiments, based on new undergoing technological developments, will further boost the kaonic atom studies, thus fostering a deeper understanding of the low-energy strong interaction extended to the second family of quarks.

DOI: [10.1103/RevModPhys.91.025006](https://doi.org/10.1103/RevModPhys.91.025006)

## CONTENTS

I. Introduction	2	a. Beam production scheme	7
II. The Physics of Light Kaonic Atoms	4	b. Kaon production scheme:	
A. Exotic atoms	4	The K1.8 beam lines	7
B. Formation of exotic atoms	4	B. Target systems for light kaonic atoms	8
C. Study of strong-interaction effects in kaonic atoms	5	C. Advances in exotic atom x-ray detection:	
III. Antikaon Sources, Targets, and Detector Developments	6	From charge-coupled devices to silicon drift detectors	9
A. Antikaon sources	6	1. Charge-coupled devices	9
1. DAΦNE at Laboratori Nazionali di Frascati of INFN	6	2. Silicon drift detectors	10
2. Japan Proton Accelerator Research Complex	7	3. SDDs with implanted junction gate field-effect transistor (JFET)	10
		4. New monolithic SDD arrays	11
		IV. The Experimental Results in the Modern Era	11
		A. The beginning of the modern era: The “kaonic-hydrogen puzzle” and its solution	11

\*Catalina.Curceanu@lnf.infn.it

1. The kaonic-hydrogen puzzle	11
2. The KpX kaonic-hydrogen measurement at KEK	12
3. The DEAR experiment at DAΦNE	13
a. Kaonic-hydrogen measurement	13
b. Kaonic nitrogen measurement	16
B. Light kaonic atom precision measurements	17
1. The E570 experiment at KEK 12 GeV-PS	17
a. The kaonic helium discrepancy	17
b. The kaonic-helium measurement	17
2. The SIDDHARTA experiment at DAΦNE	19
a. Kaonic-hydrogen measurement	19
b. Kaonic helium-3 and helium-4 measurements	22
c. First exploratory measurement of kaonic deuterium	24
C. Atomic physics results	25
1. Kaonic-hydrogen $K$ -series transition yields measurements by KpX and SIDDHARTA	25
2. Kaonic deuterium transition yields measurement by SIDDHARTA	26
3. Kaonic helium-4 and helium-3 transition yield measurements by SIDDHARTA	26
4. Kaonic nitrogen transition yield measurement by DEAR	26
V. Planned Experiments	28
A. Kaonic deuterium	28
1. Experimental requirements for kaonic deuterium experiments	28
a. Large area x-ray detector system	28
b. Lightweight cryogenic target	28
c. The SIDDHARTA-2 veto system	28
d. The E57 veto system	29
2. The SIDDHARTA-2 experiment at DAΦNE	29
3. The E57 experiment at J-PARC	30
B. Ultrahigh precision x-ray kaonic atom spectroscopy	30
1. The E62 experiment at J-PARC	30
C. Shift and width of the $1s$ state of kaonic helium-3 and kaonic helium-4	33
VI. Conclusions and Outlook	33
A. Achievements in the modern era	34
B. Outlook	34
1. First measurement of kaonic deuterium	34
2. Ultra-high-precision measurement of kaonic helium-3 and kaonic helium-4	34
3. First measurements of shifts and widths of the $1s$ state in kaonic helium-3 and kaonic helium-4	35
Acknowledgments	35
References	35

## I. INTRODUCTION

Exotic atoms were predicted already in the 1940s (Tomonaga and Araki, 1940; Conversi, Pancini, and Piccioni, 1945, 1947; Fermi and Teller, 1947) and their studies provided a wealth of experimental data which fostered a deeper understanding of particle and nuclear physics and a continuous refinement of the related theories. An exotic atom is an atomic system where an electron is replaced by a negatively charged particle, which could be a muon, a pion, a kaon, an antiproton, or a sigma hyperon, bound into an atomic orbit by its electromagnetic (e.m.) interaction with the nucleus.

Among exotic atoms, the hadronic ones, in which the electron is replaced by a hadron, a particle built up by quarks, play a unique role, since their study allows one to experimentally investigate the strong interaction, described by the quantum chromodynamics (QCD). The interaction is measured at threshold, since the relative energy between the hadron forming the exotic atoms and the nucleus is so small that it can be, for any practical purpose, neglected. In this context, the kaonic atoms are a special case, since by studying them one can access the strong interaction of particles with strangeness, keeping in mind that the kaon contains the strange quark. Experiments with kaonic atoms are the only way to measure the strong interaction at threshold between antikaons and nucleons, by extracting the antikaon-nucleon scattering lengths, fundamental quantities for the low-energy QCD with strangeness.

A kaonic atom is formed when a kaon stops in a target and replaces the electron of an atom of the target. The kaon is captured in a highly excited quantum state, due to its mass much larger than the electron one. The kaonic atom experiences then a series of deexcitation processes, which bring the kaon to the ground state. These processes are accompanied by the emission of radiation which, for the transitions to the lowest lying levels, is in the x-ray energy domain. Not all kaons reach the fundamental level since, depending on the target density, other processes compete and may substantially reduce the yield of the transitions to the fundamental level. Among these competing processes the Stark effect, mixing levels with the same principal quantum number, which increases with the density, results in a dramatic reduction of the yield at high target densities.

When the kaon reaches the fundamental level of the kaonic atom, its wave function and that of the nucleus are overlapping so the kaon and the nucleus interact by the strong interaction: QCD comes into play. The main effect of the presence of the strong interaction on top of the electromagnetic one is a shift of the energy level with respect to the electromagnetically calculated value and a broadening of the level. The broadening, seen as an increased width of the transition line, implies a limited lifetime of the kaonic atom and is due to the absorption of the kaon by the nucleus as a consequence of the strong interaction. Measurement of the x-ray transitions toward the lowest lying states allows one to measure the shift and the width of the levels, which are entirely caused by the strong interaction between the kaon and the nucleus at threshold. The experimental quantities, shifts and widths, measured for the lightest kaonic atoms, namely, kaonic hydrogen and kaonic deuterium, are then used to determine the isospin-dependent antikaon-nucleon scattering lengths, fundamental quantities for a better understanding of the QCD in the nonperturbative regime with strangeness.

The importance of light kaonic atom measurements was recognized a long time ago. While the experimental studies of similar pionic atoms had already started in the 1950s (Camac *et al.*, 1952) and high-precision experiments in this sector had been performed throughout the years (Bird *et al.*, 1983; Chatellard *et al.*, 1997; Hauser *et al.*, 1998), the kaonic atom experiments had a much more complicated beginning. The challenge of performing kaonic atom measurements reflects the difficulty to produce kaon beams which can be stopped in a target and form kaonic atoms, on the one side, and the lack

of suitable experimental technologies, in terms of x-ray detectors with good energy and timing resolutions and high-density cryogenic gaseous targets, on the other side.

Experiments measuring kaonic atoms, in particular, kaonic hydrogen, performed in the 1970s through the 1980s (Davies *et al.*, 1979; Izycki *et al.*, 1980; Bird *et al.*, 1983) have left the scientific community with a huge problem, also known as the “kaonic-hydrogen puzzle”: the measured strong-interaction shift of the fundamental level with respect to the electromagnetic calculated value was positive, the level resulting more bound than the electromagnetic binding energy, which meant an attractive-type strong interaction at threshold between the kaon and the proton. This was in striking contradiction with the results of the analyses of low-energy scattering data which found a repulsive-type strong interaction. An analogous inconsistency was verified for kaonic helium, where the measured transitions to the  $2p$  level showed, in this case, a large shift with respect to the electromagnetic value, while theories predicted a shift which, if any, should be extremely small. It was clear to all involved that new measurements of light kaonic atoms employing new technologies were mandatory to solve these ambiguous situations and to finally allow real progress in the field.

In the last 20 years, defining the modern era, a breakthrough in the technologies for studies of kaonic atoms was achieved, which finally allowed one to make real and steady progress in the field.

New technological developments in accelerators delivering kaon beams materialized in the construction of the Double Annular  $\Phi$  Factory for Nice Experiments (DAΦNE) collider at the Frascati National Laboratories of INFN (LNF-INFN) in Italy, and in the kaon extracted beams in Japan, first at the High Energy Accelerator Research Organization (KEK) and then at the Japan Proton Accelerator Research Complex (J-PARC). The availability of the new kaon beams with excellent characteristics for the studies of kaonic atoms was the first necessary ingredient toward the progress in kaonic atom studies in the modern era.

DAΦNE provides a source of charged kaons generated by the decay of the  $\phi$  resonance formed in the collisions of electrons and positrons beams. The kaons have very low momenta (127 MeV/ $c$ ) and low-energy spread, making the beam ideal to be stopped in gaseous targets and to form, with high efficiency, kaonic atoms. KEK and J-PARC are delivering high-intensity, high-energy kaon beams which can also be stopped in targets to form kaonic atoms (see Sec. III).

In parallel with the delivery of these new kaon beams, equal effort has been put into the development of lightweight gaseous high-density cryogenic targets, to avoid the Stark effect, and of new high performance x-ray detectors able to measure the weak signal of kaonic atoms over a large background. A series of solid state detectors, going from silicon (lithium) detectors to charge-coupled devices (CCDs) and, more recently, to fast silicon drift detectors (SSDs) with timing capabilities, specially developed for kaonic atoms spectroscopy, were used in the experiments performed at DAΦNE and KEK (J-PARC) in the modern era of kaonic atom research.

With the new technologies and kaon beams, steady progress was achieved that allowed one to perform experiments which measured, with unparalleled precision, the kaonic-hydrogen

transitions, solving the kaonic-hydrogen puzzle, in a series of measurements performed first at KEK, the KpX experiment (Iwasaki *et al.*, 1997), then at DAΦNE, DEAR (DAΦNE exotic atom research) (Beer *et al.*, 2005), and SIDDHARTA (silicon drift detector for timing applications) (Bazzi *et al.*, 2011a). Other light kaonic atoms were also measured with high precision, such as kaonic helium-4, also in this case solving the inconsistencies resulting from old experiments, kaonic helium-3 (the first measurements ever), and other low- $Z$  kaonic atom transitions, which contributed to the understanding of the atomic cascade processes in kaonic atoms. These new measurements are cornerstones for any theory which is dealing with strong-interaction effects in the strangeness sector.

In spite of the significant progress achieved in the last 20 years, the kaonic deuterium measurement, the most wanted one in the field of low-energy kaon-nucleon interaction studies, could not yet be performed. The SIDDHARTA experiment at the DAΦNE collider succeeded, in a test experiment, to set an upper limit on its yield. The kaonic deuterium measurement is extremely difficult, since the yield of the last transition to the fundamental level is at least 10 times lower than the corresponding one in kaonic hydrogen and, moreover, the transition line is at least twice as broad. In a reasonable experimental approach one expects about ten kaonic deuterium x rays per day embedded in a large accelerator background, which needs to be drastically reduced. To perform the kaonic deuterium measurement further technological progress had to be achieved. New strategies were followed in the last years, consisting of the development of dedicated new silicon drift detectors with a time response and characteristics superior to any other detector used so far in kaonic atom measurements. These improved detectors allow the efficient use of special veto systems for a dramatic background reduction. At the same time, new cryogenic techniques have been exploited to build a high-density cryogenic gaseous deuterium target, where kaons are efficiently stopped. The new technological developments will foster a breakthrough in the field, which will finally allow one in the coming years to perform the first measurement of kaonic deuterium, indispensable in extracting the antikaon-nucleon isospin-dependent scattering lengths.

In parallel, a new type of detector technology has been developed, the transition edge sensors, for extreme precision x-ray measurements. These detectors work on a calorimeter principle, based on a phase transition in a superconducting material, achieving unprecedented energy resolution for particles (in our case x rays) passing through the detector. They will be used to perform measurements of kaonic atom transitions with sub-eV precision, which are important to fully understand the strong interaction between kaons and nuclei.

In conclusion, the last 20 years of kaonic atom precision measurements mark the modern era of kaonic atom experiments and set new constraints on theories which deal with low-energy QCD in the strangeness sector. The future of this sector will further boost a deeper understanding of the “strangeness physics” in the nonperturbative regime of QCD, with implications from particle and nuclear physics to astrophysics, for better knowledge of the way in which nature works.

## II. THE PHYSICS OF LIGHT KAONIC ATOMS

### A. Exotic atoms

By exotic atom one means any system in which a negatively charged particle heavier than an electron—a muon, a pion, a kaon, an antiproton, a sigma hyperon—is bound into an atomic orbit by its electromagnetic interaction with the nucleus. Exotic atoms formed with muons are subject to the weak interaction, while for all other exotic atoms the strong interaction is also involved.

Predicted in the 1940s (Tomonaga and Araki, 1940; Conversi, Pancini, and Piccioni, 1945, 1947; Fermi and Teller, 1947) the existence of exotic atoms was first established by the observation of Auger electrons in photographic emulsions (Fry, 1951). Characteristic x rays from pionic and muonic atoms were identified for the first time in the early 1950s. Up to now, x radiation from exotic atoms with muons (Fitch and Rainwater, 1953), pions (Camac *et al.*, 1952), kaons (Burlinson *et al.*, 1965), antiprotons (Bamberger *et al.*, 1970), and sigma hyperons (Backenstoss *et al.*, 1970) has been established.

In leading order, given by the Bohr formula, the level binding energies  $B_n$  are proportional to the reduced mass  $\mu$  of the captured particle and nucleus, and the Bohr radii  $r_B$  are proportional to  $1/\mu$ :

$$B_n = \mu c^2 \alpha^2 Z^2 / 2n^2, \quad (1)$$

$$r_B = \hbar c / \mu c^2 \alpha Z, \quad (2)$$

where  $\mu$  is defined as  $\mu = m_N m / (m_N + m)$ , with  $m_N$  the mass of the nucleus and  $m$  the mass of the exotic particle. The symbols  $\alpha$ ,  $Z$ , and  $n$  denote the fine structure constant, the atomic number, and the principal quantum number, respectively. The present value of the conversion constant  $\hbar c$  is 197.326 978 8(12) MeV with an uncertainty of 22 ppb (Patrignani *et al.*, 2017).

As an example, Table I (Gotta, 2004) gives the binding energies  $B_{1s}$  of the atomic ground states and the Bohr radii  $r_B$  of “electronic” and “exotic hydrogen” for a captured muon, pion, kaon, and antiproton.

### B. Formation of exotic atoms

When a negatively charged particle other than an electron enters a target it is slowed down to a kinetic energy of a few tens of eV by ionizations and excitations of the molecules of the target. An exotic atom is formed when this particle is

stopped inside the target and is captured by a target atom into an outer atomic orbit, replacing an electron. The capture is generally a very complex process, because of the large number of involved degrees of freedom. It depends on the atomic and molecular structure, on the range of values of the principal quantum number  $n$  and angular momentum  $l$ , and is specific to the element under consideration (von Egidy and Hartmann, 1982; Horvath and Entezami, 1983). It can be said that the capture occurs and the cascade starts when the overlap of the wave function of the exotic particle with the outermost electron orbit of an atom of the target is maximal. The initial principal quantum number  $n$  of the exotic atom is (Zmeskal, 2008)

$$n \sim \sqrt{\frac{\mu}{m_e}} n_e, \quad (3)$$

where  $\mu$  is the reduced mass of the system,  $m_e$  is the electron mass, and  $n_e$  is the principal quantum number of the outermost electron shell.  $n_e = 1$  for hydrogen and helium. For exotic hydrogen, the values of  $n$  for muons, pions, kaons, and antiprotons are 13, 15, 25, and 30, respectively.

For exotic hydrogen and, to some extent, for helium, the *Stark mixing* is quite important. Stark mixing occurs when the exotic atom passes through the Coulomb field of other target atoms. The electric field mixes the states with the same principal quantum number  $n$ , but different angular momenta  $l$ , following the selection rules  $\Delta l = \pm 1$  and  $\Delta m = 0$ . The level mixing between  $l$  and  $l - 1$  makes the *s*-wave component initiate the absorption reaction much faster than the cascade process. For kaonic atoms, this means that the kaon-nuclear absorption may occur from even higher orbits. Stark mixing is, therefore, responsible for the drastic reduction of the x-ray yield with increasing target density. The higher density turns out in a higher probability of interaction with neighboring atoms and their electric dipole fields. Figure 1 reports, for kaonic hydrogen, an example of cascade calculation showing the density dependence of the *K*-series x-ray yields. The yields quickly decrease at higher densities due to the Stark-mixing effect.

The kaon cascades down via *Coulomb deexcitation* and *external Auger emission* until, for lower lying states, the probability for *radiative transitions* becomes dominant (Markushin, 1994); see Fig. 2.

The involved time scales are as follows: for slowing down and capture into an atomic orbit,  $10^{-12}$  to  $10^{-9}$  s; for Coulomb deexcitation and Auger processes,  $10^{-12}$  to  $10^{-9}$  s; and for radiative transitions from lower lying states,  $10^{-17}$  to  $10^{-15}$  s.

TABLE I. Binding energies  $B_{1s}$  of the atomic ground state and “Bohr radii”  $r_B$  of “electronic” and “exotic” hydrogen for a captured particle of mass  $m$ .  $\mu$  is the reduced mass of the system and  $l_{\text{had}}$  denotes the angular momentum states noticeably affected by strong interactions (Gotta, 2004).

	$m$ (MeV/ $c^2$ )	$\mu$ (MeV/ $c^2$ )	$B_{1s}$ (keV)	$r_B$ (fm)	Accessible interaction	$l_{\text{had}}$
$ep$	0.511	0.511	$13.6 \times 10^{-3}$	53 000	Electroweak	...
$\mu p$	105.7	95.0	2.53	279	Electroweak	...
$\pi p$	139.6	121.5	3.24	216	Electroweak + strong	$s$
$Kp$	493.7	323.9	8.61	81	Electroweak + strong	$s, p$
$\bar{p}p$	938.3	469.1	12.5	58	Electroweak + strong	$s, p$

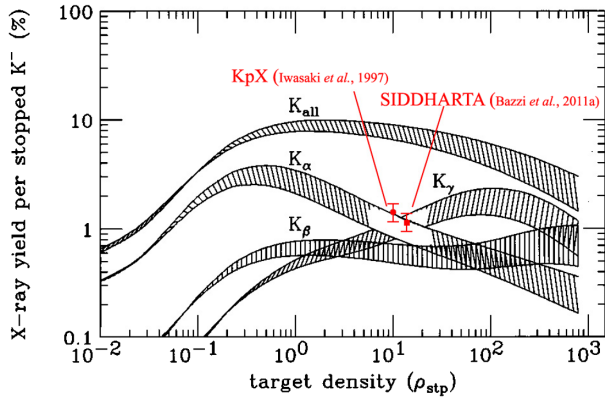


FIG. 1. Density dependence of  $K^-p$  atom x-ray yields. In this work the shift and width were taken to be  $\varepsilon_{1s} = 300$  eV,  $\Gamma_{1s} = 550$  eV, and  $\Gamma_{2p} = 1$  meV.  $\rho_{\text{STP}}$  denotes the density at the standard temperature and pressure. The liquid hydrogen density (LHD) corresponds to  $\sim 790 \rho_{\text{STP}}$ . The gas target density used in the KpX experiment, the first experiment to employ a cryogenic gaseous target, was  $\sim 10 \rho_{\text{STP}}$  (1.3% LHD). In the SIDDHARTA experiment (Bazzi *et al.*, 2011a) a gas target density of  $\sim 14.5 \rho_{\text{STP}}$  (1.8% LHD) was used. Adapted from Koike, Harada, and Akaishi, 1996.

The slowing down and the atomic process time scales are much faster than the lifetimes of the hadrons considered for exotic atoms as the kaon. Therefore, following the stopping of the kaon in matter, the kaon-nucleus strong interaction can be studied.

### C. Study of strong-interaction effects in kaonic atoms

The study of strong-interaction effects was the major motivation for performing experiments with kaonic atoms. The electromagnetic interaction with the nucleus is well known and the energy levels can be calculated at a precision of eV by solving the Klein-Gordon equation. Even a small deviation from the electromagnetic value allows one to get

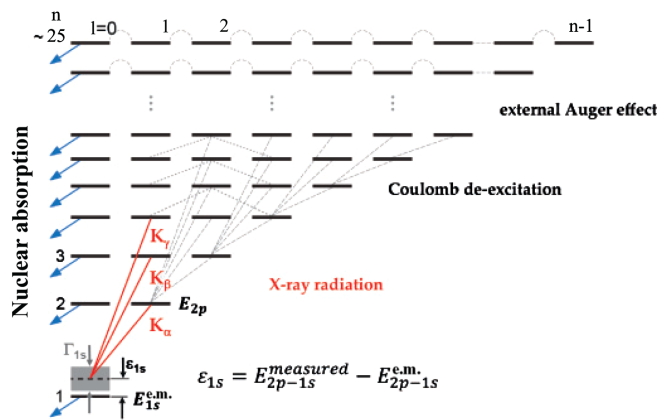


FIG. 2. Cascade processes for kaonic hydrogen, starting when the kaon is captured in a highly excited state, down to the  $1s$  ground state, which is shifted due to strong interaction and broadened due to nuclear absorption of the kaon by the proton. The shift and width of the  $2p$  state due to strong interaction are negligible.

information on the strong interaction between the kaon and the nucleus.

From Table I, one sees that the atomic binding energies of light systems are in the keV range, namely, the kaon interacts with the nucleus with a relative energy of a few keV, instead of the tens of MeV, as performed in the low-energy scattering experiments. Hence, kaonic atoms offer the unique opportunity to study the antikaon-nucleon-nucleus interaction, nearly “at threshold,” namely, at zero relative energy.

Of particular interest in kaonic atom experiments are the studies of systems formed with hydrogen isotopes, which give access to the basic low-energy physics parameters such as the *antikaon-nucleon scattering lengths*. Kaonic deuterium enables access to the antikaon-neutron system. Other light elements provide information on how to construct the antikaon-nucleus interaction from elementary reactions. It is noteworthy that light exotic atoms are formed almost “electron free,” which opens the possibility for high-precision measurements due to the absence of the electron screening effect.

In the study of strong-interaction effects, the observables of interest are the shift ( $\varepsilon$ ) and the width ( $\Gamma$ ) of the atomic levels caused by the strong interaction between the kaon and the nucleus. The levels are shifted and broadened relative to the electromagnetic value, but the shift and width are sensible only for the ground state  $1s$ .

For the sign of the strong-interaction shift  $\varepsilon_{1s}$  we use the Warsaw convention (Iwasaki *et al.*, 1997), according to which  $\varepsilon_{1s}$  is defined as

$$\varepsilon_{1s} = E_{2p \rightarrow 1s}^{\text{measured}} - E_{2p \rightarrow 1s}^{\text{e.m.}}, \quad (4)$$

where  $E_{2p \rightarrow 1s}^{\text{measured}}$  and  $E_{2p \rightarrow 1s}^{\text{e.m.}}$  are the  $2p \rightarrow 1s$  transition energies experimentally measured and calculated with only the electromagnetic interaction taken into account, respectively.

The electromagnetic  $2p \rightarrow 1s$  energy transition is calculated by solving the Klein-Gordon equation and then applying finite size and vacuum polarization corrections. The value obtained for kaonic hydrogen is  $6480 \pm 1$  eV (Iwasaki *et al.*, 1997).

Neglecting isospin-breaking corrections altogether, i.e., assuming  $m_d = m_u$ , in the case of kaonic hydrogen the relation between  $\varepsilon_{1s}$  and  $\Gamma_{1s}$  and the  $K^-p$  complex scattering length  $a_{K^-p}$  is given by the so-called Deser-Trueman formula (Deser *et al.*, 1954; Trueman, 1961)

$$\varepsilon_{1s} + \frac{i}{2} \Gamma_{1s} = 2\alpha^3 \mu^2 a_{K^-p}. \quad (5)$$

It turns out, however, that the isospin-breaking corrections to the lowest order of Eq. (5) are large (Meißner, Raha, and Rusetsky, 2004, 2006). They are much larger than their counterparts in pionic hydrogen ( $\pi^-p$ ) or in pionium ( $\pi^+\pi^-$ ), where they are typically at the few percent level.

The large isospin-breaking corrections arise, in particular, from  $s$ -channel rescattering with  $\bar{K}^0 n$  intermediate state (the *cusp effect*) and Coulomb corrections that are nonanalytic in  $a_{K^-p}$ , but proportional to  $\ln(a_{K^-p})$ .

Meißner, Raha, and Rusetsky (2004, 2006) evaluated the isospin-breaking effects in terms of  $\alpha$  and  $\delta \sim m_d - m_u$ . The Deser-Trueman formula was modified up to and including all terms of order  $O(\delta^4)$  [we use the Landau symbol  $O(x)$  for quantities that vanish like  $x$  when  $x$  tends to zero].

By the inclusion of the isospin-breaking corrections, the improved Deser-type formula at the next-to-leading order in isospin breaking becomes

$$\varepsilon_{1s} + \frac{i}{2}\Gamma_{1s} = 2\alpha^3\mu^2 a_{K^-p} [1 - 2\alpha\mu(\ln\alpha - 1)a_{K^-p} + \dots]. \quad (6)$$

A similar formula holds for the  $K^-d$  scattering length  $a_{K^-d}$ :

$$\varepsilon_{1s} + \frac{i}{2}\Gamma_{1s} = 2\alpha^3\mu^2 a_{K^-d} [1 - 2\alpha\mu(\ln\alpha - 1)a_{K^-d} + \dots]. \quad (7)$$

The  $K^-p$   $s$ -wave scattering length  $a_{K^-p}$  is related to the  $\bar{K}N$  isospin-dependent ( $I = 0, 1$ ) scattering lengths  $a_0$  and  $a_1$  through the average

$$a_{K^-p} = \frac{1}{2}[a_0 + a_1]. \quad (8)$$

In order to obtain the individual isoscalar  $a_0$  and isovector  $a_1$  scattering lengths one has to also measure the kaonic deuterium, which provides information on a different combination of  $a_0$  and  $a_1$ :

$$a_{K^-n} = a_1, \quad (9)$$

$$a_{K^-d} = \frac{4[m_N + m_K]}{2m_N + m_K} Q + C, \quad (10)$$

where

$$Q = \frac{1}{2}[a_{K^-p} + a_{K^-n}] = \frac{1}{4}[a_0 + 3a_1]. \quad (11)$$

The first term in Eq. (10) represents the lowest-order impulse approximation [ $K^-$  scattering from each (free) nucleon of deuterium]. The second term  $C$  includes all higher-order contributions, namely, all other physics associated with the  $K^-d$  three-body interaction.

The three-body system  $\bar{K}NN$  can be studied by solving Faddeev-type equations, taking into account the dynamics of the system, namely, specifying the two-body interactions. Among all the spin-isospin states of the  $\bar{K}NN$  system, the  $K^-d$  state has an advantage, since the  $K^-d$  scattering and the properties of kaonic deuterium can be directly measured.

On the other side, the  $K^-d$  three-body problem includes the complication that the  $K^-p$  and  $K^-n$  interactions involve significant inelastic channels, such as

$$K^-p \rightarrow \bar{K}^0n - 5 \text{ MeV}, \quad (12)$$

$$K^-p \rightarrow \pi\Sigma + 100 \text{ MeV}, \quad (13)$$

$$K^-p \rightarrow \pi^0\Lambda + 180 \text{ MeV}, \quad (14)$$

which require a coupled-channel formalism, including both elastic and inelastic channels.

### III. ANTIKAON SOURCES, TARGETS, AND DETECTOR DEVELOPMENTS

#### A. Antikaon sources

##### 1. DAΦNE at Laboratori Nazionali di Frascati of INFN

DAΦNE is a world-class electron-positron collider at the LNF-INFN in Italy. The engineering and design phase of the accelerator complex started in January 1991 and it has been housed in the same buildings that previously hosted ADONE [the big ADA (Anello Di Accumulazione), the first  $e^+e^-$  collider in the world, invented in Frascati National Laboratories of INFN by B. Toushek]. It is worth mentioning that ADONE was successfully operated until April 1993, and the first electron beam was already stored in DAΦNE by October 1997.

The DAΦNE accelerator complex includes a double ring lepton collider working at the c.m. energy of the  $\phi$  resonance (1.02 GeV) and an injection system; see Fig. 3. In its original configuration (Vignola *et al.*, 1996) the collider consisted of two independent rings, each  $\sim 97$  m long, sharing two 10 m long interaction regions (IR1 and IR2), where the KLOE and FINUDA or DEAR detectors were, respectively, installed, taking data one at a time. A full energy injection system, including an S-band linac, 180 m long transfer lines, and an accumulator or damping ring, provides fast and high efficiency  $e^+/e^-$  injection also in the topping-up mode during collisions.

DAΦNE has been delivering luminosity to the experiments since 2001 implementing, at the same time, several progressive upgrades intended to push the collider performances in terms of luminosity. In fact, at the end of the KLOE run in 2005, the maximum measured instantaneous luminosity was of the order of  $1.5 \times 10^{32} \text{ cm}^{-2} \text{ s}^{-1}$ , with a maximum daily integrated luminosity of  $\sim 9.6 \text{ pb}^{-1}$  (Gallo *et al.*, 2006). Comparable values have been measured during the operation for the FINUDA experiment in 2007 (Milardi *et al.*, 2007).

However, the experimental activity at DAΦNE outlined several factors limiting any further relevant luminosity improvement. For this reason, in 2008 the collider underwent a major upgrade in order to implement a new collision scheme based on a large Piwinski angle and compensation of the resonances due to the beam-beam interaction: the crab-waist collision scheme (Raimondi, Shatilov, and Zobov, 2007).

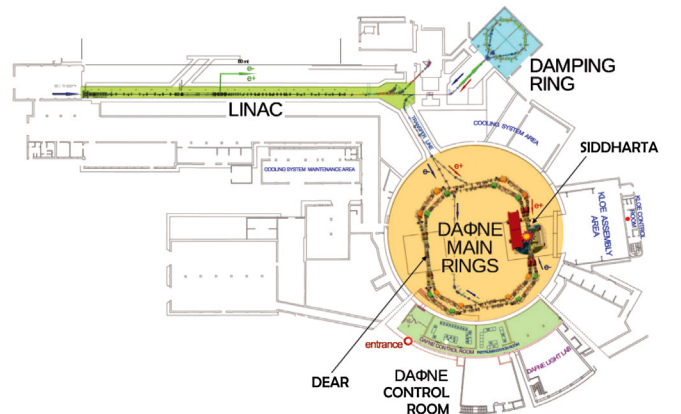


FIG. 3. DAΦNE accelerator complex layout. Adapted from Vignola *et al.*, 1996.

The new approach to collisions provides several advantages: it reduces the beam-beam tune shift in the horizontal plane, shrinks the longitudinal size of the overlap between colliding bunches, thus allowing one to increase the vertical focusing at the interaction point and, moreover, it cancels almost completely the parasitic crossings.

A pair of crab-waist sextupoles, installed in symmetric position with a proper phase advance with respect to the interaction point, suppresses the betatron and synchrotron resonances coming from the vertical motion modulation due to the horizontal oscillation. The upgrade offered an ideal opportunity to replace the IR2 with a crossing section providing complete separation between the two beams.

A comparison of the DAΦNE parameters in the nominal and the crab-waist configuration is presented in Table II.

The experience with the novel scheme, done while providing data to the SIDDHARTA experiment (Milardi *et al.*, 2009; Zobov *et al.*, 2010), outlined a factor of 3 increase in terms of peak luminosity with respect to previous collider performance.

This research and development activity in the accelerator physics field had wide international resonance: there are currently projects and machines under construction which include the crab-waist scheme as the main design element.

DAΦNE continues to be a worldwide unique low-energy kaon source via the decay of  $\phi$  mesons produced almost at rest to charged  $K^+/K^-$  pairs, with a probability of 48.9%; to neutral  $K_{0L}/K_{0S}$  pairs, with a probability of 34.2%; and to a  $\rho$  meson with one or three pions, with a probability of 15.3%. The produced charged kaons have a momentum of 127 MeV/c, and a momentum spread  $\Delta p/p < 0.1\%$ , making them ideal for use in producing and studying kaonic atoms.

## 2. Japan Proton Accelerator Research Complex

J-PARC is a joint project between two organizations, the High Energy Accelerator Research Organization (KEK) and the Japan Atomic Energy Agency (JAEA). The facility is located in the Tokai village, in the northern region of Ibaraki prefecture, Japan. The construction started in April 2001 and in spring 2009 phase 1 of the project was completed. J-PARC consists of a series of world-class proton accelerators and

TABLE II. DAΦNE beams parameters.

	DAΦNE (Nominal)	DAΦNE upgrade crab-waist
$\beta_y^*$ (cm)	1.7	0.9
$\beta_x^*$ (cm)	170	25
$\sigma_x^*$ (cm)	760	200
$\sigma_y^*$ (cm)	5.4	3.5
$\sigma_z^*$ (cm)	2.5	1.7
$\theta_{\text{cross}}/2$ (mrad)	12.5	25
$\psi$ (mrad)	0.6	1.9
$\epsilon$ (mm mrad)	0.34	0.26
Average bunch current (mA)	10–15	10–15
Synchrotron radiation loss per turn (keV)	9.7	9.7
rf (radio frequency) $f$ (MkHz)	368.265	368.667
Harmonic number	120	120
$L \times 10^{32}$ (cm <sup>-2</sup> s <sup>-1</sup> )	1.5	4.5

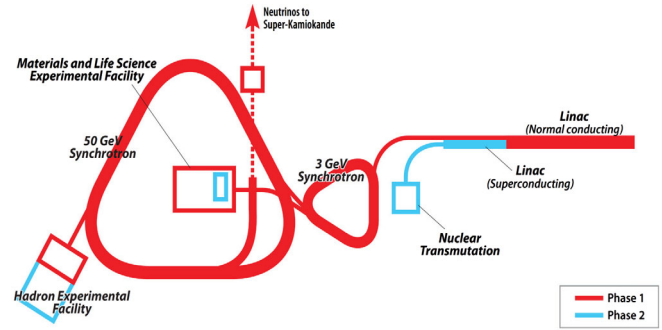


FIG. 4. J-PARC accelerator layout, showing the existing facilities in red and the proposed upgrades in blue. Adapted from Sako, 2010.

experimental facilities making use of high-intensity proton beams. J-PARC is a multipurpose and multidisciplinary facility that is unique in a variety of secondary beams. Neutron, pion (muon), kaon, and neutrino beams are produced via collisions between the proton beams and target materials (spallation reactions). Applications of these beams include fundamental nuclear and particle physics, material and life science, and nuclear technology.

At J-PARC, a proton beam is accelerated to high intensity and high energy by a series of accelerators (Fig. 4), which consist of a 400 MeV linear accelerator (LINAC), which has a length of 330 m with a current for user operation of 40 mA; a 3 GeV rapid cycling synchrotron (RCS), which has a circumference of about 350 m and provides a proton beam current of 333  $\mu\text{A}$  (1 MW); and a 50 GeV (currently 30 GeV) main ring (MR), which has a circumference of about 1600 m and provides a proton beam current of 15  $\mu\text{A}$  (0.75 MW).

### a. Beam production scheme

A negative hydrogen ( $\text{H}^-$ ) is produced at the ion source and accelerated in the linac to 400 MeV. The  $\text{H}^-$  beam is injected into a carbon stripping foil, where the two electrons of the  $\text{H}^-$  are stripped and the remaining proton is further accelerated to 3 GeV in the rapid cycling synchrotron. Part of the beam is injected to the MR, while the rest of it is transported to the Material and Life Science Facility (MLF). In the MLF the protons are converted to pulsed spallation neutrons and muons. In the MR the protons are further accelerated to 30 GeV (and in the future to 50 GeV) and then either via fast extraction, transported to the Neutrino Experimental Facility to produce a pulsed neutrino beam or via slow extraction to the Hadron Hall to produce an intense kaon beam with a momentum of about 1 GeV/c. The accelerator complex is operated in a pulse mode. The linac and RCS are operated at a 25 Hz cycle, while the main ring works at 0.27 Hz.

### b. Kaon production scheme: The K1.8 beam lines

The secondary main kaon beam lines K1.8 and K1.8BR were constructed at the Hadron Hall using primary protons from the J-PARC 50 GeV synchrotron (MR). Up to now only 30 GeV primary protons are produced, which are transported to the Hadron Hall through the beam switching yard and

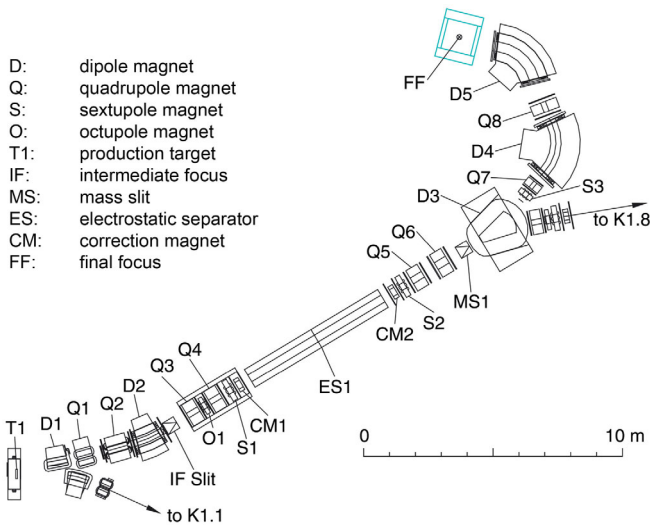


FIG. 5. Configuration of the K1.8BR beam line in the Hadron Hall of J-PARC. Adapted from Agari *et al.*, 2012.

focused on the secondary-particle-production, water-cooled gold target  $T1$  (Takahashi *et al.*, 2015).

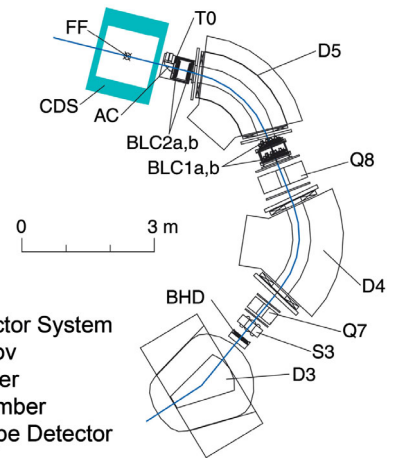
In the following, the K1.8BR beam line is described in more detail, because the kaonic helium E62 experiment that has concluded the data taking in June 2018, and the future kaonic deuterium E57 experiment, was installed and will be installed there. K1.8BR branches off from K1.8 at a bending magnet downstream of an electrostatic separator (ES1), used to purify secondary beams of charged particles with momenta up to 1.2 GeV/ $c$ .

The layout of the K1.8BR is shown in Fig. 5 and the main parameters are summarized in Table III. The length of the K1.8 BR beam line was optimized to have only 31.3 m from the production target  $T1$  to the final focus, where the experimental apparatus will be placed. Details of the beam line, such as the beam line elements and optical design, have been described by Agari *et al.* (2012).

A schematic view of the beam line spectrometer is shown in Fig. 6. It is composed of beam line magnets, trigger counters, beam trackers, and a kaon identification counter. The beam trigger is generated at the coincidence signal of a beam hodoscope detector (BHD) and a time zero counter (T0). The flight length between the BHD and T0 is 7.7 m. The kaon beam with momentum around 0.9–1.2 GeV/ $c$  is identified by using an aerogel Cherenkov counter (AC) with a refractive index of 1.05. The kaon beam is tracked with two beam trackers: beam line chamber 1 (BLC1) and beam line

TABLE III. Parameters of the K1.8BR beam line.

Primary beam	30 GeV/ $c$ proton
Repetition cycle	5.2 s
Flat top	2.93 s
Production target	Au
Production angle	6 deg
Length (T1–FF)	31.2 m
Momentum range	1.2 GeV/ $c$ (max.)
Acceptance	2.0 msr% ( $\Delta\Omega \Delta p/p$ )
Momentum bite	$\pm 3\%$



FF Final Focus  
CDS Cylindrical Detector System  
AC Aerogel Cherenkov  
T0 Time zero counter  
BLC Beam Line Chamber  
BHD Beam Hodoscope Detector

FIG. 6. Schematic view of the beam line spectrometer. The setup consists of a beam line spectrometer, a cylindrical spectrometer system (CDS), trigger counters (BHD and T0), beam line chambers (BLC1 and BLC2), and a kaon identification counter (AC). The beam line magnets, composed of an SQDQD system, consist of beam sweeping dipole magnets (D4 and D5), quadrupole magnets (Q7 and Q8), and a sextupole magnet (S3). Adapted from Agari *et al.*, 2012.

chamber 2 (BLC2). Pions in the beams are discriminated from kaons using the kaon identification counter, and protons are removed by ES1 (Fig. 5). The trajectory of the kaon beam is tracked with the two beam line chambers installed across the D5 magnet. The kaon momentum is analyzed using this tracking information together with beam optics of the D5 beam line magnet to attain an expected momentum resolution of  $\sim 0.1\%$ . The beam line spectrometer was completed in January 2009, when the first beam was delivered to the J-PARC Hadron Hall.

The operation for the Hadron Hall experiments with the slow extracted proton beam was steadily optimized achieving the following parameters at the end of 2017: the acceleration time in the MR was shortened from 1.9 to 1.4 s with a duration of slow extracted primary protons of about 2.5 s. The full cycle now has a duration of 5.2 s (before 6.0 s), delivering  $5.5 \times 10^{13}$  primary protons during one extraction cycle to the Hadron Hall at a MR beam power of 50 kW. This translates into a charged kaon production of  $5 \times 10^3$  kaons/spill/kW (primary proton beam power) at a momentum of 1 GeV/ $c$  with a  $K^-/\pi^-$  ratio of 45:100, which reduces to  $5 \times 10^2$  kaons/spill/kW for a kaon momentum of 0.7 GeV ( $K^-/\pi^-$  ratio of 5:100), which can be used for kaonic atoms studies.

## B. Target systems for light kaonic atoms

There are general requirements for research on kaonic-hydrogen isotopes, like high-purity gas target systems, to avoid kaon losses due to the Stark effect, cooled to cryogenic temperature. On the other hand, these targets have to be designed for optimum x-ray detection by reducing the material budget in front of the x-ray detector.

According to the different kaon sources, the shapes of the target systems are quite different, but in common for all cells is

TABLE IV. Main parameters of different lightweight target cells.

	SIDDHARTA	SIDDHARTA-2	E57
Active target volume (cm <sup>3</sup> )	2400	2100	540
Target diameter (cm)	13.7	14.5	6.0
Working temperature (K)	20–25	25–30	25–30
Working pressure (MPa)	0.10	0.25	0.5
Gas density	1.8% <sup>a</sup>	3% <sup>b</sup>	4% <sup>b</sup>
Burst pressure (MPa)	0.40	0.65	0.80
Kapton entrance window (μm)	125	125	125
Kapton side wall (μm)	75	140	140

<sup>a</sup>Gas density as a fraction of the liquid hydrogen density (0.0708 g/cm<sup>3</sup>).

<sup>b</sup>Gas density as a fraction of the liquid deuterium density (0.164 g/cm<sup>3</sup>).

the request for thin target walls, facing the x-ray detector. Table IV summarizes the main characteristics of lightweight target cells used for SIDDHARTA and for the future planned SIDDHARTA-2 and E57 experiments.

### C. Advances in exotic atom x-ray detection: From charge-coupled devices to silicon drift detectors

The first kaonic-hydrogen x-ray measurement, initialing the modern era of kaonic atoms research, made use of Si(Li) detectors in the KpX experiment (at KEK, Japan). CCDs were successfully used as x-ray detectors for the DEAR experiment at LNF-INFN. Finally, SDDs were adapted for kaonic atom research, in the framework of the European project HadronPhysics within the EU-FP6 Programme, when for the first time large area SDDs were developed with  $3 \times 1$  cm<sup>2</sup> cells on one silicon wafer, for the SIDDHARTA programme at DAΦNE. Research and development work on SDDs continued, leading to an optimized detector for the future kaonic deuterium programs at LNF-INFN and J-PARC. A comparison of the main characteristics of these detector systems is given in Table V.

#### 1. Charge-coupled devices

CCD arrays are ideal detectors for a variety of x-ray imaging and spectroscopy applications. Performance characteristics, such as a high dynamic range, versatile readout, and data-storage modes, made them suitable for exotic atom research (Fiorucci *et al.*, 1990; Varidel *et al.*, 1990; Egger, Chatellard, and Jeannet, 1993). In its simplest version, the CCD structure consists of a series of closely spaced electrodes separated from an underlying semiconductor substrate by a thin insulating oxide layer; see Fig. 7. When a bias voltage is

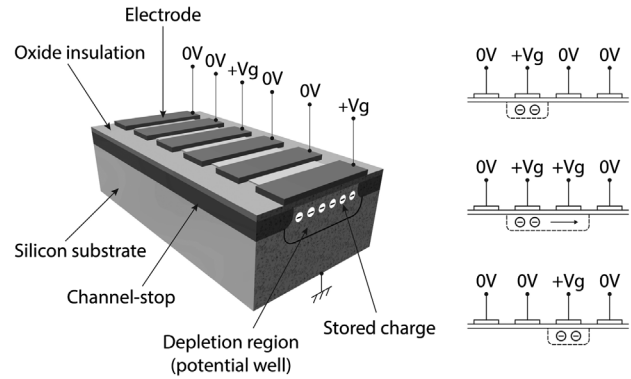


FIG. 7. (Left) The structure of a CCD. (Right) A sketch showing how the charge below a pixel is transferred.

applied to an electrode, a depletion region is formed beneath it in the semiconductor. This depletion region is like a potential well which can store an electrical charge packet. By pulsing the electrodes in an appropriate sequence, the potential well, and hence its charge packet, can be transferred through the semiconductor (see Fig. 8) to be finally read out and processed. By applying a shift register, the original position of the charge packet can be determined.

Identification of x-ray events and determination of their energies are achieved by taking advantage of the pixelized structure, which allows one to apply a selection based on topological and statistical criteria (Ishiwatari *et al.*, 2006). This powerful background rejection tool is based on the fact that x rays in the 1–10 keV energy range interact mainly via the photoelectric effect and have a high probability to deposit all their energy in a single or at most two adjacent pixels, whereas the energy deposited from background particles, charged particles, gammas, or neutrons, is distributed over several pixels (therefore called “cluster events”), which can be rejected; see Fig. 8, left. A selected “single pixel” (see Fig. 8, right), a pixel with a charge content above the noise threshold, which is surrounded by eight neighbor pixels having a charge content below that threshold, is considered to be an x-ray hit. Also two-adjacent pixels good events are considered to be a good x-ray hit. For the DEAR experiment, CCD55-30 detector chips (from Marconi Applied Technologies) were used, each with a total effective area of 7.24 cm<sup>2</sup>, consisting of  $1242 \times 1152$  pixels with a pixel size of  $22.5 \times 22.5$  μm<sup>2</sup>. A depletion depth of about 30 μm was achieved with an x-ray detection efficiency of about 60% at 6 keV. The working temperature of the CCD chips was set at 165 K to achieve an energy resolution of 150 eV at 6 keV, which is almost 3 times

TABLE V. Comparison of x-ray detectors for kaonic atom research.

Detector	Si(Li)	CCD	SDD-KETEK	SDD-JFET	SDD-CUBE
Effective area (mm <sup>2</sup> )	200	724	$1 \times 100$	$3 \times 100$	$8 \times 64$
Thickness (mm)	5	0.03	0.26	0.45	0.45
Energy resolution (eV) at 6 keV	410	150	190	160	140
Drift time (ns)	290	...	375	800	300
Experiment	KpX	DEAR	E570	SIDDHARTA	E57, SIDDHARTA-2
Reference	Iwasaki <i>et al.</i> (1997)	Ishiwatari <i>et al.</i> (2006)	Okada <i>et al.</i> (2007)	Bazzi <i>et al.</i> (2011a)	Quaglia <i>et al.</i> (2015)

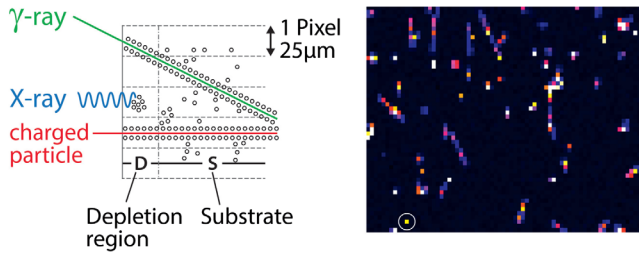


FIG. 8. (Left) Particle interactions and charge collection in a CCD detector. (Right) An example of an x-ray signal (inside the circle) in a CCD picture exposed during a data-taking run.

better than that of the Si(Li) detectors (410 eV, see Table V). The study of transport and charge integration for the DEAR experiment showed that the best results in terms of resolution and linearity were obtained with a readout time of about 90 s. Investigations on how occupancy affects efficiency, resolution, and linearity have shown that a total exposure of 120 s is acceptable (corresponds to an occupancy of  $\sim 10\%$ ). During the readout the CCDs were exposed; therefore the whole acquisition could be done in continuous readout. In summary, the CCD55-30 chip used for DEAR is characterized by an excellent energy resolution of 150 eV at 6 keV at a temperature of 165 K, with an applied readout time of 90 s (the exposure time depends on the radiation environment). CCDs cannot be used for timing applications.

## 2. Silicon drift detectors

SDDs, initially developed as position sensitive detectors, are used nowadays also for x-ray spectroscopy (Gatti and Rehak, 1984, 2005; Lechner *et al.*, 1996). The characteristic parameters of SDDs are reported in Table V.

On one side of the SDD a concentric ring-shaped strip segmentation is placed, as well as a small collecting anode located in the center of the strips. The other side is made of a nonstructured junction, which forms the radiation entrance window and gives a homogeneous sensitivity over the whole detector area.

The  $n$ -type device substrate is fully depleted by applying a negative voltage (with respect to the collecting anode) to the  $p^+$  back contact and the  $p^+$  field strip rings on the opposite side. The negative bias of the  $p^+$  rings progressively increases from the ring next to the anode to the far outmost one. The maximum negative voltage of the outmost ring is about twice the voltage of the back contact. The minimum potential energy for electrons falls diagonally from the backside edge of the device to the readout electrode in the center of the upper side. Each electron generated inside the depleted detector volume by absorption of ionizing radiation will therefore drift to the  $n^+$  readout anode. The generated holes are collected by the reverse biased  $p^+$  implanted regions which form the radiation entrance window. The main feature of the SDDs is the small value of the anode capacitance, which provides a lower rise time and increases the amplitude of the output signal, hence permitting one to achieve good resolution in energy and time, as well as less noise in subsequent electronic components even during high count rate measurements. This capacitance is practically independent of the active area and thus allowed one

to develop detectors with large area and reduced thickness. The reduced thickness in the depletion layer ( $\sim 500 \mu\text{m}$ ) results in less sensitivity to background events caused by high-energy gamma rays or electrons, but still achieving almost 100% efficiency for 8 keV x rays (97.5% at 10 keV).

## 3. SDDs with implanted junction gate field-effect transistor (JFET)

For the SIDDHARTA experiment, to take full advantage of the low output capacitance, an  $n$ -channel JFET was integrated on the detector chip close to the  $n^+$  implanted anode; see Fig. 9. The JFET and the anode are located on the upper side of the device, in the center of the  $p^+$  field rings. In that way, stray capacitances of various connections are minimized and a perfect matching between detector and front-end electronics capacitance is achieved.

The on-chip electronics includes a sensing anode, a first amplifying JFET, and a reset mechanism. The electron collecting anode is an  $n^+$  contact surrounding the JFET in a close geometry. The largest part of the capacitance of the detector arises from the relatively large geometry of the collecting anode structure. The integrated transistor is a nonconventional single sided  $n$ -channel JFET, which is operated on completely depleted high resistivity silicon. For the reset of the anode potential, caused by signal charges and leakage current, a pulsed reset method has been used. The pulsed reset is done by applying positive voltage pulses to the  $n^+$  implanted clear contact; see Fig. 9. During the clear pulse, a path for electrons is opened from the anode to the clear contact. This is the classical pulsed, nonoptical reset in source follower configurations.

The SDD chips for SIDDHARTA were developed in the framework of the European project HadronPhysics3 within the EU-FP7 (Bazzi *et al.*, 2011b). The SDDs operated at a temperature of  $\sim 170$  K achieve an energy resolution of 160 eV (FWHM) at 6 keV and a drift time (timing resolution) below  $1 \mu\text{s}$ . The cooling and mounting structure of the SDD chips, as well as the first amplification stage and the high- and low-voltage supply boards, lead to an active to total x-ray detection area of about 25%. Overall, 48 SDDs, each with  $3 \times 1 \text{ cm}^2$  cells and a thickness of  $450 \mu\text{m}$ , were used; see Fig. 10.

Although the detector performed very well in the high radiation environment of DAΦNE, there was a drawback: During injection of electrons and positrons into the DAΦNE

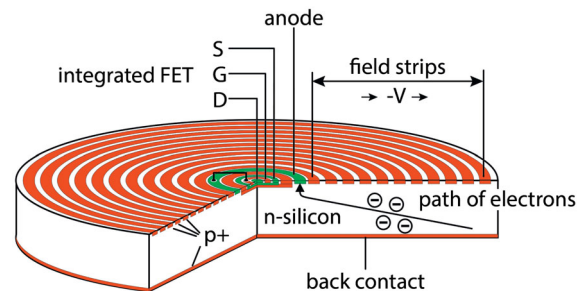


FIG. 9. SDD structure with implanted JFET (S = source, G = gate, D = drain) and reset mechanism via a clear contact. Adapted from Lechner *et al.*, 1996.

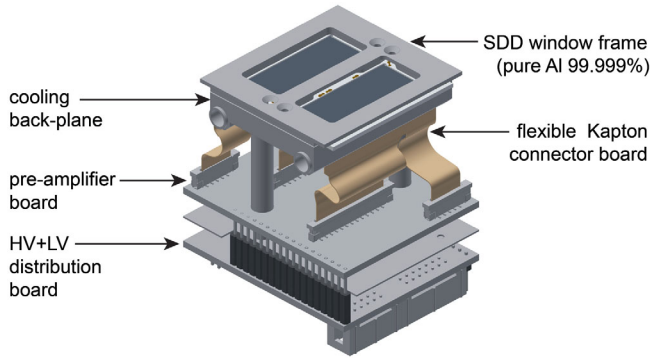


FIG. 10. Subdetector unit with two SDD chips, each with three individual cells, used in the SIDDHARTA experiment.

storage rings the beam related background raised almost 2 orders of magnitude, compared to the “normal” collision mode, causing around one-third of the SDDs to latch up. These SDDs had to be recovered by lowering the supply voltages and slowly ramping them up again, leading to an additional dead time of a few seconds, before stable operation was regained.

#### 4. New monolithic SDD arrays

New monolithic SDD arrays have been developed by Fondazione Bruno Kessler, Italy, together with Politecnico di Milano, LNF-INFN and SMI, Austria for the study of kaonic deuterium x rays at LNF-INFN (SIDDHARTA-2 experiment) and J-PARC (E57 experiment). Each monolithic array is  $450\ \mu\text{m}$  thick and consists of eight square SDD cells, each with an active area of  $8 \times 8\ \text{mm}^2$ . The individual SDD cells are arranged in a  $2 \times 4$  array with a 1 mm dead region along its border and are mounted on an alumina ceramic carrier; see Fig. 11, left. These SDD arrays belong to an improved technology with an average leakage current of  $200\ \text{pA/cm}^2$  at room temperature (Bertuccio *et al.*, 2015).

A big difference with respect to the previously used SDDs is the change of the preamplifier system from the JFET structure on the SDD chip to a complementary metal-oxide semiconductor integrated charge sensing amplifier (CUBE) (Bombelli *et al.*, 2011). For each SDD cell this CUBE amplifier is placed on the ceramic carrier as close as possible to the anode of the SDD. The anode is electrically connected to the CUBE with a bonding wire; see Fig. 11, center. This makes the SDDs performance almost independent on the applied bias voltages and increases their stability, even when

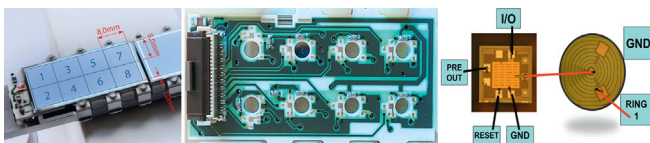


FIG. 11. Layout of the new  $2 \times 4$  SDD array: (left) SDD chip mounted on a ceramic carrier and aluminum cooling block, with indication of the pixel structure; (center) backside of the ceramic carrier with eight holes to allow for bonding connections of each anode to the CUBE amplifier; (right) amplified bonding layout for one anode CUBE arrangement.

exposed to high charged particle rates (test measurement at J-PARC K1.8BR).

The ceramic carrier is mounted on top of an aluminum holder block using M1 screws, not only to protect the delicate detector bonding connections but also to cool down the SDDs to cryogenic temperatures (100–150 K). The special structure of the ceramic carrier (gear-wheel type) allows a close packing of the SDDs around the target cell, which is essential for optimizing the geometrical x-ray detection efficiency. Furthermore, a better drift time of 300 ns can be achieved with the newly developed SDDs compared to the previous ones ( $\sim 800\ \text{ns}$ ) by changing the active cell area from 100 to  $64\ \text{mm}^2$  and by further cooling to 100 K, which was not possible before, because of the delicate JFET structure, which reached an optimal performance at around 170 K.

In summary, the main parameters of the new monolithic SDDs with external CUBE preamplifier developed for kaonic deuterium measurements are an excellent energy resolution of 140 eV at 6 keV at a temperature of 100 K with a time resolution (drift time)  $\sim 300\ \text{ns}$ , optimized active to total x-ray detection area of 75%, and no problems with latch-up at high counting rates.

## IV. THE EXPERIMENTAL RESULTS IN THE MODERN ERA

### A. The beginning of the modern era: The “kaonic-hydrogen puzzle” and its solution

#### 1. The kaonic-hydrogen puzzle

Three measurements of kaonic-hydrogen x rays were carried out at CERN and the Rutherford Laboratory, in the late 1970s through the early 1980s (Davies *et al.*, 1979; Izzycki *et al.*, 1980; Bird *et al.*, 1983).

In these measurements, liquid hydrogen targets and Si(Li) detectors were used. Davies *et al.* (1979) observed a peak at  $6.52 \pm 0.06\ \text{keV}$ , which they attributed to the  $K_\alpha$  line. Izzycki *et al.* (1980) observed a weak pattern of three lines at  $6.96 \pm 0.09$ ,  $7.99 \pm 0.07$ , and  $8.64 \pm 0.10\ \text{keV}$ , which they assigned to the  $K_\alpha$ ,  $K_\beta$ , and  $K_\gamma$  transitions, respectively. Bird *et al.* (1983) identified a similar series of transitions.

As shown in Fig. 12, all three spectra suffered from large background and low statistics: X-ray signals were very difficult to identify, having been strongly attenuated by the Stark effect in the liquid hydrogen target.

A common feature, despite the low quality of the data, was that the sign of the shift, and, consequently, that of the real part of the  $K^-p$  scattering length, was *positive*, which implied an *attractive-type* strong interaction. This was in striking contradiction with the results of the analyses of the low-energy data [ $K^-p$  cross sections for elastic and inelastic processes, branching ratios for  $K^-p$  absorption at rest,  $\pi\Sigma$  invariant mass distributions; see, for example, Martin (1981), using the  $K$ -matrix approach; and Kim (1965) and Sakitt *et al.* (1965) using the constant scattering length approach], which found a *negative real part* of the scattering length, corresponding to a *repulsive-type* strong interaction, turning out in a less bound ( $K^-p$ ) system. This discrepancy between x-ray measurements and low-energy scattering data has been named the *kaonic-hydrogen puzzle*. This “puzzle” has received considerable theoretical attention, with about 15 years of effort trying to

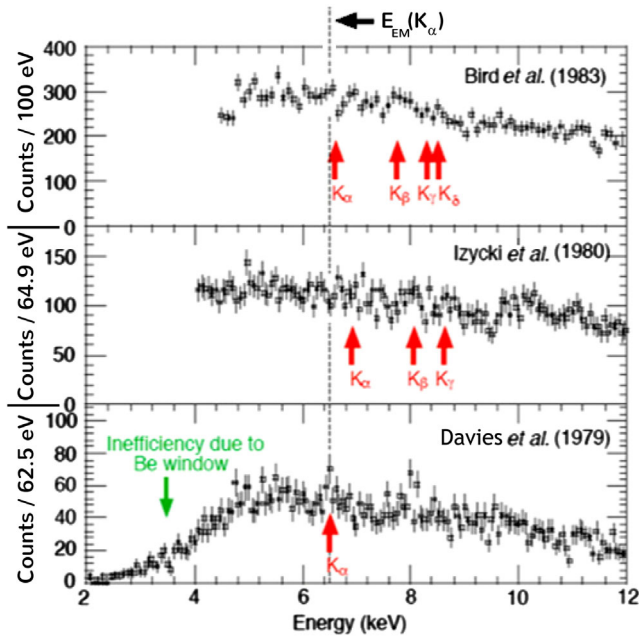


FIG. 12. The three kaonic-hydrogen x-ray transition measurements carried out at CERN and the Rutherford Laboratory, in the late 1970s through the early 1980s. In these measurements a liquid hydrogen target was used.

reconcile the two sets of data. However, no satisfactory theoretical explanation was found: various attempts to find a phenomenological potential fitting both the low-energy data and the kaonic-hydrogen measurements were unsuccessful.

## 2. The KpX kaonic-hydrogen measurement at KEK

In 1993, a proposal for a kaonic-hydrogen x-ray measurement was submitted to the KEK 12 GeV-PS PAC.

The experiment (E228, KpX) was performed at the K3 low-energy separated beam line at the KEK Proton Synchrotron. A cross-sectioned view of the experimental apparatus is shown in Fig. 13.

Two experimental difficulties had to be dealt with by the KpX experiment. One was the small yield of the  $K$  transitions; the other was the hadronic background. All the previous experiments employed a liquid hydrogen target in order to stop  $K^-$ 's efficiently. The cascade calculations, however, show (Fig. 1) that the  $K_\alpha$  yield at the liquid hydrogen density  $790\rho_{\text{STP}}$  is up to 1 order of magnitude lower than the yield at gaseous densities.

KpX was the first experiment which employed a gaseous target at 4 atm and 100 K ( $10\rho_{\text{STP}}$ , 1.3% LHD), so to substantially reduce the Stark effect.

The background reduction was the other key issue to be solved. Many background sources were present, due not only to beam-contaminating pions, but also to products of kaon-absorption reactions, and to in-flight reactions and decays. Contaminating pions and pile-up effects had to be removed off-line using lucite Čerenkov counters (see Fig. 13), since the mass separation of the KEK K3 beam line was limited to  $\pi^-:K^- \sim 90:1$ .

The  $K^-p$  absorption, which occurs as the final stage of the atomic cascade of the kaonic-hydrogen atom, produces

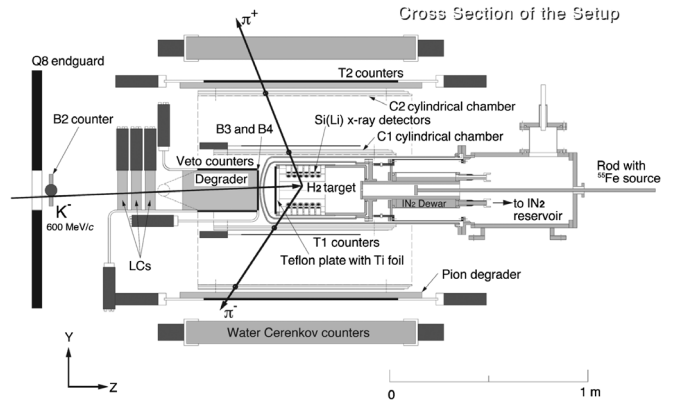


FIG. 13. The major components of the KpX experimental apparatus. A beam of negatively charged kaons of 600 MeV/c was utilized from the KEK 12 GeV-PS at the K3 beam line, the momenta degraded by a carbon block, after which they were injected into the hydrogen target. Kaons were identified by three lucite Čerenkov (LCs) counters sandwiched with the beam defining counters  $B2$  and  $B3$ . Two charged pions emitted from the  $K^-p$  reaction were tracked by two cylindrical MWPCs  $C1$  and  $C2$  and triggered by the cylindrical hodoscope counters  $T1$  and  $T2$ . The contaminating  $e^\pm$  tracks were rejected by outermost water Čerenkov counters. To achieve a maximum solid angle for x rays, 60 Si(Li) crystals were directly exposed to the gaseous hydrogen target, whose density was  $\rho \sim 10\rho_{\text{STP}}$ . From Ito *et al.*, 1998.

various reaction products including high-energy  $\gamma$  rays. These high-energy  $\gamma$  rays, which are mainly generated by the decays of  $\pi^0$ ,  $\Lambda$ , and  $\Sigma^0$ , were a major background source in the previous experiments. There are, however, reaction modes that have no  $\gamma$  rays in the final state:  $K^-p \rightarrow \Sigma^\pm\pi^\mp$  followed by  $\Sigma^\pm \rightarrow n\pi^\mp$ . These modes (branching ratio  $\sim 50\%$ ) are characterized by the presence of two charged pions with momenta higher than 150 MeV/c in the final state. There are no other reaction modes in which  $\gamma$  rays are emitted along with two charged pions with momenta higher than 150 MeV/c. Thus, by tagging on two charged pions with momenta higher than 150 MeV/c, one can exclude all the reactions producing high-energy  $\gamma$  rays.

There is an additional important role of the tagging system. It serves to distinguish kaons stopped in hydrogen from those stopped in other materials and those which undergo in-flight decay or reactions in hydrogen. Since the lifetime of the charged  $\Sigma$  particle is short, the  $K^-p$  reaction and the  $\Sigma$  decay can be regarded as taking place approximately at the same point (some millimeters apart). Thus, the  $K^-p$  reaction position can be obtained as the vertex of the trajectories of the two charged pions. Also, the time taken by the kaon to slow down and come to rest in the hydrogen gas is several nanoseconds and it can be measured as the time difference between the kaon arrival into the target and the pion emission after the absorption. For stopped kaons, this time of flight is determined uniquely as a function of the range in hydrogen. In this way, the requirement that the two-pion vertex occurs inside the hydrogen volume and has an appropriate time of flight clearly selects only kaons stopping in hydrogen and forming kaonic-hydrogen atoms.

To achieve this two-pion tagging, the target was surrounded by two layers of scintillation counter arrays  $T1$  and  $T2$  (for the timing of the outgoing particles) and two layers of multiwire proportional chambers (MWPCs)  $C1$  and  $C2$  (for reconstruction of the particle trajectories), as shown in Fig. 13.

The utilized 600 MeV/ $c$  kaon beam was degraded by graphite ( $\sim 2.2$  g/cm $^3$ ) blocks so to stop kaons in the hydrogen gas. The average kaon intensity and the  $K/\pi$  ratio, both after the carbon target, were  $8 \times 10^3$  per spill and 1/90, respectively. The spill duration was 2 s and the repetition rate was one spill every 4 s. As for the x-ray detection, lithium-drifted Si(Li) x-ray detectors were used.

A removable  $^{55}\text{Fe}$  source was installed in the downstream cooling rod to irradiate all detectors through a small beryllium window, and the source was periodically inserted when the beam was off to check the resolution of the Si(Li) detectors.

For the *in situ* calibration, a titanium foil inside the target vessel was used as an in-beam energy calibration source to monitor the gain stability of the Si(Li) detectors. The foil was placed on a teflon plate in order to remove undesirable x rays from the material in the vessel.

The typical x-ray energy resolution was 410 eV (FWHM) at 6.4 keV, and the typical time resolution was 290 ns (FWHM); see Table V.

The x-ray spectrum obtained in the KpX experiment is shown in Fig. 14 (Iwasaki *et al.*, 1997). As shown in the figure, the  $K$ -series x rays are clearly seen, for the first time, at around 6 to 9 keV, with remarkable signal-to-noise ratio. The dashed line indicated as  $E_{e.m.}(K_\alpha)$  is the electromagnetic value for the  $2p \rightarrow 1s$  transition ( $6480 \pm 1$  eV). The  $K_\alpha$  peak, unambiguously observed, is located on the left on the  $E_{e.m.}(K_\alpha)$  line, which means that the  $1s$  strong-interaction shift is

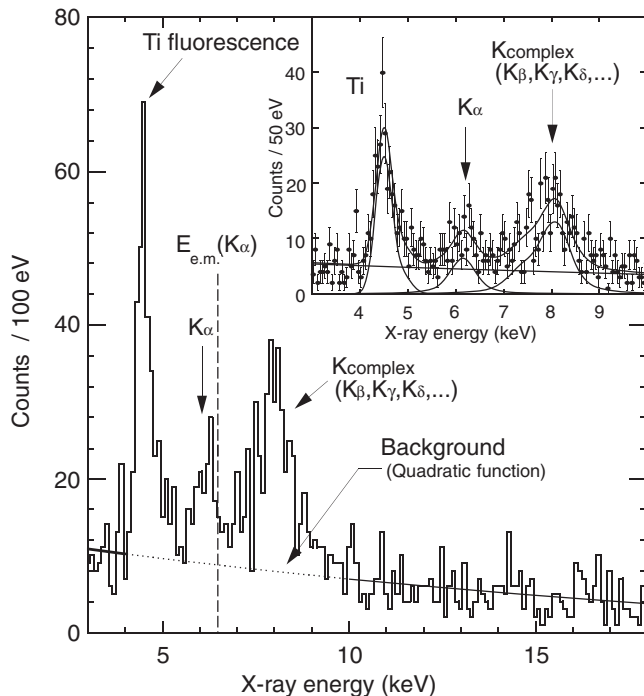


FIG. 14. The x-ray spectrum obtained by the KpX experiment. The inset is a close-up spectrum of the region of interest, together with the fit result. From Iwasaki *et al.*, 1997.

negative, namely, the  $1s$  energy level is shifted upward, turning out in a less bound ( $K^-p$ ) system due to the repulsive-type strong interaction.

The other peak structure near  $\sim 8$  keV, denoted as  $K_{\text{complex}}$ , can naturally be interpreted as a sum of all the higher  $K$ -series x rays.

The resulting shift and width of the kaonic-hydrogen  $1s$  level turned out as follows:

$$\epsilon_{1s} = -323 \pm 63(\text{stat}) \pm 11(\text{syst}) \text{ eV}, \quad (15)$$

and

$$\Gamma_{1s} = 407 \pm 208(\text{stat}) \pm 100(\text{syst}) \text{ eV}. \quad (16)$$

In Fig. 15, the shift and width obtained by the KpX experiment are compared with the results of three previous measurements (Davies *et al.*, 1979; Izycki *et al.*, 1980; Bird *et al.*, 1983), together with some of the analyses of the low-energy  $\bar{K}N$  scattering data (Kim, 1965; Sakitt *et al.*, 1965; Martin, 1981). In the figure, the DEAR results (Beer *et al.*, 2005) are also reported.

The sign of the shift obtained by KpX is opposite to those obtained in the previous experiments on kaonic hydrogen and is consistent with the analyses of low-energy  $\bar{K}N$  scattering data. The long-standing kaonic-hydrogen puzzle was definitely swept away.

### 3. The DEAR experiment at DAΦNE

#### a. Kaonic-hydrogen measurement

The primary goal of the DEAR proposal (Bianco *et al.*, 1999) at the  $e^+e^-$  DAΦNE collider of the Frascati National Laboratories of INFN was the precise determination of shift and broadening, due to strong interaction, of the fundamental level of kaonic hydrogen. The DEAR experiment (Beer *et al.*, 2005) took advantage of the clean (no contaminating particles),

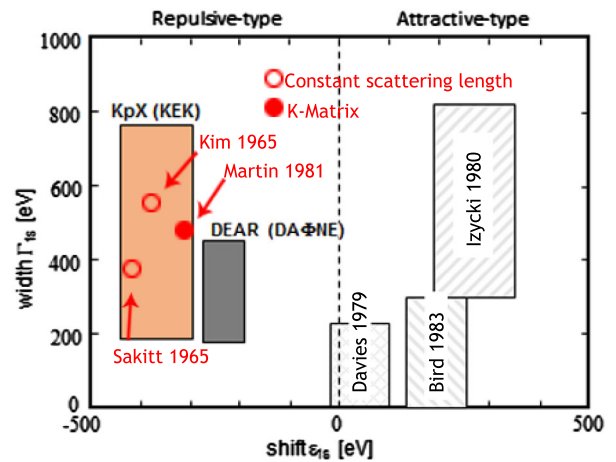


FIG. 15. The shift and width obtained by the KpX experiment are compared with the results of three previous measurements (Davies *et al.*, 1979; Izycki *et al.*, 1980; Bird *et al.*, 1983) and with some of the analyses of the low-energy  $\bar{K}N$  scattering data (Kim, 1965; Sakitt *et al.*, 1965; Martin, 1981). The DEAR result (Beer *et al.*, 2005) is also reported.

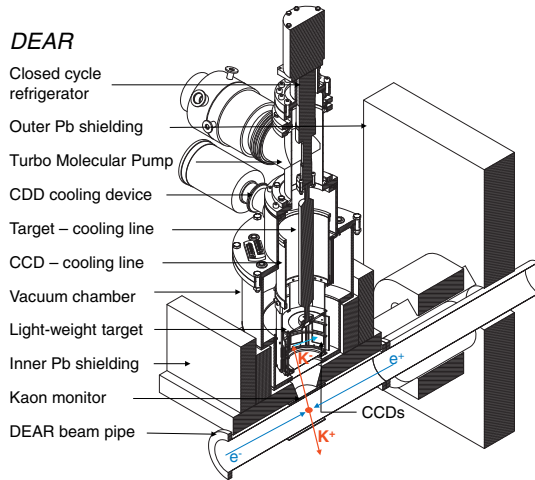


FIG. 16. Schematic view of the DEAR experimental setup; only the right outer lead wall shielding is shown.

low momentum ( $127 \text{ MeV}/c$ ), nearly monoenergetic ( $\Delta p/p = 0.1\%$ ) beam of kaons from the decay of  $\phi$  mesons produced by  $e^+e^-$  collisions in the DAΦNE collider.

The setup consisted of three components: a kaon detector, a cryogenic target system, and an x-ray detection system. Figure 16 shows a schematic view of the setup. The whole setup was installed in one of the two interaction regions of DAΦNE. The beam pipe surrounding the interaction point had a diameter of 90 mm and was made of aluminum 250  $\mu\text{m}$  thick with a 650  $\mu\text{m}$  carbon fiber reinforcement.

The kaon monitor also allowed the measurement of the absolute luminosity delivered by the machine.

CCDs were used as x-ray detectors. A vacuum chamber insulated the target cell and the CCDs. The target cell and the vacuum chamber were made of selected low- $Z$  materials, in order to reduce the fluorescence lines from excitation of the materials by the impinging kaons. An aluminum alloy ( $\text{AlMgSi}_{0.5}$ ) with the lowest possible manganese content was used for the vacuum chamber. The cylindrical target cell, 12.5 cm in diameter and 14 cm high, was constructed by 75  $\mu\text{m}$  Kapton foils (side wall and entrance window), a support structure made by thin epoxy-fiberglass bars with a top plate and an entrance ring of aluminum. Laboratory irradiations of all setup materials using strong x-ray sources revealed the presence of calcium and strontium in the epoxy-fiberglass bars. Gold ( $L$ -complex) electronic fluorescence lines showed up as well from the ceramic support of the CCDs. The aluminum bottom side of the target had a 100 mm diameter hole where kaons entered the target gas by passing through a 125  $\mu\text{m}$  Kapton window. Thin zirconium and titanium foils were placed on top of the target in order to use their fluorescence lines for in-beam energy calibration.

Because of the finite, although small, crossing angle (28 mrad) between electron and positron beams, the  $\phi$  particles were slightly boosted toward the outside of the DAΦNE rings. Therefore, the momenta of the two kaons in the  $K^+K^-$  pairs had a small angular dependence. Monte Carlo simulations to optimize the number of stopped kaons and the x rays detected by the CCDs were performed. The boost effect was

compensated by degraders composed of steplike multilayer Hostaphan foils.

A series of measurements with the target filled with nitrogen were performed previous to the kaonic-hydrogen one. The aim was to optimize the kaons stopping distribution and to characterize the machine background, by measuring kaonic nitrogen x-ray transitions whose yields were more than an order of magnitude higher than those of kaonic hydrogen (see Sec. IV.C.4).

Shielding the machine background was a major concern for the experiment (Bragadireanu *et al.*, 2001). As shown in Fig. 16, the interaction region was protected by two lead walls, each 200 mm thick and 1200 mm high. Additional lead shielding surrounded the DEAR beam pipe and the target cell. Using multilayer packages of materials having decreasing densities and atomic number (lead, copper, aluminum, polycarbonate), the low-energy x-ray background generated by the electromagnetic cascades of high-energy electrons or positrons, lost from the beams due to the Touschek effect (Bernardini *et al.*, 1963), was reduced by a factor of about 100.

For x-ray detection, 16 CCD55-30 chips were selected, covering a total area of 116  $\text{cm}^2$  facing the cryogenic target cell (see Sec. III.C.1).

The readout electronics was designed and built at Frascati National Laboratories. The data acquisition (DAQ) system allowed full flexibility in adjusting all CCD readout parameters for the optimal charge transport efficiency, while the quality of the conversion was improved by using 16 independent, high-precision analog digital converters (ADCs). The DEAR CCD readout system was described by Iliescu (2003), where the following topics are discussed: CCD operation, hardware implementation, DAQ performance, cluster analysis, exposure optimization, evaluation of the e.m. noise in the DAΦNE hall, charge transport correction, and the CCD final event structure.

In the kaonic-hydrogen measurement, data for  $58.4 \text{ pb}^{-1}$  of integrated luminosity ( $84.1 \times 10^6 K^-$ ) were collected. Furthermore, a measurement with no-colliding beams, i.e.,  $e^+e^-$  beams separated in the interaction region, was performed. These data represented the so-called “no-collisions background.”

The clean extraction of the kaonic-hydrogen x-ray spectrum required a careful treatment of the raw data. The applied procedure included several selection steps.

The so-called “cluster analysis” selected single and double pixel events (Ishiwatari *et al.*, 2006); see Sec. III.C.1. The number of hit pixels categorizes therefore the event type. Events having one or two hit pixels were selected as x-ray events to increase both the x-ray detection efficiency and the signal-to-noise ratio. The typical fraction for hit pixels per frame was about 3%–5%, such as to have an efficiency of hit recognition of about 98%–99%. The x-ray detection efficiency as a function of energy and the x-ray event loss due to pile-up effect were calculated by means of Monte Carlo simulations and laboratory tests.

The measured charge transport inefficiency was relatively low ( $\sim 10^{-6}$ /step during the image transfer and  $10^{-5}$ /step during the faster pixel transfer). The image transfer was therefore corrected using a linear compensation, while for

the pixel transport several formulas were tested, including linear, exponential, and power-law. The last one, chosen by the MIT-ACIS group too (Grant *et al.*, 2004), proved to be the most accurate. Small corrections were also applied for the inefficiency of the transfer between the output register and the node ( $< 10^{-4}$ , single step), as well as between the image region and the shift register ( $< 10^{-5}$ , single step). The parameters were obtained by fitting the 2D distributions (energy position) of two calibration lines (titanium and zirconium), for both central and trailing pixels, thus allowing a consistency check. The result of this procedure brought a relevant improvement to the energy resolution, from 214 eV (FWHM) to 176 eV at the  $K_\alpha$  line of copper (8040 eV), as well as a  $\sim 3.5\%$  increase of the single-pixel statistics.

Even without irradiation, CCDs have a charge pedestal due to the electronic noise. This “noise peak” was analyzed in the position and width at each measurement and data with broadened widths were rejected. From the position and width of the noise peak, a “noise threshold” was fixed: a pixel with charge above the threshold was regarded as a hit pixel. A small charge transfer inefficiency during readout created a position-dependent energy calibration. This well-known effect was corrected in the analysis routine.

An energy calibration procedure, based on fluorescence lines from setup materials, and from the titanium and zirconium foils placed on top of the target, was applied for each detector. Data of all individual detectors were then added. The overall resolution of the sum of detectors was determined: the values ranged from 130 eV (FWHM) for Ca  $K_\alpha$  (3.6 keV) to 280 eV for Zr  $K_\alpha$  (15.7 keV).

The energy spectrum, shown in Fig. 17, consists of a continuous background component, fluorescence lines from setup materials and from the titanium and zirconium foils, and the kaonic-hydrogen lines.

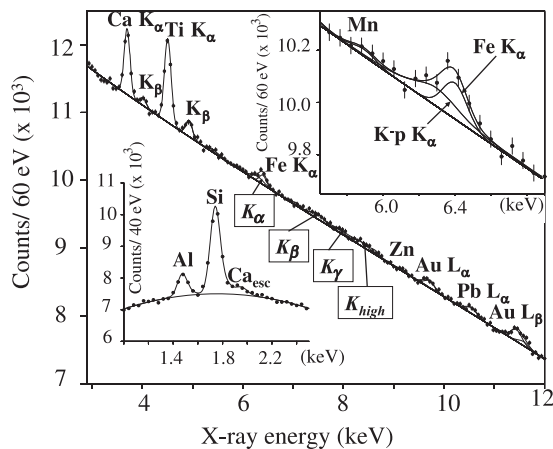


FIG. 17. The measured kaonic-hydrogen x-ray spectrum in the DEAR experiment. The kaonic-hydrogen transitions (indicated by boxes) and the electronic excitations coming from setup materials are visible. The fit functions (total and components) are shown. Upper-right inset: zoom of the kaonic-hydrogen  $K_\alpha$  transition region with the continuous background; the iron  $K_\alpha$  and the kaonic-hydrogen  $K_\alpha$  lines are disentangled. Lower-left inset: zoom of the silicon peak region with the aluminum, silicon, and calcium escape peaks. From Beer *et al.*, 2005.

Analysis of the kaonic-hydrogen  $K$  lines had to meet three crucial challenges: (i) determination of the continuous background shape, to which the width of the kaonic-hydrogen lines was very sensitive; (ii) disentanglement of the residual iron  $K_\alpha$  fluorescence line (coming from the setup components), which partially overlaps the kaonic  $K_\alpha$  signal; and (iii) dealing with the high  $K$ -series transitions  $K_\delta 5p \rightarrow 1s$  and higher ( $K_{\text{high}}$ ), which could not be resolved and had poorly known yields.

In order to face up at best these challenges, two independent analyses were performed. Both used Voigt functions with fixed Gaussian width for the detector resolution to fit the kaonic-hydrogen lines. In the fit the following parameters were used: intensities of  $K_\alpha$ ,  $K_\beta$ , and  $K_\gamma$ ; energy of  $K_\alpha$ ; and one Lorentzian width for all  $K$  lines, since the hadronic broadening comes from the ground state width only. The energy differences between  $K_\alpha$ ,  $K_\beta$ ,  $K_\gamma$ , and  $K_{\text{high}}$  were set to their electromagnetic values; see Table VI.

The two analysis methods differ essentially in the background spectrum which was used. Analysis I used the bulk of no-collisions data as background spectrum. A simultaneous fit of the two spectra, kaonic hydrogen and no collisions, was performed by constructing a  $\chi^2$  function as a sum of the two individual ones. The same shape of the continuous background component (a quadratic polynomial), apart from a normalization factor, was used to fit both spectra. All the fluorescence lines were normalized with the same factor.

Concerning the influence of the  $K_{\text{high}}$  transitions, the fit range was chosen from 2.9 to 10.4 keV, leaving aside the region between 7.74 and 8.82 keV, since “higher” transitions ( $n \geq 4 \rightarrow 1$ ), which could not be disentangled, contributed mainly in this energy range. In order to study the low-energy tails of the  $K_{\text{high}}$  complex, various values for the  $K_{\text{high}}/K_\gamma$  yield ratios, obtained from cascade calculations, were imposed in the fit. The effects of varying the yield ratios, as well as the fit energy range, were studied by Monte Carlo simulations and eventually included in the systematic error. In other words, the fit aimed at being independent of the shape of the  $K_{\text{high}}$  complex and thus avoid model dependency due to assumptions on this shape.

Analysis II used as a background spectrum the sum of kaonic nitrogen data (Ishiwatari *et al.*, 2004) and a subset (low CCDs occupancy) of no-collisions data.

Analyses performed in the laboratory, in a clean casing made out of Teflon and ultrapure aluminum, in which a

TABLE VI. Calculated values of the electromagnetic x-ray energies of the kaonic-hydrogen atom taking into account vacuum polarization effect, finite size effect, and relativistic recoil (Iwasaki *et al.*, 1997).

Transition	Line name	Energy (keV)
$2p \rightarrow 1s$	$K_\alpha$	6.480
$3p \rightarrow 1s$	$K_\beta$	7.678
$4p \rightarrow 1s$	$K_\gamma$	8.096
$5p \rightarrow 1s$	$K_\delta$	8.290
$6p \rightarrow 1s$	$K_\epsilon$	8.395
$7p \rightarrow 1s$	$K_\zeta$	8.459
$8p \rightarrow 1s$	$K_\eta$	8.501
$\infty \rightarrow 1s$	$K_\infty$	8.635

filtered x-ray tube beam (only bremsstrahlung, no lines) activated the various components of the setup, showed that the silicon and iron fluorescence lines originated from very close components (CCD itself and its support), in both signal and background spectra. Therefore, with circulating beams, where the machine background, constituted by electromagnetic showers and their subsequent activation products dominated by orders of magnitude of the hadronic component, the ratio between silicon and iron lines was expected to be independent of the kaons presence, constant through all data taking.

Consequently, the intensity ratio between the silicon fluorescence peak and the integrated continuous background in the two spectra (described by two independent cubic polynomials) was used to normalize the iron fluorescence peak in the kaonic-hydrogen spectrum.

The two analyses gave consistent results. In both, the fit without the ( $K^-p$ )  $K$ -series contribution gave a  $\chi^2/\text{NDOF} = 1.25$ , where NDOF indicates the number of degrees of freedom. By including ( $K^-p$ ) lines, in analysis I  $\chi^2/\text{NDOF}$  turned out to be 1.04, and in analysis II the value was 1.02. Figure 18 shows the kaonic-hydrogen x-ray spectra for both analyses, after continuous and structured background subtraction. The fitting curves of the various kaonic-hydrogen lines are also shown. Shifts and widths obtained in the two analyses are reported in the figure.

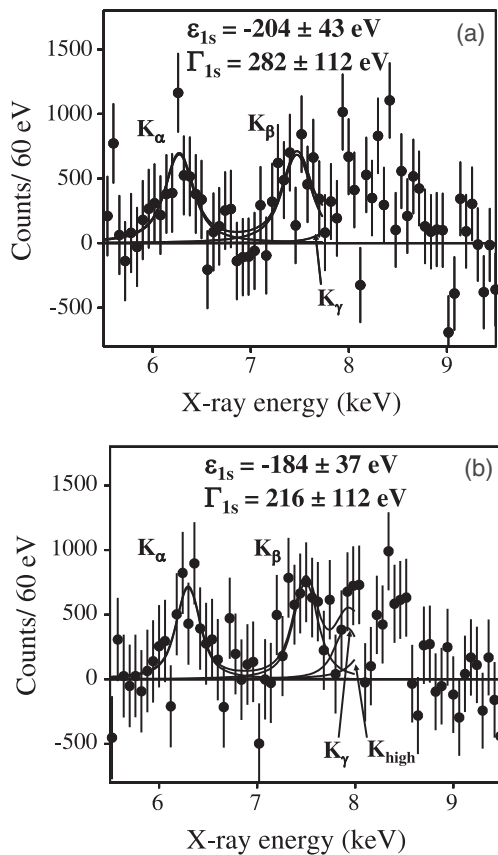


FIG. 18. The DEAR kaonic-hydrogen x-ray spectrum after continuous and structured background subtraction: (a) results of analysis I; (b) results of analysis II. The fitting curves of the various kaonic-hydrogen lines are shown. From Beer *et al.*, 2005.

The weighted average of the two independent analyses for the  $K_\alpha$  transition energy gave  $6287 \pm 37(\text{stat}) \pm 6(\text{syst})$  eV. The resulting weighted average of the ground state shift  $\epsilon_{1s}$  was

$$\epsilon_{1s} = -193 \pm 37(\text{stat}) \pm 6(\text{syst}) \text{ eV.} \quad (17)$$

The weighted  $1s$  ground state width  $\Gamma_{1s}$  was

$$\Gamma_{1s} = 249 \pm 111(\text{stat}) \pm 30(\text{syst}) \text{ eV.} \quad (18)$$

Systematic error contributions from detector energy calibration and energy resolution, as well as from the analyses procedures (fit range and method), were included.

The DEAR results were consistent with the KEK measurement (Iwasaki *et al.*, 1997), within  $1\sigma$  of their respective errors. The repulsive-type character of the  $K^-p$  strong interaction was confirmed.

The results obtained differ significantly, however, from the KEK ones in the following aspects: the uncertainty of the DEAR results was about twice smaller than that of the KEK values. Moreover, DEAR observed the full pattern of kaonic-hydrogen  $K$  lines, clearly identifying the  $K_\alpha$ ,  $K_\beta$ , and  $K_\gamma$  lines, with an intensity ratio  $1.1 \pm 0.5$  for  $K_\alpha/K_\beta$  [compatible with the cascade calculation of Jensen (2003a), within  $2\sigma$ ], and limiting the intensity of  $K_\gamma/K_\alpha$  to  $0.2 \pm 0.5$ . The statistical significance of the summed intensities of the  $K$  lines was  $6.2\sigma$ .

#### b. Kaonic nitrogen measurement

The observation of kaonic nitrogen x rays was performed during the first part of the DEAR scientific program (Ishiwatari *et al.*, 2004). Pressurized cooled nitrogen gas as a target was chosen, because the yields of kaonic nitrogen transitions are high enough to permit sufficiently fast feedback (see Sec. IV.C.4). The measurement had multiple tasks: in addition to the study of the machine background and the setup performance, to perform the first measurement of kaonic nitrogen transitions. In fact, no results had been published for kaonic nitrogen, apart from the exploratory measurement performed by DEAR of two previously unobserved transitions (Bragadireanu *et al.*, 2001). In the kaonic nitrogen measurement of DEAR, a pattern of three lines was clearly identified. The x-ray yields of these transitions were also determined. By using the experimental yields as input, information on atomic cascade could be obtained. In particular, the residual  $K$ -shell electrons population was determined. Data using the nitrogen target were taken for about one month (October 2002). The total collected integrated luminosity was  $17.4 \text{ pb}^{-1}$ , from which  $10.8 \text{ pb}^{-1}$ , taken in stable conditions, were selected for the analysis of the energy spectrum. In Fig. 19, the x-ray energy spectrum is shown, where three kaonic nitrogen x-ray lines are well identified: the  $6 \rightarrow 5$  transition at 7.6 keV, the transition  $7 \rightarrow 6$  at 4.6 keV, and the transition  $5 \rightarrow 4$  at 14.0 keV. The first and the third transitions overlap with the  $\text{Ti-}K_\alpha$  and  $\text{Sr-}K_\alpha$  lines. There are no fluorescence x-ray lines around 7.6 keV; thus the kaonic nitrogen peak at 7.6 keV could be fitted with a single Gaussian, as shown in the inset of Fig. 19. The FWHM of the  $6 \rightarrow 5$  transition line at 7588 eV turned out to be 161 eV. The other two kaonic nitrogen peaks

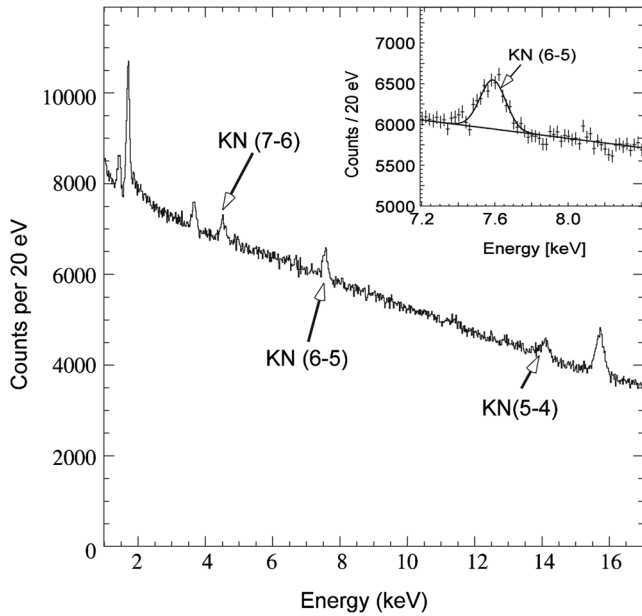


FIG. 19. Energy spectrum of kaonic nitrogen. The arrows show the positions of the kaonic nitrogen x-ray lines: the  $7 \rightarrow 6$  transition at 4.6 keV, the  $6 \rightarrow 5$  transition at 7.6 keV, and the  $5 \rightarrow 4$  transition at 14.0 keV. The peaks at 1.4, 1.7, 3.6, 4.5, 4.9, 11.5, 14.2, and 15.7 keV are the Al- $K_\alpha$ , Si- $K_\alpha$ , Ca- $K_\alpha$ , Ti- $K_\alpha$ , Ti- $K_\beta$ , Au (L complex), Sr- $K_\alpha$ , and Zr- $K_\alpha$  lines, respectively. In the inset, the fit of the  $6 \rightarrow 5$  (at 7.6 keV) transition is reported. From Ishiwatari *et al.*, 2004.

were fitted with multi-Gaussian functions, with energies fixed to known values for both the kaonic transitions and the titanium and strontium fluorescence excitations, to obtain their intensities, as shown in Fig. 20. From this fit, the yields of kaonic nitrogen transitions were extracted (reported in Sec. IV.C.4).

## B. Light kaonic atom precision measurements

### 1. The E570 experiment at KEK 12 GeV-PS

#### a. The kaonic helium discrepancy

A striking discrepancy of experiments versus theory has characterized the first measurements of the strong-interaction  $2p$  level shift in the  $3d \rightarrow 2p$  transition of kaonic helium-4.

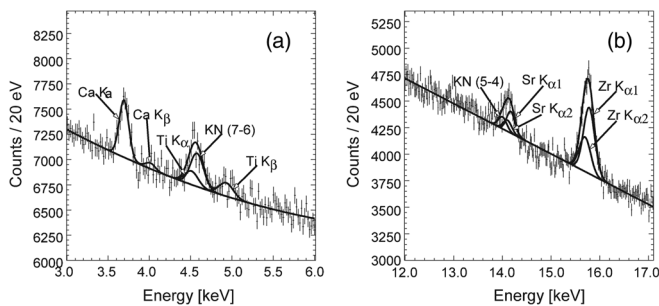


FIG. 20. Fit of the (a) ( $K^-N$ )  $7 \rightarrow 6$  (at 4.6 keV) and (b) ( $K^-N$ )  $5 \rightarrow 4$  (at 14.0 keV) kaonic nitrogen transitions. The kaonic peaks and the fluorescence lines of titanium and strontium are clearly separated. From Ishiwatari *et al.*, 2004.

The average of three kaonic helium-4  $2p$  level shift measurements (Wiegand and Pehl, 1971; Batty *et al.*, 1979; Baird *et al.*, 1983) was  $-43 \pm 8$  eV. The theoretical calculations of the shift by global fits to kaonic atom x-ray data on various nuclei, using both a phenomenological potential (Batty, Friedman, and Gal, 1997) and a SU(3) chiral unitary model (Hirenzaki *et al.*, 2000), were close to zero. Theory and experiments disagreed by more than 5 standard deviations. An accurate experimental determination of the energy shift of the  $2p$  level of kaonic helium-4 was compelling.

#### b. The kaonic-helium measurement

The aim of the E570 experiment at KEK (Okada *et al.*, 2007) was to measure the  $3d \rightarrow 2p$  transition energy of kaonic helium-4 to a precision such as to confirm or refute the large level shift measured in the previous experiments.

The experiment was carried out at the K5 beam line of the 12 GeV KEK Proton Synchrotron. The experimental apparatus was essentially the same as the former E471/E549 experiment (Sato *et al.*, 2008), with the inclusion of x-ray detectors and energy calibration foils in the cryostat of the helium target. The E570 setup is schematically shown in Figs. 21 and 22 (Okada *et al.*, 2007).

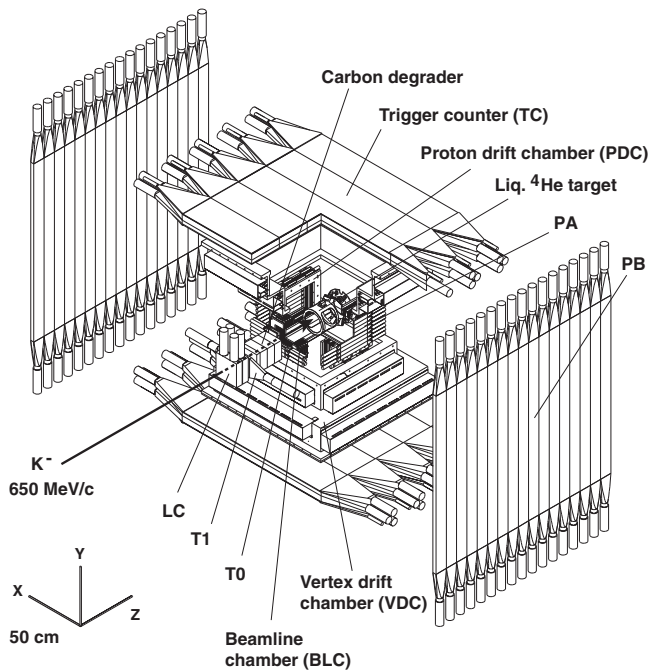


FIG. 21. Schematic drawing of the E570 experimental setup. The  $z$  axis is the beam direction, the  $x$  axis is the horizontal axis (the left of the beam view is positive), and the  $y$  axis is the vertical one (the top is positive). The 650-MeV/c negatively charged kaon beam is degraded by carbon layers and stopped in a superfluid liquid helium-4 target. Characteristic x rays generated from a kaonic-helium atom are measured by SDDs installed downstream of the target. LC: Lucite Cerenkov counter. T1 and T0: scintillation counters. BLC: beam line drift chamber. VDC: vertex drift chamber. PDC: proton drift chamber. TC: scintillation counter for the VDC. PA and PB: scintillation counters for the PDC.

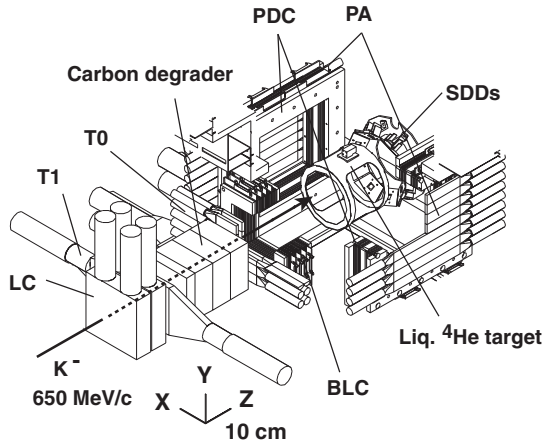


FIG. 22. Closeup of the E570 experimental setup (see the Fig. 21 caption).

The kaonic helium-4 atoms were produced by stopping  $K^-$  in a superfluid helium-4 target (cylindrical shape, 15 cm long and 20 cm in diameter, at the density of  $0.145 \text{ g/cm}^3$ ). The incident negatively charged kaons with momentum  $\sim 650 \text{ MeV}/c$  were degraded in carbon layers, counted with beam line counters, tracked by a high-rate beam line drift chamber and stopped inside the helium-4 target.

A significant improvement over the past experiments was achieved by implementing as x-ray detectors, eight SDDs, produced by KETEK GmbH, each having an effective area of  $100 \text{ mm}^2$  and  $260 \mu\text{m}$  thickness, with an energy resolution of  $\sim 190 \text{ eV}$  (FWHM) at  $6.4 \text{ keV}$  and a drift time of  $375 \text{ ns}$  (see Table V). The temperature of the SDDs was kept at  $\sim 83 \text{ K}$ . This improved the energy resolution by a factor of 2 as compared to Baird *et al.* (1983), who used a conventional Si (Li) detector. In addition, the statistics was higher by about a factor of 3.

Moreover, using the chambers and the counters constructed for the E549 experiment, the reaction vertices were reconstructed from the incoming  $K^-$  track and an outgoing charged particle [pions from the  $(K^-, \pi^-)$  reactions, or from hyperon decays]. The reaction vertices so reconstructed were imposed to be within the target: “fiducial volume cut.” This was in addition to the requirement of coincidence with the x-ray signal from the SDDs. The result was that the signal-to-noise ratio turned out improved by a factor of 6 as compared to Baird *et al.* (1983).

Finally, the energy calibration was done by using characteristic x-ray lines induced by charged particles (mostly  $\pi^-$  in the beam) on high-purity titanium and nickel foils placed just behind the target cell. The energy of the kaonic-helium  $3d \rightarrow 2p$  x rays ( $6.4 \text{ keV}$ ) lies just between the characteristic x-ray energies,  $4.5 \text{ keV}$  (titanium) and  $7.5 \text{ keV}$  (nickel) of the foils. In order to obtain high-statistics calibration spectra, SDD self-triggered events, together with the stopped- $K^-$  triggered events, were accumulated.

Figure 23 (top) shows a typical x-ray spectrum for SDD self-triggered events. Characteristic x-ray peaks of titanium and nickel were obtained with high statistics. The x-ray energy spectrum with stopped- $K^-$  triggered events is shown in

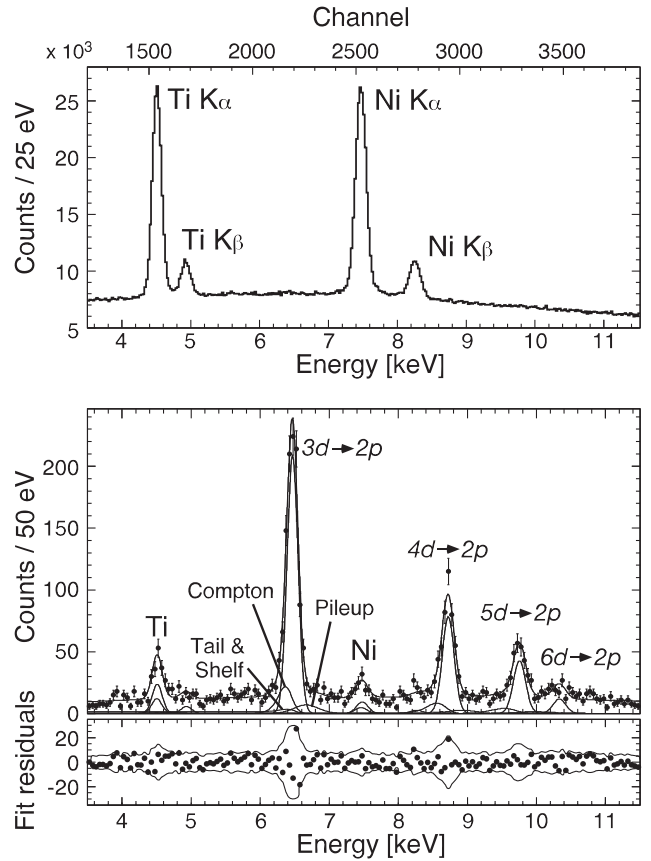


FIG. 23. The SDD kaonic helium-4 spectra (top) without and (bottom) with stopped  $K^-$ -triggered events. From Okada *et al.*, 2007.

Fig. 23 (bottom). Kaonic-helium  $3d \rightarrow 2p$ ,  $4d \rightarrow 2p$ , and  $5d \rightarrow 2p$  transitions are clearly observed.

For fitting the kaonic-helium x-ray peaks, a convolution of a Gaussian (representing the detector response) and a Lorentzian function (natural width), Voigt function, was adopted as the main-peak function. A Gaussian response was employed for fitting the characteristic x-ray peaks of the spectra, since their natural width was much smaller than the energy resolution of the SDDs.

Because of the large incoherent Compton total scattering cross section in liquid helium-4 ( $\sim 1 \text{ barn}$  at photon energies of  $\sim 10 \text{ keV}$ ), the low-energy tail due to the Compton scattering was taken into account. The convolution of an exponential function with a Gaussian was adopted for the spectral shape (called the “Compton tail function”). All parameters of the Compton tail function relative to the main peak were estimated by fitting the simulated x-ray energy spectra smeared with a Gaussian resolution function.

The kaonic helium-4 x-ray energy of the  $3d \rightarrow 2p$  transition was determined to be

$$E_{(3,d)} - E_{(2,p)} = 6467 \pm 3(\text{stat}) \pm 2(\text{syst}) \text{ eV}. \quad (19)$$

The other transition energies ( $4d \rightarrow 2p$  and  $5d \rightarrow 2p$ ) obtained in the fit are listed in Table VII. In Table VII, the electromagnetic values updated from Wiegand and Pehl

TABLE VII. The measured and the electromagnetic calculated (Koike, 2007) energies of  $3d \rightarrow 2p$ ,  $4d \rightarrow 2p$ , and  $5d \rightarrow 2p$  transitions, in kaonic helium-4. The quoted errors are purely statistical (Okada *et al.*, 2007).

Transition	$3d \rightarrow 2p$	$4d \rightarrow 2p$	$5d \rightarrow 2p$
Measured energy (eV)	$6466.7 \pm 2.5$	$8723.3 \pm 4.6$	$9760.1 \pm 7.7$
e.m. calculated energy (eV)	6463.5	8721.7	9766.8

(1971), Batty *et al.* (1979), and Baird *et al.* (1983) by Koike (2007), using the latest kaon mass value given by the particle data group (PDG) (Yao *et al.*, 2006), are also tabulated.

Since the strong-interaction shifts are negligibly small for the levels with the principal quantum number  $n$  larger than 2, the  $2p$  level shift  $\varepsilon_{2p}$  can be derived from the  $K$ -series x-ray energies using

$$\varepsilon_{2p} = (E_{(n,d)} - E_{(2,p)}) - (E_{(n,d)}^{e.m.} - E_{(2,p)}^{e.m.}), \quad (20)$$

where  $E_{(n,d)} - E_{(2,p)}$  and  $E_{(n,d)}^{e.m.} - E_{(2,p)}^{e.m.}$  correspond to the measured and calculated electromagnetic x-ray energies, respectively.

$\varepsilon_{2p}$  was calculated using Eq. (20) for each line and the statistical average was taken. The  $2p$  level shift then turned out to be consistent with zero:

$$\varepsilon_{2p} = 2 \pm 2(\text{stat}) \pm 2(\text{syst}) \text{ eV}. \quad (21)$$

Note that the electromagnetic energy and thus the energy shift are sensitive to the value of the kaon mass. If the kaon mass changes by 1 standard deviation from the PDG value of  $493.677(16) \text{ MeV}/c^2$  (Yao *et al.*, 2006),  $\varepsilon_{2p}$  changes by about 0.2 eV (Koike, 2007).

In conclusion, the E570 result excluded the earlier claim of a large experimental shift of about  $-40 \text{ eV}$  and solved the discrepancy between experiments and theory.

## 2. The SIDDHARTA experiment at DAΦNE

### a. Kaonic-hydrogen measurement

The SIDDHARTA experiment at LNF-INFN (Bazzi *et al.*, 2011a) on DAΦNE aimed at determining the kaonic-hydrogen  $1s$  shift and width with a higher precision than in DEAR (Beer *et al.*, 2005), using the large area SDDs with micro-second timing capability and good energy resolution, instead of the CCDs used in DEAR. The experiment took advantage, such as DEAR, of the excellent kaon beam delivered by DAΦNE.

Figure 24 shows a schematic view of the SIDDHARTA setup, which consisted of three main components: the kaon detector (described in Sec. IV.A.3), an x-ray detection system, and a cryogenic target system.

To obtain a uniform distribution of  $K^-$ 's momenta entering the gaseous target, a shaped degrader made of Mylar foils with a thickness ranging from 100 to  $800 \mu\text{m}$  was placed under the target, as shown in Fig. 24, taking into account the momentum boost ( $25.5 \text{ MeV}/c$ ) of the  $\phi$ 's resulting from the  $55 \text{ mrad}$   $e^+e^-$  crossing angle.

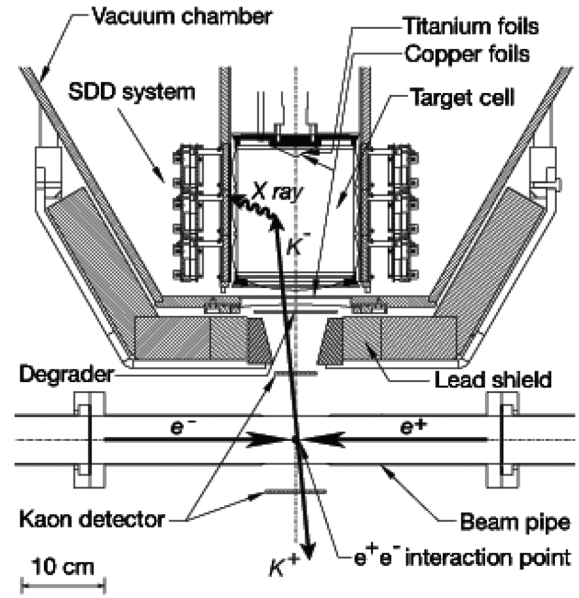


FIG. 24. Schematic view of the SIDDHARTA setup. From Bazzi *et al.*, 2011a.

The cylindrical target cell, 13.7 cm in diameter and 15.5 cm in height, was located just above the degrader inside the vacuum chamber. The lateral wall and the bottom window of the cell were made of Kapton polyimide film, 75 and  $50 \mu\text{m}$  thicknesses, respectively.

The SDDs used to detect the kaonic atom x rays are described in Secs. III.C.2 and III.C.3.

Figure 25 shows the time difference between the coincidence signals of the kaon monitor and the SDD events, from a set of data taken with the target filled with helium-3. The peak

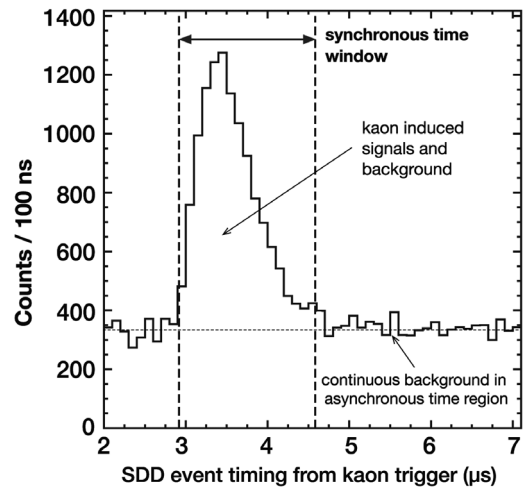


FIG. 25. Timing spectrum of a SDD. The spectrum is referred to as a dataset with target filled with helium-3. The peak corresponds to the time difference between the coincidence of the two scintillators of the kaon monitor and the x-ray events in the SDDs (triple coincidence). The peak region contains the kaon induced signals and background. The time window indicated by arrows was selected to identify synchronous events with charged kaons. The continuous asynchronous background was reduced by this timing cut. From Bazzi *et al.*, 2011c.

region contains the kaon induced signals (kaonic atom x rays) and background (gamma rays and charged particles from the  $K^-$  interactions and  $K^+$  decays). The tail of the distribution indicates the charge drift time in the SDDs. The time window indicated by the thick arrows was selected as synchronous events with charged kaons. The width of the timing window, from 2.4 to 4.6  $\mu\text{s}$ , was adjusted to maximize the signal-to-background ratio and the statistical precision of the determined kaonic atom x-ray energy. The performance on the reduction of the continuous asynchronous background depended on the timing resolution of SDDs. The source of the asynchronous background was mostly the gamma rays or minimum ionizing particles (MIPs) generated by the different timing of  $e^+e^-$  beams.

Using the coincidence between  $K^+K^-$  pairs and x rays measured by SDDs, the main source of background coming from beam losses was drastically reduced, resulting in an improvement of the signal-to-background ratio by more than a factor of 10 with respect to the corresponding DEAR ratio of about 1/100. The ratio signal over the machine background is improved by more than 4 orders of magnitude, for a kaon trigger rate of about 100 Hz and a time window of  $\sim 900$  ns. However, by giving up the detector pixel structure of CCDs, about 3 orders of magnitude in background rejection by topological selection were lost. The factor  $> 10$  comes entirely from the gain obtained by the timing in SIDDHARTA.

The readout system (Iliescu, 2009) was centered on the processing chain for the signals coming from the array of SDDs surrounding the target. The choice came from the characteristics of the detector and of the provided signals, which made it demanding in terms of data flow and timing. In particular, the overall active area (144  $\text{cm}^2$ ) was invested by a relatively large flux of particles, on the order of  $\sim 500$  Hz/ $\text{cm}^2$ , which corresponded, taking into account the digital integrators and the trigger detectors, to an average data flow of  $\sim 7$  MB/s. This amount would not represent a large number if the rate would come from events evenly distributed in time, but both accelerator background and x-ray kaonic events were produced in bursts of data, while the SDDs time response was slow (0.4–1  $\mu\text{s}$  transport, 2–3  $\mu\text{s}$  shaping) compared to the commonly used detectors in particle physics.

Since the bursts (e.m. showers) were randomly distributed in time and the long SDD processing imposed a complex event management and synchronization with the fast scintillator detectors, the required data processing speed was about 2 orders of magnitude higher. Moreover, being SIDDHARTA installed on DAΦNE after the major adaptations of the collider interaction region to the crab-waist configuration, the residual gas in the collider chamber and the nonoptimized initial optics produced a large amount of background.

Two types of data were taken with the  $e^+e^-$  beams colliding. The first type was the production of kaonic atom x-ray events taken with the kaon detectors and the Mylar degrader. The second type was the energy calibration of SDD detectors, taken every several hours with an x-ray tube activating titanium and copper foils. During the calibration runs, the kaon detectors were moved out, and the Mylar degrader was switched to a 50- $\mu\text{m}$ -thick copper foil on a

movable frame, so that no charged kaon could stop in the target. Then the x-ray tube placed beneath the beam pipe excited the titanium and copper foils.

To optimize the degrader thickness and the calibration procedures, the target was filled with helium gas and the  $L$  transitions of kaonic helium-4 were measured. Based on the high yield of these transitions, one day of measurements was sufficient (see Sec. IV.C.3). In addition, the first-ever exploratory measurement of kaonic deuterium  $K$ -series transitions was performed (see Sec. IV.B.2.c). In the kaonic-hydrogen analysis, it turned out to be essential the use of the kaonic deuterium spectrum to quantify the background lines originating from kaons captured in elements such as carbon, nitrogen, and oxygen contained in the setup materials. In fact, the deuterium target data had no peak structures of  $K^-d$  x rays due to their low yields (see Sec. IV.C.2) and broad natural widths.

Data were accumulated over six months in 2009, with an integrated luminosity of  $\sim 340$   $\text{pb}^{-1}$  for hydrogen and  $\sim 100$   $\text{pb}^{-1}$  for deuterium.

The data acquisition system recorded the signal amplitudes seen by the 144 SDD detectors along with the global time information. Whenever a kaon trigger occurred, the time difference between the x-ray event and the originating kaon was recorded, as well as the time correlations between the signals on each of the scintillators and the DAΦNE bunch frequency. From these data, the time-of-flight information of the kaon detector, the position of the hit on the detector, the rates of the SDDs, and the rate of kaon production could be extracted in the off-line analysis.

The timing distribution of the coincidence signals in the kaon detector with respect to the rf signal from DAΦNE clearly showed that kaon events could be separated from MIPs by setting the time gate as indicated in Fig. 26.

The refined *in situ* calibration in gain (energy) and resolution (response shape) of the summed spectrum of all SDDs was obtained using titanium, copper, and gold fluorescence lines excited by the uncorrelated background without trigger and also using the kaonic carbon lines from wall stops in the triggered mode.

A global simultaneous fit of the hydrogen and deuterium spectra was performed. Figure 27(a) shows the residuals of the measured kaonic-hydrogen x-ray spectrum after subtraction of the fitted background.  $K$ -series x rays of kaonic hydrogen were clearly observed, while those for kaonic deuterium were

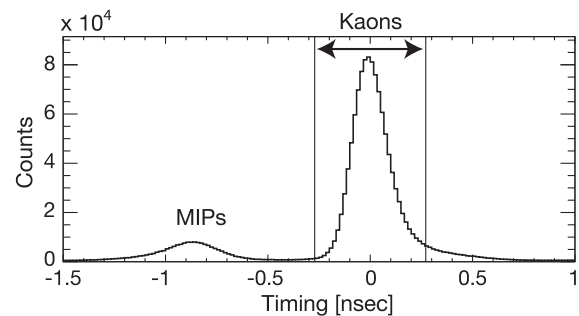


FIG. 26. Kaon identification using the timing of the coincidence signals in the kaon detector with respect to the rf signal of 368.7 MHz from DAΦNE. From Bazzi *et al.*, 2011a.

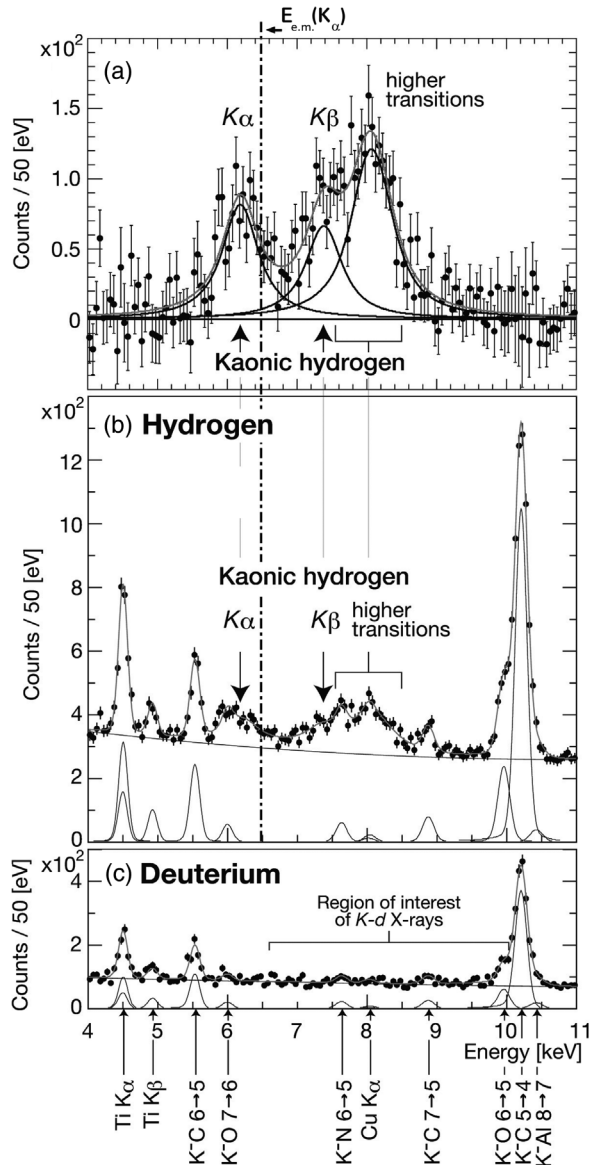


FIG. 27. The global simultaneous fit of the x-ray energy spectra of hydrogen and deuterium data. (a) Residuals of the measured kaonic-hydrogen x-ray spectrum after subtraction of the fitted background, clearly displaying the kaonic-hydrogen  $K$ -series transitions. The fit components of the  $K^-p$  transitions are also shown, where the sum of the functions is drawn for the higher transitions (greater than  $K_\beta$ ). (b), (c) Measured energy spectra with the fit lines. Fit components of the background x-ray lines and a continuous background are also shown. The dot-dashed vertical line indicates the e.m. value of the kaonic-hydrogen  $K_\alpha$  energy. From *Bazzi et al., 2011a*.

not visible (*Bazzi et al., 2011a*); see Sec. IV.C.2. Figures 27(b) and 27(c) show the fit result with the fluorescence lines from the setup materials and a continuous background.

The vertical dot-dashed line in Fig. 27 indicates the x-ray energy of kaonic hydrogen  $K_\alpha$ , calculated using the electromagnetic interaction only. Comparing the measured kaonic-hydrogen  $K_\alpha$  peak with the electromagnetic value, a repulsive-type shift (negative  $\epsilon_{1s}$ ) of the  $1s$ -energy level turned out.

Many other lines were detected in both spectra, as indicated with arrows in the figure. These kaonic atom lines result from

high- $n$  x-ray transitions of kaons stopped in the target cell wall made of Kapton ( $C_{22}H_{10}O_5N_2$ ) and its support frames made of aluminum. There are also characteristic x rays from the titanium and copper foils installed for calibration.

The response function of the SDD detectors was found to contain a slight deviation from a pure Gaussian shape, which could influence the determination of the strong-interaction width of the x-ray lines. The deviation from the pure Gaussian response was treated in two different ways to test systematic effects.

The first analysis used satellite peaks on the left and right flanks. The left flank is generally found in silicon detectors and is defined as a function having a feature decreasing exponentially in intensity toward lower energies (*Campbell et al., 2001*). The right flank could be interpreted as an effect of pile-up events and for its description a Gaussian was used (*Okada et al., 2007*).

In the second analysis, the correction of the “ideal” response was done by convoluting the Gaussian with a Lorentzian function (producing symmetric tails) and additionally with an exponential low-energy tail.

In both analyses, the kaonic-hydrogen lines were represented by Lorentz functions convoluted with the detector-response function, where the Lorentz width corresponds to the strong-interaction broadening of the  $1s$  state. The continuous background was represented by a quadratic polynomial function.

The region of interest of  $K^-d$  x rays is illustrated in Fig. 27(c). With the realistic assumption of 1 order of magnitude lower intensities than those of kaonic hydrogen (see Sec. IV.C.2), the influence of a possible kaonic deuterium signal on the kaonic-hydrogen result was found to be negligible.

In the kaonic-hydrogen spectrum, the higher transitions to the  $1s$  level,  $K_\gamma$  and above, produce an important contribution to the total intensity. The relative intensities of these lines, however, are only poorly known from cascade calculations and the free fit cannot distinguish between them, since their relative energy differences are smaller than their width, as seen in Fig. 27. As a result, fitting all the transitions at once leads to large errors on the shift and width of the  $1s$  level.

To minimize the influence of the higher transitions, the following iterative fitting procedure was adopted. In the first step, a free fit of all the transitions was performed, with the energy differences between the kaonic-hydrogen lines fixed to their e.m. differences, since the shifts and the widths of the levels higher than  $1s$  are negligible.

In the second step, the energies and widths of the higher transitions were fixed to the values found in the first step, and the spectra fitted leaving free all intensities and the common shift and width for  $K_\alpha$  and  $K_\beta$ , which were well resolved. With the new values for shift and width the described procedure was repeated until the values for shift and width converged, meaning that all the  $K$  lines had the same values for their shift and width, as it should be.

In the two independent performed analyses the event selection, calibration method, fit range, and detector-response function (as previously described) had been chosen independently. The comparison of the shift and width values gave a

direct measurement of the systematic error from the use of different procedures. The resulting shift values were consistent within 1 eV; however, the width differed by  $\sim 40$  eV, coming mainly from the use of different detector-response functions. For shift and width the mean values of the two analyses were quoted and the differences taken into account as systematic errors.

As a result, the  $1s$  level shift  $\varepsilon_{1s}$  and width  $\Gamma_{1s}$  of kaonic hydrogen were determined to be

$$\varepsilon_{1s} = -283 \pm 36(\text{stat}) \pm 6(\text{syst}) \text{ eV}, \quad (22)$$

$$\Gamma_{1s} = 541 \pm 89(\text{stat}) \pm 22(\text{syst}) \text{ eV}. \quad (23)$$

The quoted systematic errors are a quadratic summation of the contributions from the ambiguities due to the SDD gain shift, the SDD response function, ADC linearity, the low-energy tail of the kaonic-hydrogen higher transitions, the energy resolution, and the procedural dependence shown by the independent analyses.

This is the most precise measurement performed so far of the  $K$ -series x rays of kaonic-hydrogen atoms. This result was made possible by the use of new triggerable x-ray detectors, the SDDs, which lead to a much improved energy and time resolution over the past experiments KpX and DEAR, and much lower background in comparison with the DEAR experiment.

The SIDDHARTA strong-interaction  $1s$  energy level shift and width of kaonic hydrogen are plotted in Fig. 28, along with the results of the previous two measurements.

DEAR and SIDDHARTA measurements are compatible within their errors. However, the use of the background data in DEAR coming from beams not in collisions might have resulted in an underestimation of the Fe  $K_\alpha$  contribution to the

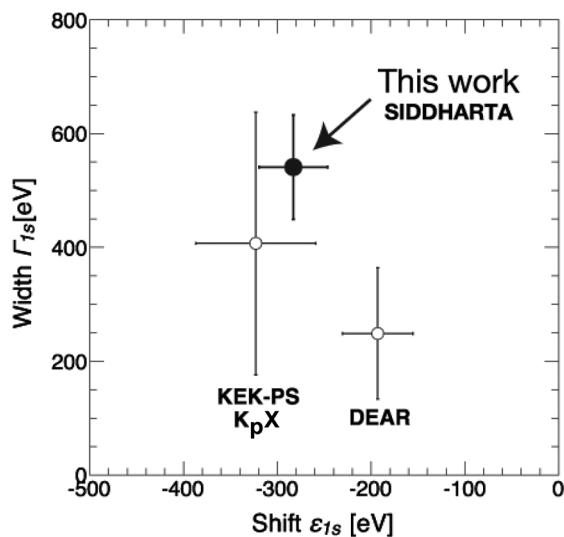


FIG. 28. Comparison of the experimental results for the strong-interaction  $1s$  energy level shift and width of kaonic hydrogen: KEK-PS KpX (Iwasaki *et al.*, 1997), DEAR (Beer *et al.*, 2005), and SIDDHARTA (Bazzi *et al.*, 2011a). The error bars correspond to quadratically added statistical and systematic errors.

fit, which has the effect of a smaller energy shift and width of the kaonic-hydrogen  $K_\alpha$  line.

All the measurements performed in the modern era show a negative shift, namely, a repulsive-type  $\bar{K}N$  interaction.

The precise determination of the shift and width provides new constraints on theories, having reached a quality which demands refined calculations of the low-energy  $\bar{K}N$  interaction (Ikeda *et al.*, 2011, 2012).

#### b. Kaonic helium-3 and helium-4 measurements

The discrepancy between experiments and theoretical calculations for the  $2p$  level shift of kaonic helium-4 was solved by the KEK-PS E570 experiment, using a liquid helium-4 target (Okada *et al.*, 2007). The SIDDHARTA experiment at the DAΦNE electron-positron collider measured, with silicon drift detectors, both the  $K^{-4}\text{He}$  and the  $K^{-3}\text{He } 3d \rightarrow 2p$  transitions using gaseous targets (Bazzi *et al.*, 2009, 2011c, 2012a). The use of gaseous targets avoided the weakening of the yields due to the Stark effect and, also, the necessity to take into account the systematic uncertainty of the Compton scattering of x rays inside the liquid helium target.

The SDD signals were calibrated with titanium and copper fluorescence x rays, assuming the linearity of the response of the SDD and the ADC. The SDDs were individually calibrated and the energy resolutions evaluated. In the analysis, 94 SDDs out of 114 with good energy resolution were selected. The achieved energy resolution of the sum over the 94 SDDs was  $\sim 150$  eV FWHM at 6 keV for the datasets of helium-4 and helium-3 targets.

During calibration runs, the x-ray tube produced a high intensity of titanium and copper fluorescence x rays. The Ti  $K_\alpha$  (4.5 keV) and Cu  $K_\alpha$  (8.0 keV) peak positions were used to determine the energy scale of each SDD. The gain drifts of SDDs were corrected by monitoring the Ti  $K_\alpha$  and Cu  $K_\alpha$  peak positions in each calibration run. Figure 29(a) shows the x-ray energy spectrum summed over 94 SDDs in the calibration runs. Figure 29(b) shows the x-ray energy spectrum of the self-triggered data, uncorrelated to the kaon triggers. The characteristic x rays of titanium, copper, and gold are seen on the continuous background.

This calibration method was not an *in situ* energy calibration in production runs. The typical count rate of a SDD in the calibration run (400 Hz) was 10 times higher than that in the production runs (40 Hz). This rate difference in the detector caused a gain shift; hence a correction was needed.

The peak stability versus time and rate was also checked (Bazzi *et al.*, 2011b) using the kaonic-helium x-ray lines by installing a thin titanium foil and a  $^{55}\text{Fe}$  source inside the setup (see Fig. 30). In Fig. 30(a), the shift in the peak position of the Mn  $K_\alpha$  line (5.9 keV) as a function of time (about two weeks) is plotted. The origin of the vertical axis is taken as an average of the peak positions in the whole data sample. A stability within  $\pm 2$ – $3$  eV was measured. This small instability was corrected up to a fluctuation of  $\pm 0.5$  eV of the peak position in the data analysis. In Fig. 30(b), the shift of the Mn  $K_\alpha$  peak position against hit rates of the SDDs is plotted. The origin of the vertical axis is taken as an average of the peak positions. The peak instability caused by hit rate dependence was found

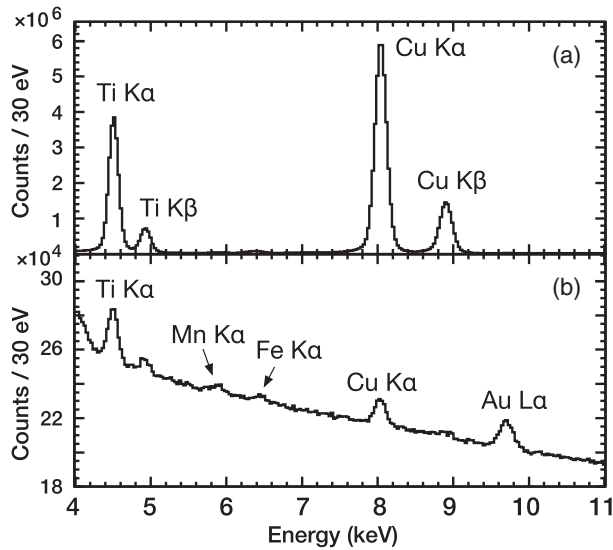


FIG. 29. X-ray energy spectra of the SDDs, where data of all the selected SDDs were summed: (a) data taken with the x-ray tube in the calibration runs, and (b) data uncorrelated to the kaon triggers in the production runs. The peak positions of the titanium, copper, and gold fluorescence x-ray lines in (b) were used to determine the uncertainty on the energy calibration and the energy dependence of the energy resolution. From [Bazzi \*et al.\*, 2011c](#).

to be about  $\pm 2$  eV, and it was corrected using the relation between rate and peak shift up to a fluctuation of  $\pm 0.5$  eV.

The x-ray peaks were fitted with the Voigt function  $V(\sigma, \Gamma) = G(\sigma) \otimes L(\Gamma)$ . The values of  $\sigma$  and  $\Gamma$  represent the resolution of detector response and the natural line width, respectively. In fitting the Ti  $K_\alpha$  and Cu  $K_\alpha$  peaks, intensity ratio, energy difference, and natural linewidths of the fine structure of  $K_\alpha$  x rays ( $K_{\alpha 1}$  and  $K_{\alpha 2}$  lines) were fixed.

The SDD detector response was assumed to be Gaussian. The detector resolution  $\sigma$  had an energy dependence expressed as  $\sigma(E) = \sqrt{a + bE}$  with the free parameters of white noise  $a$  and fluctuation of the number of charges  $b$ . The parameters were determined by fitting the three data points of Ti  $K_\alpha$ , Cu  $K_\alpha$ , and Au  $L_\alpha$  for the data uncorrelated to the kaon triggers; see Fig. 29(b).

Figure 31 shows the x-ray energy spectra of different target data, (a) deuterium (2.50 g/l), (b) helium-3 (0.96 g/l), (c) helium-4 (1.65 g/l), and (d) helium-4 (2.15 g/l). Several kaonic atom x-ray peaks are indicated for the deuterium target data. The x rays of kaonic carbon ( $K^-C$ ), kaonic nitrogen ( $K^-N$ ), and kaonic oxygen ( $K^-O$ ) were identified as produced from the Kapton polyimide used for the target cell and the target entrance window. The kaonic aluminum ( $K^-Al$ ) was also seen. It comes from the target cell frame and the structures of the SDDs. For the datasets of helium-3 and helium-4 targets, clear  $L_\alpha$  ( $3d \rightarrow 2p$ ) peaks are seen. Other Balmer series x rays can also be seen as smaller peaks. In the figure, the sum of the higher state transitions ( $n > 5$ ) is indicated as  $L_{\text{high}}$ .

In fitting the x-ray energy spectra, the peak positions of the  $K^-C$ ,  $K^-N$ ,  $K^-O$ , and  $K^-Al$  lines were fixed to the calculated

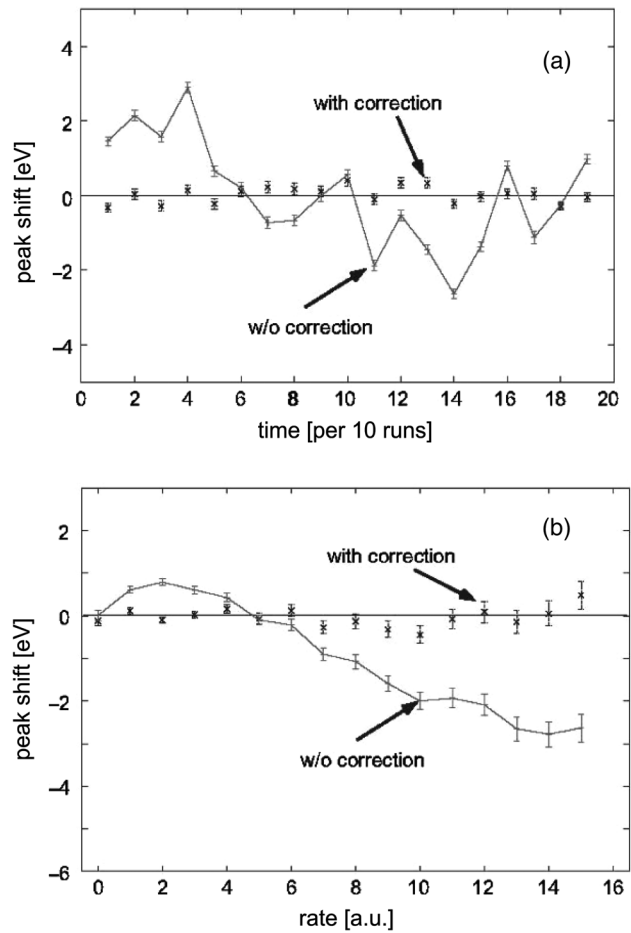


FIG. 30. The shift in the x-ray peak position of the Mn  $K_\alpha$  line (5.9 keV) as a function of (a) time and (b) rate. The origin of the vertical axis is the average of the data. With correction of the time and rate dependences, a stability of  $\pm 0.5$  eV was obtained. From [Bazzi \*et al.\*, 2011b](#).

values, because the energy shift and broadening due to the strong interaction are negligible in these high kaonic atom transitions. The Gaussian  $\sigma$  was also fixed by taking into account its energy dependence. A second order polynomial function was used to fit the continuous background. Then the  $L_\alpha$  energies and widths of the  $K^-3\text{He}$  and  $K^-4\text{He}$  atoms were determined.

Two datasets of helium-4 targets were merged. The systematic uncertainty was calculated as the quadratic sum of the individual contributions. The main contribution was the uncertainty of energy calibration ( $\pm 3.5$  eV) and the presence of the Mn  $K_\alpha$  and Fe  $K_\alpha$  x rays coming from the  $^{55}\text{Fe}$  source ( $\pm 2.0$  eV). Other contributions (e.g., effects of timing window selection and contributions of the kaonic oxygen line at 6.0 keV) were negligibly small.

The  $2p$ -state strong-interaction shift  $\varepsilon_{2p}$  was obtained from  $\varepsilon_{2p} = E_{3d \rightarrow 2p}^{\text{measured}} - E_{3d \rightarrow 2p}^{\text{e.m.}}$ , where  $E_{3d \rightarrow 2p}^{\text{measured}}$  is the experimental value of the x-ray energy and  $E_{3d \rightarrow 2p}^{\text{e.m.}}$  is the calculated electromagnetic energy with the quantum electrodynamics (QED) corrections. The strong-interaction shift of the  $3d$  state was negligibly small. The  $2p$ -state width  $\Gamma_{2p}$  was obtained from the fit value of the peak by fixing the Gaussian  $\sigma$ .

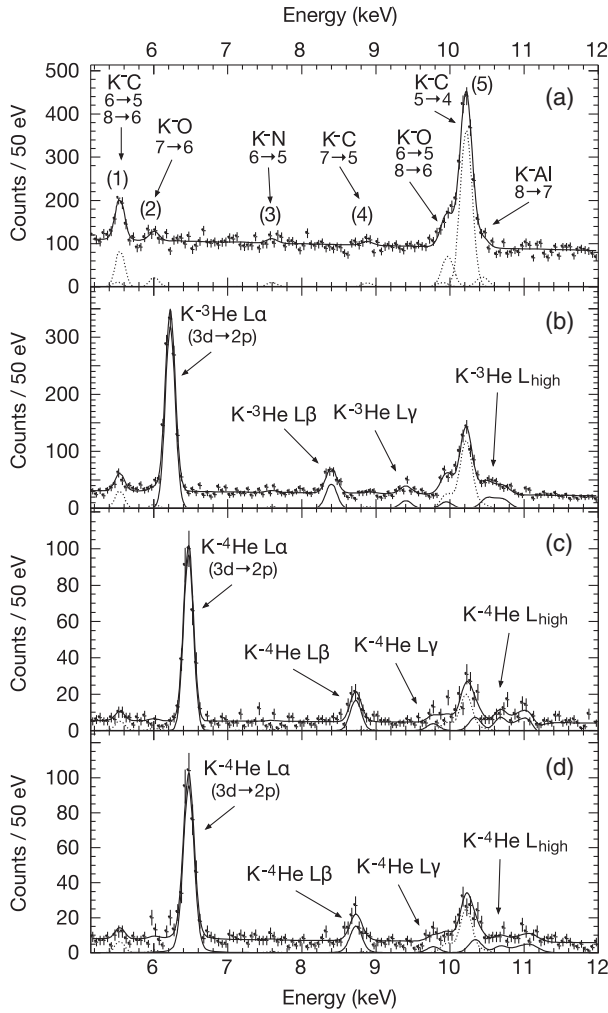


FIG. 31. X-ray energy spectra of different SIDDHARTA target data in the synchronous time window. (a) Deuterium (2.50 g/l), (b) helium-3 (0.96 g/l), (c) helium-4 (1.65 g/l), and (d) helium-4 (2.15 g/l). Several kaonic atom x-ray peaks are indicated by numbers for the deuterium target data: (1) kaonic carbon ( $K^-C$ )  $8 \rightarrow 6$  and  $6 \rightarrow 5$ , (2) kaonic oxygen ( $K^-O$ )  $7 \rightarrow 6$ , (3) kaonic nitrogen ( $K^-N$ )  $6 \rightarrow 5$ , (4) ( $K^-N$ )  $7 \rightarrow 5$ , (5) ( $K^-O$ )  $8 \rightarrow 6$  and  $6 \rightarrow 5$ , ( $K^-C$ )  $5 \rightarrow 4$ , and kaonic aluminum ( $K^-Al$ )  $8 \rightarrow 7$  transitions. The fit lines in the energy spectra are also shown. The dotted lines show the fit functions of the other kaonic atom x-ray lines produced in the Kapton foils and the aluminum frames. The solid lines show the fit functions of the kaonic-helium x-ray lines in (b), (c), and (d). The background was fitted with a second order polynomial function. The positions of the kaonic-helium x-ray lines in (b), (c), and (d) are indicated by arrows. Adapted from [Bazzi \*et al.\*, 2014](#).

The obtained values for  $\epsilon_{2p}$  and  $\Gamma_{2p}$  are ([Bazzi \*et al.\*, 2009, 2011c, 2012a](#)) as follows:

$$K^{-3}\text{He}: \epsilon_{2p} = -2 \pm 2(\text{stat}) \pm 4(\text{syst}) \text{ eV}, \quad (24)$$

$$K^{-4}\text{He}: \epsilon_{2p} = +5 \pm 3(\text{stat}) \pm 4(\text{syst}) \text{ eV}, \quad (25)$$

$$K^{-3}\text{He}: \Gamma_{2p} = 6 \pm 6(\text{stat}) \pm 7(\text{syst}) \text{ eV}, \quad (26)$$

$$K^{-4}\text{He}: \Gamma_{2p} = 14 \pm 8(\text{stat}) \pm 5(\text{syst}) \text{ eV}. \quad (27)$$

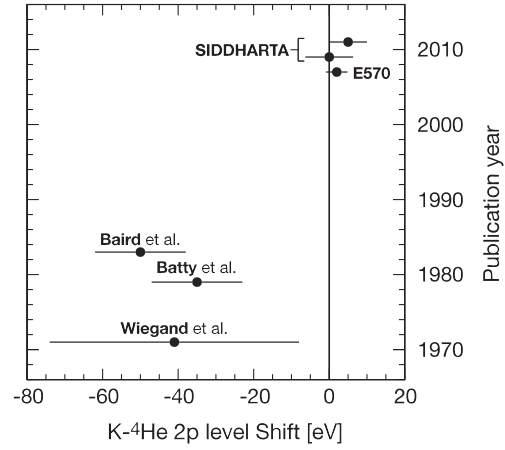


FIG. 32. Comparison of experimental results for the strong-interaction shift of the kaonic helium-4  $2p$  level. The plots exhibit results for the three old experiments ([Wiegand and Pehl, 1971](#); [Batty \*et al.\*, 1979](#); [Baird \*et al.\*, 1983](#)) and the recent two experiments E570 ([Okada \*et al.\*, 2007](#)) and SIDDHARTA publishing two values using different datasets in 2009 ([Bazzi \*et al.\*, 2009](#)) and in 2011 ([Bazzi \*et al.\*, 2011c](#)). The error bars correspond to quadratically added statistical and systematic errors.

The  $K^{-3}\text{He}$  measurements were realized for the first time. The main contribution to the systematic errors was the uncertainty on the fixed Gaussian  $\sigma$ . Even with clear peaks and low background, the precisions of  $\Gamma_{2p}$  were not enough to determine the linewidth, due to the 150 eV (FWHM) energy resolution of SDDs.

The  $K^{-4}\text{He}$  SIDDHARTA results for  $\epsilon_{2p}$  with gaseous target are consistent with the results of the KEK-PS E570 ([Okada \*et al.\*, 2007](#)) with liquid target, within the errors (Fig. 32).

### c. First exploratory measurement of kaonic deuterium

“The necessity to perform measurements of the kaonic deuterium ground state observables is justified by the fact that, unlike the case of pionic atoms, the measurement of only the kaonic hydrogen spectrum does not allow, even in principle, to extract independently both  $s$ -wave  $\bar{K}$ -nucleon scattering lengths  $a_0$  and  $a_1$ ” ([Meißner, Raha, and Rusetsky, 2006](#)).

On the theoretical side, there are many recent publications, reported in Table VIII, which give consistent values for shifts  $\epsilon_{1s}$  and widths  $\Gamma_{1s}$  of kaonic deuterium.

The SIDDHARTA experiment, after performing the most precise measurement on kaonic hydrogen ([Bazzi \*et al.\*, 2011a, 2012b](#)), made the first exploratory study of kaonic deuterium ([Bazzi \*et al.\*, 2013](#)).

For the fit, the kaonic deuterium  $K$ -series transitions were put in the model with the pattern of the transition energies taken from the electromagnetic values ( $E_{2p \rightarrow 1s} = 7820$  eV,  $E_{3p \rightarrow 1s} = 9266$  eV,  $E_{4p \rightarrow 1s} = 9772$  eV,  $E_{5p \rightarrow 1s} = 10006$  eV, etc.) ([Ishiwatari, 2007](#)). The strong-interaction shift was set to  $-805$  eV and the width to 750 eV, as representative values of theory predictions (see Table VIII). For the shape of the transitions, Voigt functions were used, with the (energy dependent) Gaussian  $\sigma$ , fixed by interpolating the values from

TABLE VIII. Compilation of predicted  $K$ - $d$  scattering lengths  $a_{K-d}$  and corresponding experimental observables  $\epsilon_{1s}$  and  $\Gamma_{1s}$ .

$a_{K-d}$ (fm)	$\epsilon_{1s}$ (eV)	$\Gamma_{1s}/2$ (eV)	Reference
$-1.58 + i 1.37$	-887	757	Mizutani <i>et al.</i> (2013)
$-1.48 + i 1.22$	-787	505	Shevchenko (2012)
$-1.46 + i 1.08$	-779	650	Doring and Meißner (2011)
$-1.42 + i 1.09$	-769	674	Gal (2007)
$-1.66 + i 1.28$	-884	665	Meißner, Raha, and Rusetsky (2006)
$-1.42 + i 1.60$	-670	508	Hoshino <i>et al.</i> (2017), Horiuchi <i>et al.</i> (2017)

the calibration lines. The background lines from kaonic x rays generated by kaons stopping in the foils of the target window were Gaussians, and the continuous background described by a quadratic polynomial. The relative intensities of the transition energies of kaonic deuterium were approximated to be the same as in the kaonic-hydrogen measurement (Bazzi *et al.*, 2011a). The results of the fit are shown in Fig. 33. No clear signal was observed.

The fit to the spectrum gave a total number of kaonic deuterium events  $N_X = 518 \pm 250(\text{stat}) \pm 180(\text{syst})$ .

By adding statistical and systematic errors quadratically one obtains  $N_X = 518 \pm 308$ , corresponding to a significance of  $1.7\sigma$ . The systematic error of  $N_X$  covers the dependence of the resultant intensity on the selection of the fit range and the background function, the channel binning, the choice of detectors, and the selected correlation time window.

### C. Atomic physics results

#### 1. Kaonic-hydrogen $K$ -series transition yields measurements by KpX and SIDDHARTA

In addition to the most precise measurement of  $\epsilon_{1s}$  and  $\Gamma_{1s}$ , SIDDHARTA obtained a new result for the yields of  $K^-p$

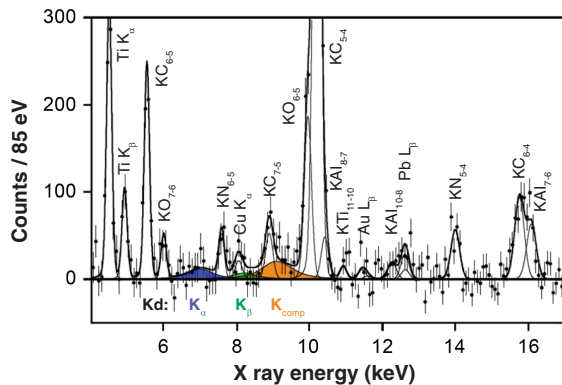


FIG. 33. X-ray spectrum of the exploratory kaonic deuterium measurement. The continuous background fit component is already subtracted. The fit was performed with fixed  $Kd$  transition shift and width ( $-805, 750$  eV) and fixed yield ratios of the  $K$  transitions. The integrated luminosity was  $100 \text{ pb}^{-1}$ . The lines from kaonic x rays generated by kaons stopping in the window foils as well as the fluorescence lines excited by background are labeled. Note the excess of events in the region of a possible signal. From Bazzi *et al.*, 2013.

$K$ -series x rays (Bazzi *et al.*, 2016). This information, not only important from an experimental point of view, is also essential to improve the cascade model calculations of kaonic hydrogen, which is a key topic for the experiment, but still poorly known. Before SIDDHARTA, only the KEK-PS KpX experiment obtained a value of the yield of  $K_\alpha$  (Iwasaki *et al.*, 1997):

$$Y_{K_\alpha} = 0.015 \pm 0.005 \quad (28)$$

and  $K_\alpha$ :  $K_{\text{tot}} = 0.27$  for  $10\rho_{\text{STP}}$  hydrogen gas target density.

In SIDDHARTA the dataset used to extract the yields corresponded to  $106 \text{ pb}^{-1}$  integrated luminosity. The target density was  $1.3 \pm 0.1 \text{ g/l}$ , which is about 15 times  $\rho_{\text{STP}}$ .

The absolute yield of transitions is given by the ratio between the number of measured x rays per kaon trigger ( $N_X/N_K$ ), namely, the experimental production efficiency  $\epsilon^{\text{exp}}$  and the corresponding quantities  $\epsilon^{\text{MC}}$  and  $N_X^{\text{MC}}/N_K^{\text{MC}}$  given by Monte Carlo (GEANT4, version 4.9.4) simulations:

$$Y = \frac{\epsilon^{\text{exp}}}{\epsilon^{\text{MC}}} = \frac{N_X/N_K}{N_X^{\text{MC}}/N_K^{\text{MC}}}. \quad (29)$$

Following the procedure adopted in determining  $\epsilon_{1s}$  and  $\Gamma_{1s}$ , a simultaneous fit of the hydrogen and deuterium spectra was performed for the data corresponding to the 97 SDDs which were operating stably with good energy resolution.

To obtain the number of kaonic-hydrogen x rays, the energy range for the fit was chosen to be from 4 to 11 keV, so covering all the  $K$ -series lines (see Table VI). The fit results showed, as for the analysis of the full dataset, a clearly identified  $K_\alpha$  line and a structure including transitions to  $1s$  from higher levels. These higher transitions produced an important contribution to the total intensity. Since the individual lines were overlapping, the relative intensities could not be assigned. To handle this uncertainty, an iterative fitting procedure, analogous to that used to extract  $\epsilon_{1s}$  and  $\Gamma_{1s}$ , was applied.

The absolute yields turned out to be (Bazzi *et al.*, 2016)

$$Y_{K_\alpha} = 0.012^{+0.004}_{-0.003}, \quad (30)$$

$$Y_{K_{\text{complex}}} = 0.030^{+0.009}_{-0.008}, \quad (31)$$

$$Y_{K_{\text{tot}}} = 0.043^{+0.012}_{-0.011}, \quad (32)$$

where  $K_{\text{complex}}$  includes all the transitions to  $1s$  from  $3d$  and higher energy levels and  $K_{\text{tot}}$  includes all the transitions to  $1s$ .

These results, together with the absolute yield of  $K_\alpha$  and the  $K_\alpha/K_{\text{tot}}$  ratio given by the KpX experiment, confirmed the density dependence of the yields predicted by cascade calculations; see Fig. 1.

A comparison between experiments and cascade calculation results for  $Y(K_\alpha)/Y(K_{\text{tot}})$  and  $Y(K_\alpha)$  allows one to obtain an estimation of  $\Gamma_{2p}^{\text{had}}$ , as discussed by Jensen and Markushin (2003).

## 2. Kaonic deuterium transition yields measurement by SIDDHARTA

To extract limits on the yields of the kaonic deuterium transitions, one needs to calculate the experimental efficiencies. The chain of processes starting from the produced  $\phi$  mesons was simulated. Two independent Monte Carlo simulations were performed using GEANT3 and GEANT4 routines. The  $\phi$ 's momentum was given by the crossing angle of electrons and positrons (55 mrad) and resulted in a horizontal boost of 25.5 MeV/ $c$ . The decay to charged kaon pairs is adapted to a  $\sin^2(\theta)$  distribution, as expected.

The charged kaons were followed along their tracks through the various materials of the setup (beam pipe, air, scintillators of the kaon trigger, degrader, vacuum window, target window, and finally the target gas). When a negative kaon is stopped in the target or in the setup materials, a routine started the tracks corresponding to the kaon-absorption products. For the case of deuterium, these products are  $\Sigma$ 's or  $\Lambda$ 's, pions and nucleons. The kaonic x rays were generated isotropically with a yield of 100%. Following these x rays, the attenuation was treated by a user routine and finally the eventual absorption in the SDDs was registered.

The relevant number to derive an absolute kaonic deuterium x-ray yield from the experimental data was the calculated *efficiency per trigger*  $W$ , defined as  $Kd$  x rays detected in the SDDs per each kaon pair detected in the kaon trigger (for 100% x-ray yield and data from 100 SDDs). The contributions to the systematic error are shown in Table IX, and a compilation of materials in Table X.

After averaging the two Monte Carlo efficiency calculations, being consistent within errors, and using the larger errors, the efficiency per trigger  $W$  turned out to be

$$W = 0.00752 \pm 0.00128. \quad (33)$$

Putting together the numbers of deuterium events (see Sec. IV.B.2.c) with the number of detected kaon pairs, the efficiency, and correction factors (e.g., dead time), the following yield values were obtained.

Total  $Kd$   $K$ -series yield:

$$Y(K_{\text{tot}}) = 0.0077 \pm 0.0051 \quad (34)$$

which corresponds to  $Kd$   $K_\alpha$  yield:

TABLE IX. Sources of systematic errors contributing to the calculated efficiency.

Error source (uncertainty)	Contribution to efficiency error
Total material thickness ( $\pm 7$ mg/cm <sup>2</sup> )	$\pm 9\%$
Size of $e^+e^-$ collision zone ( $\pm 5$ mm)	$\pm 8\%$
Setup geometry, distance from interaction point ( $\pm 5$ mm)	$\pm 7\%$
Variation in $e^+e^-$ crossing angle ( $\pm 2$ mrad)	$\pm 4\%$
Gas density ( $\pm 2\%$ )	$\pm 3\%$
Statistical error in Monte Carlo simulation	$\pm 3\%$
Central value of beam tune ( $\pm 0.4$ MeV)	$\pm 4\%$
Quadratic sum of above	$\pm 17\%$

TABLE X. Compilation of setup materials which the kaons are passing. Because of the  $\phi$  boost the kinetic energy of kaons is direction dependent; this effect is compensated by a shaped degrader consisting of stripes of 2 cm wide foils of varying thickness.

Description	Thickness (mm)	Thickness (mg/cm <sup>2</sup> )
Beam pipe window (Al)	0.400	108.0
Air	141.0	17.0
Plastic scintillator	1.450	150.0
Scintillator wrapping (tape)	0.500	71.0
Scintillator wrapping (Al)	0.006	1.62
Uniform degrader (Mylar)	0.175	24.3
Shaped degrader (Mylar)	0.200–0.700	27.8–93.7
Light shield (paper)	0.120	96.0
Vacuum window (Kapton)	0.125	177.5
Calibration foil (titanium)	0.025	11.3
Target window (Kapton)	0.100	14.2
Sum of above	144.101–144.601	698.7–764.6

$$Y(K_\alpha) = 0.0019 \pm 0.0012. \quad (35)$$

Such values are compatible with what is expected, namely, a yield of a factor about 10 smaller than the kaonic-hydrogen yield, estimated to be between 1% and 2% for  $K_\alpha$ ; see the cascade calculation predictions (Koike, Harada, and Akaishi, 1996; Jensen, 2004; Raeisi and Kalantari, 2009; Faber *et al.*, 2011). The larger absorption in the  $2p$  state (larger  $\Gamma_{2p}$ ) in the case of kaonic deuterium atoms, as compared to kaonic hydrogen, causes the lower  $K_\alpha$  yield.

From the yield values previously given, the upper limits for the yields turned out to be (C.L. 90%)  $Y(K_{\text{tot}}) < 0.0143$  and  $Y(K_\alpha) < 0.0039$  (Bazzi *et al.*, 2013).

## 3. Kaonic helium-4 and helium-3 transition yield measurements by SIDDHARTA

The absolute yields of  $L$ -series x rays of  $K^{-3}\text{He}$  and  $K^{-4}\text{He}$  were determined by SIDDHARTA for the first time (Bazzi *et al.*, 2014). The results are shown in Table XI. The yields of the  $L_\alpha$  x rays in gas are about twice as high as those in liquid ( $\sim 9\%$ ). On the other hand, the yields of the  $L_\beta$  and the  $L_\gamma$  x rays are similar in gas and in liquid. The intensities of the  $L_{\text{high}}$  lines in gas are higher than those in liquid. These yield differences are related to the density dependence of the cascade processes, such as the molecular Stark effect (Day and Snow, 1960) and molecular ion formation (Russell, 1978) in exotic helium atoms.

## 4. Kaonic nitrogen transition yield measurement by DEAR

To estimate the transition yields of the kaonic nitrogen measurement performed by DEAR, Monte Carlo calculations to evaluate the kaon stopping efficiency in the target gas, the x-ray absorption in gas and in the target windows, and the CCD quantum efficiency were performed.

Table XII contains a summary of the results for the yields of the  $(K^-N) 7 \rightarrow 6$ ,  $(K^-N) 6 \rightarrow 5$ , and  $(K^-N) 5 \rightarrow 4$  kaonic x-ray transitions in nitrogen. The measured numbers of events in the corresponding lines were compared with the predicted number of events from the Monte Carlo simulations in which

TABLE XI. Absolute x-ray yields of  $K^{-3}\text{He}$  and  $K^{-4}\text{He}$  measured with the SIDDHARTA gaseous targets. The yields are shown in percentages per stopped  $K^{-}$ . The experimental results for liquid helium-4 are shown in the last two columns: column 5 (Wiegand and Pehl, 1971); column 6 (Baird *et al.*, 1983), where the value of  $L_{\text{high}}$  in the liquid helium-4 data of Baird *et al.* (1983) includes the contribution of  $L_{\delta}$  only.

Transition	helium-3 (0.96 g/l)	helium-4 (1.65 g/l)	helium-4 (2.15 g/l)	helium-4 (liquid)	helium-4 (liquid)
$L_{\alpha}$ ( $3d \rightarrow 2p$ )	$25.0^{+6.7}_{-5.8}$	$23.1^{+6.0}_{-4.2}$	$17.2^{+2.6}_{-9.5}$	$9.2 \pm 2.4$	$8.9 \pm 4.5$
$L_{\beta}$ ( $4d \rightarrow 2p$ )	$3.6^{+1.3}_{-0.7}$	$4.2 \pm 1.1$	$3.1^{+0.6}_{-1.6}$	$5.2 \pm 1.3$	$2.3 \pm 1.2$
$L_{\gamma}$ ( $5d \rightarrow 2p$ )	$1.3^{+0.5}_{-0.4}$	$1.3 \pm 0.6$	$0.7^{+0.3}_{-0.5}$	$2.4 \pm 0.7$	$1.6 \pm 0.8$
$L_{\text{high}}$	$5.2 \pm 2.1$	$6.9^{+2.0}_{-1.9}$	$4.1^{+1.1}_{-2.1}$	...	$0.4 \pm 0.3$

the yields were assumed to be 100%. The systematic error of the calculation was estimated to be about 10%. In the last line of Table XII the final results of the measured yields including statistic and systematic errors at a density  $\rho = 3.4\rho_{\text{NTP}}$  are reported. There is the tendency that the yield increases in going from ( $K^{-}\text{N}$ )  $7 \rightarrow 6$  to the ( $K^{-}\text{N}$ )  $6 \rightarrow 5$  and ( $K^{-}\text{N}$ )  $5 \rightarrow 4$  transitions.

Understanding the atomic cascade processes in kaonic nitrogen is especially important due to the possible role of this exotic atom for a precise determination of the charged kaon mass, still an open problem. In fact, the determination of meson masses from the x-ray energies of mesonic atoms requires the measurement of transitions which must not be affected by the strong interaction. The levels involved are therefore of relatively high principal quantum numbers and are influenced by interaction with the electron clouds. Evaluation of the status of the electron shells and, therefore, of the importance of the electron screening, is difficult to assess, since it depends on the balance between the Auger emission and the electron refilling. For solids, the evaluation of electron screening is not straightforward, whereas in gaseous targets a high degree of ionization was observed in antiprotonic (Bacher *et al.*, 1988) and muonic (Bacher *et al.*, 1989) noble gases (neon, argon, and krypton).

In kaonic atoms with  $Z > 2$ , the deexcitation takes place in a competition mainly between electron ejection due to the Auger effect and radiative transitions. The Auger transition rates for emitting  $K^{-}$  and  $L^{-}$  shell electrons were evaluated by first order perturbation theory (Burbidge and de Borde, 1953; de Borde, 1954). In the cascade calculation, both  $K^{-}$  and  $L^{-}$  shell electron refilling processes were taken into account. In a gas target at the density used, the  $L^{-}$  shell refilling is expected to be negligibly small compared to other processes.

Using the measured values for the transition yields as input, a cascade calculation was performed to evaluate the screening effect due to the  $K^{-}$  and  $L^{-}$  shell electron population (Ishiwatari *et al.*, 2004).

The cascade calculation performed by DEAR started from  $n \sim 30$  with a modified statistical distribution  $P(l) \propto (2l+1)\exp(-al)$ , where  $a$  is a free parameter. The electron refilling rates for  $K^{-}$  and  $L^{-}$  shells were also free parameters in the calculation, as well as the shell filling probabilities at the start. The nuclear absorption rate was obtained by numerically solving the Klein-Gordon equation with the phenomenological  $K^{-}$ -nucleus potential of Batty, Friedman, and Gal (1997). In this potential, several nuclear bound states appear below the atomic states, but the transition to such nuclear state was ignored. In the circular orbit, nuclear absorption dominates for  $n \leq 3$  states.

The cascade parameters were adjusted to reproduce the experimental yields. The best-fit cascade parameters with their uncertainties are reported in Table XIII.

Since the  $8 \rightarrow 6$  x-ray energy transition (about 7.55 keV) is very close to the  $6 \rightarrow 5$  one (7.59 keV), the fit was done by assuming that the observed “ $6 \rightarrow 5$ ” yield is the sum of the  $6 \rightarrow 5$  and  $8 \rightarrow 6$  yields. The calculated x-ray yields using the best fit cascade parameters are shown in Table XIV.

As for the  $L^{-}$  shell refilling rate, an eventual conflict between thermalization and Coulomb explosion, as observed in the case of pionic nitrogen (Siems *et al.*, 2000), did not show up within the achieved accuracy and the cascade model. Within the uncertainty of the parameters in Table XIII, it was found that for the  $n = 6$  level a  $K^{-}$  shell electron fraction of approximately 1%–3% could be expected at a density  $\rho = 3.4\rho_{\text{NTP}}$ . After the kaon cascades along the circular orbits, the kaonic atom is almost completely ionized at  $n = 6$  and no refilling occurs at  $n \leq 6$ . The transitions from the  $\Delta n = 2$  noncircular orbits, where the  $K^{-}$  shell refilling is important, contribute to the  $K^{-}$  shell electron fraction, but it seems doubtful to conjecture their contribution in view of the simple model used. The residual population is important to be measured because cascade calculations still need a lot of experimental input to fine-tune all the involved rates to fit observables.

TABLE XII. Yields of kaonic nitrogen x rays at a density  $\rho = 3.4\rho_{\text{NTP}}$ . Measured and Monte Carlo estimated numbers of events assuming a 100% yield are tabulated. The yields are calculated using the experimental values divided by the simulated ones.

Transition	$7 \rightarrow 6$	$6 \rightarrow 5$	$5 \rightarrow 4$
Calculated energy (keV)	4.577	7.595	14.000
Measured number of events	$3310 \pm 690$	$5280 \pm 380$	$1210 \pm 320$
Monte Carlo number of events	$7971 \pm 796$	$9590 \pm 962$	$2108 \pm 210$
Yield	$41.5 \pm 8.7(\text{stat}) \pm 4.1(\text{syst})\%$	$55.0 \pm 3.9(\text{stat}) \pm 5.5(\text{syst})\%$	$57.4 \pm 15.2(\text{stat}) \pm 5.7(\text{syst})\%$

TABLE XIII. Best-fit cascade parameters for kaonic nitrogen in the  $\chi^2$  fit to the x-ray yields and their uncertainty within  $1\sigma$ 

$K$ -shell refilling rate	$(1.10_{-0.03}^{+1.22}) \times 10^{12} \text{ s}^{-1}$
$L$ -shell refilling rate	$(0.00_{-0.00}^{+0.01}) \times 10^{12} \text{ s}^{-1}$
Initial $K$ -shell refilling probability	$0.15_{-0.01}^{+0.15}$
Initial $L$ -shell refilling probability	$0.49_{-0.08}^{+0.11}$
$a$ [in $\exp(aI)$ ]	$0.05 \pm 0.01$

Jensen (2003b) independently performed a cascade calculation for kaonic nitrogen and the  $K$ -shell electron population was estimated to be  $\sim 2\%$  at  $n = 6$  in agreement with the DEAR cascade results.

## V. PLANNED EXPERIMENTS

### A. Kaonic deuterium

The kaonic deuterium x-ray measurement represents the most important experimental information missing in the low-energy antikaon-nucleon interactions field (see also Sec. IV.B.2.c). Two dedicated measurements are planned in the coming years at DAΦNE and J-PARC. The possibility to have two independent measurements on a lepton and a hadron machine, with two different beam-correlated background sources, will give an additional control on systematic errors, which is indeed important in order to extract a weak and a broad signal under high background conditions.

#### 1. Experimental requirements for kaonic deuterium experiments

The experimental challenge of the kaonic deuterium measurement is the very small kaonic deuterium x-ray yield (1 order of magnitude less than for hydrogen, see Sec. IV.C.2), the even larger width, and the difficulty to perform x-ray spectroscopy in the high radiation environments of the machines delivering kaons. The kaonic deuterium measurements at DAΦNE and at J-PARC require a large area x-ray detector, with good energy and timing resolution and stable working conditions, even in the high accelerator background environment. Moreover, it is necessary to have a dedicated veto detector system, to improve by at least 1 order of magnitude the signal-to-background ratio, as compared to the kaonic-hydrogen measurement performed by SIDDHARTA. A dedicated cryogenic lightweight gaseous target system is mandatory.

##### a. Large area x-ray detector system

To meet the stringent requirements for the kaonic deuterium measurement, new monolithic SDD arrays have been

TABLE XIV. Calculated x-ray yields for  $\Delta n = 1$  and  $\Delta n = 2$  transitions in kaonic nitrogen using the best-fit cascade parameters given in Table XIII.

$7 \rightarrow 6$	41.2%	$8 \rightarrow 6$	6.4%
$6 \rightarrow 5$	49.0%	$7 \rightarrow 5$	7.2%
$5 \rightarrow 4$	56.8%	$6 \rightarrow 4$	6.9%
$4 \rightarrow 3$	64.0%	$5 \rightarrow 3$	6.0%

developed by the Fondazione Bruno Kessler (FBK) and Politecnico di Milano, Italy. The SDD array consisting of eight square SDD cells, each with an active area of  $8 \times 8 \text{ mm}^2$  arranged in a  $2 \times 4$  array format, was described in Sec. III.C.4. A new advanced production technology allows one to set up the cryogenic target and detector systems with an efficient detector packing density, covering a solid angle of almost  $2\pi$  sr for stopped kaons in the gaseous target cell. These newly developed SDDs also allow a flexible arrangement around the cryogenic target cell, which enables one to perform the kaonic deuterium measurements at the two main kaon factories: DAΦNE and J-PARC.

##### b. Lightweight cryogenic target

For DAΦNE and J-PARC the same technique for producing the cryogenic target cells is used. The main component of both cells is the cylindrical wall, which consists of two layers of  $50 \mu\text{m}$  thick Kapton foils glued together with a two-component epoxy glue, with an overlap of 10 mm, achieving a total thickness of the order of  $140 \pm 10 \mu\text{m}$  with an x-ray transmission of 85% at 7 keV.

The final dimensions of the target cells depend on the machine used. DAΦNE supplies low momentum monochromatic kaons ( $127 \text{ MeV}/c$ ), so low thickness degrader, few mm plastic has to be applied to achieve a kaon stopping efficiency of almost 100%. In contrast, E57 uses kaons with momentum of  $660 \text{ MeV}/c$ , which need a kaon carbon degrader with a thickness of  $\sim 400 \text{ mm}$  to achieve a kaon stop efficiency of  $\sim 2\%$ .

Finally, it turns out that a gas density for SIDDHARTA-2 and E57 of 3% and 4% of the liquid deuterium density, respectively, will be optimal. Therefore, the dimensions of the target cells are quite different: for SIDDHARTA-2 the diameter of the cell is 145 mm with a height of 130 mm, while for E57 a diameter of 60 mm and a length of 190 mm were found to be optimal; see Fig. 34.

##### c. The SIDDHARTA-2 veto system

Two special veto systems are foreseen for SIDDHARTA-2, consisting of an outer barrel of scintillator counters, read by photomultipliers (PMs), called Veto 1 and an inner ring of plastic scintillation tiles (SciTiles), read by silicon photomultipliers (SiPMs), placed as close as possible behind the SDDs, for charge particle tracking, called Veto 2; see Fig. 35.

*The Veto-1 device:* It will be used to suppress fluorescence x rays produced by the direct stops of kaons in the target entrance window or in the vacuum chamber materials.

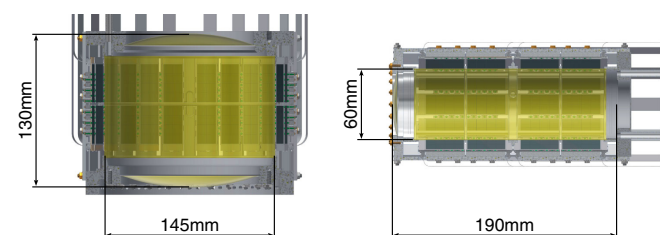


FIG. 34. Sketch of the (left) SIDDHARTA-2 and the (right) E57 cryogenic target cells.

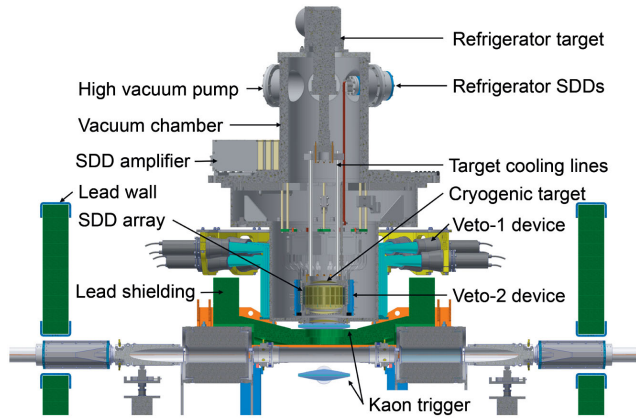


FIG. 35. The SIDDHARTA-2 setup with the cryogenic target cell surrounded by the SDDs and the Veto-2 system within the vacuum chamber, while the Veto-1 device is surrounding the chamber on the outside.

Once a  $K^-$  is stopped in the target gas, it is captured by the gas atoms and undergoes an atomic cascade (or decay), with radiative and nonradiative transitions, until it is absorbed by the deuteron. Most of the channels include a charged pion. The emitted pion has enough energy to pass through the SDD cooling system, the electronics, and the vacuum chamber, reaching the scintillator barrel of the Veto-1 system placed around the setup. The same is valid for pions generated by kaons absorbed in other materials of the setup. Based on the relatively long time that a kaon needs to stop in the target gas before it gets absorbed, compared to the short time in a solid (e.g., in the entrance window of the target or in the vacuum chamber) one can realize a veto counter by using this time information. The Veto-1 system allows one to separate these two types of events: kaons stopped in gas from kaons stopped in setup materials.

*The Veto-2 device:* The kaons stopped inside the deuterium target produce, together with the kaonic deuterium x rays, many charged particles, mostly pions, coming from the interactions of kaons with the deuteron following the nuclear absorption. While the kaonic deuterium x rays are very rare (due to the small yield) the charged particles are abundant, since each kaon produces them following the absorption. These charged particles can deliver signals in SDDs in the same energy range as the x rays of kaonic deuterium (see below), representing an important background source to be identified and eliminated. The absorption time is so fast that it is not possible to separate these two kinds of events using time information. One can, however, veto the unwanted signals by considering the spatial correlations between SDDs and hits in the scintillator tiles placed behind them.

In principle, four different cases can be considered for a charged particle passing through, or close to, a SDD cell.

Case 1: charged particles (pions) passing through the active area of the SDDs, depositing large charge on their way, producing a signal of about 150 keV, far above the region of interest (5–15 keV).

Case 2: charged particles passing through the edge of a SDD cell, depositing only a small energy, producing a signal in the region of interest.

Case 3: charged particles passing through the ceramic or cooling bar of a SDD cell, producing a “delta ray,” which might produce a signal in the region of interest.

Case 4: charged particles producing an x ray or an electron in the material surrounding the SDDs (e.g., the vacuum chamber), which might be backscattered and produce a signal in the region of interest.

Although case 1 is most likely, the cases 2 to 4 will contribute to a severe background in the region of interest. Let us point out that only about 0.1% of the stopped kaons will reach the  $1s$  ground state and produce an x ray. Dedicated Monte Carlo studies (using GEANT4) have shown that Veto 1 and Veto 2 are essential to perform a successful measurement and reduce the background by a factor of approximately 10.

#### d. The E57 veto system

For E57 at J-PARC, a charged particle tracking system, the cylindrical detector system (CDS), available from the E15 experiment (Hashimoto *et al.*, 2015) is used as the veto system.

The CDS consists of a solenoid magnet, a cylindrical drift chamber (CDC), and a cylindrical detector hodoscope (CDH). The CDC is a cylindrical wire drift chamber with 15 layers of anode wires, with an efficiency of over 99%. The outer radius of the CDC is 530 mm, the inner radius is 150 mm, and the total length is 950 mm, with a solid angle coverage of 66% of  $4\pi$ . The typical intrinsic resolution is of 200  $\mu\text{m}$ . The CDH is a segmented plastic scintillation counter used for the charged particle trigger and particle identification and is located at a radial distance of 544 mm from the beam axis with a solid angle coverage of 59% of  $4\pi$ . The CDH consists of 36 scintillator bars type Eljen EJ-200, with a length of 790 mm, a width of 99 mm, and a thickness of 30 mm. The scintillation light is read out by a pair of Hamamatsu photomultipliers (R7761 fine-mesh, 19-dynode, diameter 1.5 in.). The measured average time resolution (FWHM) of the CDH without a magnetic field is  $170 \pm 7$  ps, obtained with cosmic ray data.

The CDC allows one to apply a fiducial volume cut, selecting only those events which have their origin within the gas volume of the target, while the CDH is used in the trigger scheme for E57 (second-level trigger).

## 2. The SIDDHARTA-2 experiment at DAΦNE

SIDDHARTA-2 is a new experiment, which will be installed on DAΦNE in the spring of 2019, taking advantage of the experience gained in the previous SIDDHARTA experiment on kaonic hydrogen (Bazzi *et al.*, 2011a) and kaonic helium (Bazzi *et al.*, 2009, 2011c, 2012a). The goal of the new apparatus is to drastically increase the signal-to-background ratio, by gaining in solid angle, by taking advantage of the new SDDs with improved timing resolution, and by implementing additional veto systems.

In summary, the final SIDDHARTA-2 apparatus has required the development of novel SDD chips with on-board preamplifiers. In parallel, a new ASIC chip, called SFERA, was developed by Politecnico di Milano for multiplexing 16 SDD channels. Two new veto systems have been added.

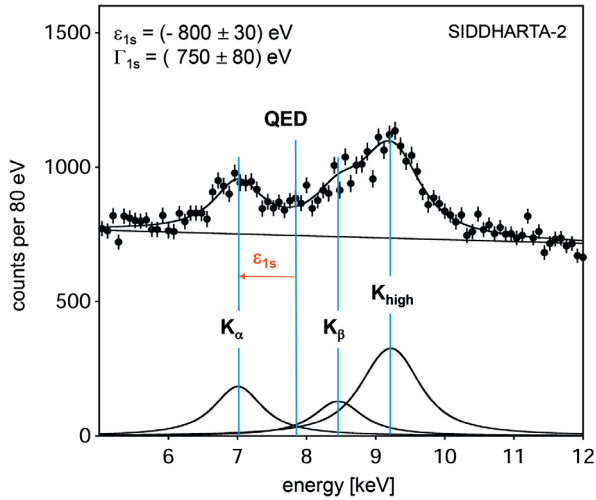


FIG. 36. Simulated SIDDHARTA-2 kaonic deuterium spectrum, assuming a shift  $\varepsilon_{1s} = -800 \pm 30$  eV and width  $\Gamma_{1s} = 750$  eV of the  $1s$  state, as well as a  $K_\alpha$  yield of  $10^{-3}$ . The spectrum was simulated for an integrated luminosity of  $800 \text{ pb}^{-1}$ .

Figure 35 shows the SIDDHARTA-2 apparatus. A detailed Monte Carlo simulation was performed within the GEANT4 framework to optimize the critical parameters of the setup, like target size, gas density, detector configuration, and shielding geometry. The Monte Carlo simulation took into account the described improvements with the assumption that the values of shift and width of the  $1s$  ground state of kaonic deuterium were  $-800$  and  $750$  eV, respectively, as representative theoretical expected values (see Table VIII). Moreover, yield ratios  $K_\alpha : K_\beta : K_{\text{total}}$  were those of kaonic hydrogen, with an assumed  $K_\alpha$  yield of  $10^{-3}$  (see Sec. IV.C.2).

Figure 36 shows the expected spectrum for an integrated luminosity of  $800 \text{ pb}^{-1}$  delivered by DAΦNE in similar machine background conditions as in SIDDHARTA runs. The extracted shift and width can be determined with precisions of about 30 and 80 eV, respectively. These values are of the same order as the SIDDHARTA results for kaonic hydrogen.

### 3. The E57 experiment at J-PARC

The E57 experiment will be performed in 2020 at the K1.8BR kaon beam line at J-PARC, using the K1.8BR multipurpose spectrometer—which includes as the main part the CDS—and the newly developed SDDs for x-ray detection in SIDDHARTA-2, surrounding a cryogenic target cell. The K1.8BR multipurpose spectrometer has been described in detail by Agari *et al.* (2012).

The cryogenic target cell surrounded by SDDs is placed in the center of the CDS (Fig. 37), with a total SDDs active area of  $246 \text{ cm}^2$ . The setup allows the tracking of the incoming kaons with segmented plastic scintillators, used also as start counters, and a beam line chamber. The charged particles produced in the kaon absorption on nuclei are tracked by the large CDC, while the CDH is used as a trigger in coincidence with the start counters.

Detailed Monte Carlo studies (GEANT4) have been performed to optimize the kaon stops in a gaseous target, taking

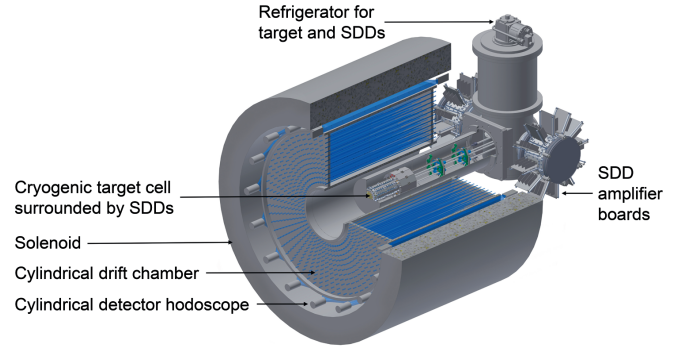


FIG. 37. Layout of the E57 setup with the cylindrical spectrometer system within a 0.7 T solenoid and in the center the cryogenic target with the novel SDD arrays.

special care of the large degrader thickness of 400 mm carbon for a  $660 \text{ MeV}/c$  kaon beam. The kaonic deuterium x-ray spectrum was simulated, taking the yield ratios  $K_\alpha : K_\beta : K_{\text{total}}$  from the SIDDHARTA kaonic-hydrogen data, with an assumed  $K_\alpha$  yield of  $10^{-3}$ . For the strong-interaction induced shift and width,  $-800$  and  $750$  eV, respectively, were assumed (same assumption used for SIDDHARTA-2).

Figure 38 shows the expected spectrum for a beam time of four weeks and a proton beam power of 40 kW. The extracted shift and width can be determined with precisions of 40 and 110 eV, respectively.

## B. Ultrahigh precision x-ray kaonic atom spectroscopy

### 1. The E62 experiment at J-PARC

A novel, unprecedented high-resolution, x-ray detector system has been made available to the hadronic scientific community by the E62 Collaboration at J-PARC. The aim of the E62 experiment is a high-precision measurement of the shifts of the  $2p$  level of kaonic helium-3 and kaonic helium-4 atoms induced by the presence of the strong interaction.

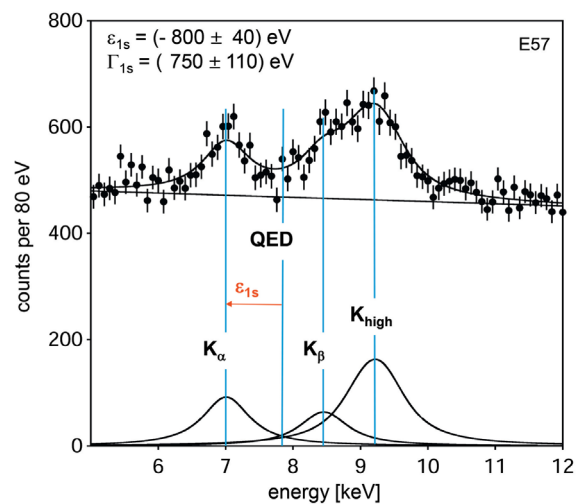


FIG. 38. Simulated E57 kaonic deuterium spectrum, assuming a shift  $\varepsilon_{1s} = -800 \pm 40$  eV and width  $\Gamma_{1s} = 750$  eV of the  $1s$  state, as well as a  $K_\alpha$  yield of  $10^{-3}$ .

Theoretically predicted values for the shifts of the  $2p$  state of kaonic-helium isotopes are

$$\varepsilon_{2p}(K^{-4}\text{He}) = -0.2 \text{ eV} \quad (36)$$

and

$$\varepsilon_{2p}(K^{-3}\text{He}) = +0.3 \text{ eV} \quad (37)$$

(Friedman, 2012).

On the experimental side (see Sec. IV.B), the most precise measurements up to now have been performed by the E570 experiment at KEK (Okada *et al.*, 2007):

$$\varepsilon_{2p}(K^{-4}\text{He}) = +2 \pm 2(\text{stat}) \pm 2(\text{syst}) \text{ eV}, \quad (38)$$

employing a liquid helium target and SDD detectors, and by the SIDDHARTA experiment at LNF-INFN (Bazzi *et al.*, 2009, 2011c):

$$\varepsilon_{2p}(K^{-4}\text{He}) = +5 \pm 3(\text{stat}) \pm 4(\text{syst}) \text{ eV}, \quad (39)$$

$$\varepsilon_{2p}(K^{-3}\text{He}) = -2 \pm 2(\text{stat}) \pm 4(\text{syst}) \text{ eV}, \quad (40)$$

employing gaseous helium targets and SDD detectors.

The scientific case is still open: the precision of the theoretical calculations is one-tenth of an eV, while the experimental accuracy is an order of magnitude worse.

An accurate experimental determination of the energy shifts of the  $2p$  level of kaonic-helium isotopes is then compelling. The required degree of precision is of the order of 0.2 eV or better. This precision might as well allow one to determine the sign of the level shift: upward or downward with respect to the electromagnetic value.

To achieve this precision, a breakthrough in detector technology is mandatory. SDD detectors reach at most an accuracy of  $\pm 2$  eV, with a resolution of about 150 eV (FWHM) at 6 keV (Okada *et al.*, 2007; Bazzi *et al.*, 2009, 2011c).

To deal with this request, a novel high-resolution cryogenic x-ray detector system was proposed by the E62 Collaboration (Bazzi, 2015). [This proposal was originally submitted as J-PARC E62 experiment (Precision Spectroscopy of kaonic atom x rays with TES).] The challenge was to obtain spectroscopic results with precision at the level of those obtained in measurements of pionic atom x rays using high-resolution wavelength dispersive Bragg crystal spectrometers (Gotta, 2004). Crystal spectrometers were not used for kaonic atom measurements, mainly due to their small detector acceptance, combined to orders of magnitude lower intensities  $K^-$  beams compared to  $\pi^-$  beams.

The E62 cryogenic detector system is based on an array of superconducting transition-edge-sensor (TES) microcalorimeters. TES is a highly sensitive thermal sensor that measures energy deposition via the increase in the resistance of a superconducting thin film that is biased within the sharp phase transition between the normal and superconducting phases (Irwin and Hilton, 2005; Ullom and Bennett, 2015). The typical energy resolution is as good as 2–3 eV (FWHM) at 6 keV (Smith *et al.*, 2012; Uhlig *et al.*, 2015), therefore corresponding to about 2 orders of magnitude better than that

of SDDs. On the other hand, only a small collecting area is available for a TES pixel (typically  $\sim 0.1 \text{ mm}^2$ ). Recent technological advances in multiplexed readout of multipixel TES arrays (more than 200 pixels) (Doriese *et al.*, 2016) allow for the performance of a precision kaonic atom measurement in a realistic data acquisition time.

The J-PARC E62 experiment employed a 240-pixel TES array developed by the National Institute of Standards and Technology (NIST) (Doriese *et al.*, 2017). Each TES consists of a bilayer of thin molybdenum and copper films. An additional  $4\text{-}\mu\text{m}$ -thick bismuth absorber is attached on each pixel, which has 80% detection efficiency for 6.5 keV x rays and covers an effective area of  $320 \times 300 \mu\text{m}^2$ . Thus, the total active area is approximately  $23 \text{ mm}^2$ . The TES array is cooled with a pulse-tube-backed adiabatic demagnetization refrigerator and is operated at 70 mK, slightly below the critical temperature. The 240 channels are read with eight time-division-multiplexing chips in parallel, at an effective sampling rate of 104 kHz. The digitized waveforms are streamed without any dead time, and only the self-triggered events are recorded.

In 2014, a pathfinding experiment was performed to demonstrate the feasibility of TES-based hadronic atom x-ray spectroscopy by measuring x rays from the  $4f \rightarrow 3d$  transition of pionic carbon  $\pi^-^{12}\text{C}$ . The experiment was performed at the  $\pi\text{M1}$  beamline of the Paul Scherrer Institute (PSI) using the same type of TES spectrometer used in E62 (Okada *et al.*, 2016).

A SDD was also installed as a reference and measured the pionic x rays with a FWHM energy resolution of  $\sim 165$  eV. The *in situ* energy calibration method was demonstrated by shining characteristic x rays excited by an x-ray tube source during the data acquisition. As a result, the averaged energy resolution achieved was 6.8 eV (FWHM) at 6.4 keV under a high-rate pion beam intensity of 1.45 MHz. The resulting systematic uncertainty in the  $\pi\text{-}^{12}\text{C}$   $4f \rightarrow 3d$  transition was less than 0.1 eV, so matching the E62 goal (Tatsuno *et al.*, 2016).

In 2016, a commissioning experiment was conducted at the secondary kaon beam line K1.8BR of the J-PARC hadron experimental facility, where the E62 experiment had to be installed. Optimization of the kaon beam and the degrader thickness in order to efficiently stop  $K^-$  in a target sample was successfully performed (Hashimoto *et al.*, 2017).

Finally, in 2018, the E62 experiment was carried out. Figure 39 shows the schematic view of the experimental setup. Incident  $K^-$ 's with momenta of 900 MeV/c were degraded in moderators and stopped in a cryogenic liquid helium-3 or helium-4 target, where the  $K^{-3}\text{He}$  or  $K^{-4}\text{He}$  atoms were generated.

The physics data taking of the E62 experiment was completed in June 2018. The  $3d \rightarrow 2p$  transition x-ray spectra for both  $K^{-3}\text{He}$  and  $K^{-4}\text{He}$  were successfully observed. At the moment of writing this paper, the data analysis is ongoing.

Precise *in situ* energy calibration was realized by shining six well-known calibration x-ray lines  $K_\alpha$  and  $K_\beta$  for Cr, Co, and Cu, using an x-ray tube source installed, as shown in Fig. 39, constantly during the data taking.

The expected performance of the TES at the J-PARC environment was studied using the GEANT4 toolkit.

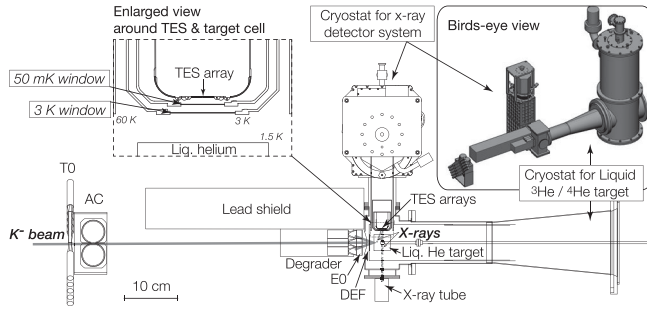


FIG. 39. A cross-section top view of the J-PARC E62 experimental setup. The inset shows a birds-eye view around TES and the helium target cell. A set of beam detectors, a cryogenic liquid helium-3 and helium-4 target system, and the NIST's TES x-ray spectrometer system are shown. From Okada, 2015.

Figure 40 shows the expected spectrum after the stopped kaons timing selection, assuming two weeks of data taking at 50 kW primary proton beam power. The continuous background in the figure is induced by accidental hits of the particles of the beam, by secondary particles from stopped kaon reactions, and by contamination from calibration x rays. Kaonic-helium x-ray lines could be clearly identified, and their energies could be determined with a statistical precision of about 0.2 eV.

Yamagata-Sekihara, Hirezaki, and Hiyam (2015) suggested that a high-precision measurement of the level shifts in the isotopes of kaonic helium might allow one to select between different versions of an antikaon-nucleus optical potential, namely, to resolve the question of the depth of the real part of the potential. A purely phenomenological potential of the “ $t\rho$ ” type, where  $\rho$  is the nuclear density and  $t$  is an effective amplitude (Friedman and Gal, 2007), are typically 180 MeV deep, while potentials constructed from more fundamental approaches are in the range of 40–85 MeV (Ramos and Oset, 2000). The depth of the potential may have far-reaching consequences for the possible existence of

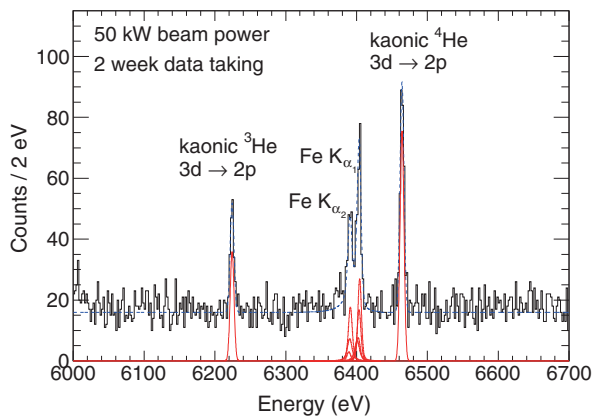


FIG. 40. Expected spectrum in the J-PARC E62 experiment. The red lines represent various x-ray components, and the blue dotted line represents a fit to the spectrum assuming as an example a constant background. From Okada, 2015.

kaon-nucleon clusters and the relation to kaon condensation in neutron stars (Akaishi and Yamazaki, 2002; Gazda *et al.*, 2007; Yamazaki and Akaishi, 2007; Gazda *et al.*, 2008, 2009).

With reference to the suggestion of Yamagata-Sekihara, Hirezaki, and Hiyam (2015) a warning has to be made. The proper framework to deal with optical potentials is experiments on medium-weight and heavier targets, since for a meaningful comparison using shifts and widths of the levels of kaonic-helium isotopes few-body approaches are required. Indeed, the progress in the field made recently by the Jerusalem-Prague Collaboration has given a substantial contribution to the study of the interaction of  $K^-$  mesons with hadronic systems, ranging from  $K^-$  atoms to  $K^-$ -nuclear clusters (Cieply *et al.*, 2011a, 2011b; Friedman, 2012; Friedman and Gal, 2012, 2013, 2017; Hrtankova and Mares, 2017).

Global analyses of kaonic atom experimental results along the periodic table were performed. The single-nucleon amplitudes, constrained by the kaonic-hydrogen SIDDHARTA results (Bazzi *et al.*, 2011a), were derived in several effective field theory SU(3) chiral-model approaches to  $S = -1$  meson-baryon interactions. To the single-nucleon part  $V_{K^-}^{(1)}$  of the  $K^-$ -nucleus optical potential was added a phenomenological isoscalar potential  $V_{K^-}^{(2)}$  of the form (Friedman and Gal, 2017)

$$2\mu V_{K^-}^{(2)}(\rho) = -4\pi B \left(\frac{\rho}{\rho_0}\right)^\alpha \rho, \quad (41)$$

where  $B$  is a complex strength,  $\alpha$  a positive exponent representing  $K^-$  multinucleon processes, and  $\rho_0 = 0.17 \text{ fm}^{-3}$ .

As an example, Fig. 41 (Friedman *et al.*, 2017) shows the real part of the  $K^-$  optical potential in Ni atoms, based on the Kyoto-Munich (KM)  $K^-N$  chiral-model amplitudes, augmented by a phenomenological amplitude  $B(\rho/\rho_0)^\alpha$ , for three values of the  $\alpha$  exponent, all providing good global fits to kaonic atom data. For comparison, a purely phenomenological potential (Friedman and Gal, 2007) is also shown in the figure.

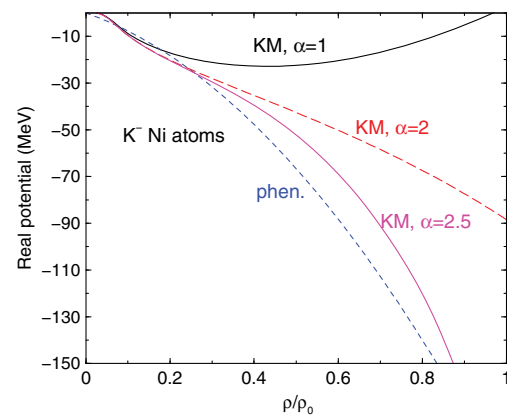


FIG. 41. Real part of the best fit  $K^-$ -Ni optical potential based on the single-nucleon amplitudes plus a phenomenological multi-nucleon amplitude  $B(\rho/\rho_0)^\alpha$ . Shown for comparison as short-dashed lines is a purely phenomenological potential (Friedman and Gal, 2007). Adapted from Friedman *et al.*, 2017.

Kaonic atom data probe the  $K^-$  optical potential reliably up to  $\sim 50\%$  of  $\rho_0$  at most. Hrtankova and Mares (2017) applied the Friedman-Gal (Friedman and Gal, 2017) optical potential to higher densities  $\rho \geq 0.5\rho_0$  by extrapolating  $V_{K^-}^{(2)}$ . The result was that the  $K^-$  multinucleon absorption gives rise to a substantial increase of the widths of the  $K^-$  states. The widths of the deeply bound kaonic nuclear states considerably exceed the  $K^-$  binding energies for  $A \geq 6$ . Therefore, observation of such states in experiments seems highly unlikely and limited to very light systems, such as  $K^-pp$ .

Kaonic atom data cover the whole periodic table with reasonable accuracy for shift and widths of the lower levels ( $n \leq 2$ ). However, as far as the upper levels are concerned, they are poorly known, being determined from the measured yields of the transitions to lower levels. This causes an increase of the error on top of the scarce accuracy of the yield measurements.

Therefore Friedman and Okada (2013) suggested to carry out new kaonic atom experiments on several carefully selected targets with an improved accuracy in determining both lower and upper level observables.

ATES-based detector can allow, for the first time, precision measurements of level widths due to strong interaction. Absorption is sufficiently strong in kaonic atoms to make it the dominant effect: the level widths are up to 1 order of magnitude larger than the corresponding level shifts. Furthermore, the shifts are almost universally of a repulsive type, although the real potentials required to fit kaonic atom data are of an attractive type. Hence the role of the real part is secondary to that of the imaginary part of the potential.

The level width which is usually obtained as the imaginary part of the complex eigenvalue when solving the Klein-Gordon equation with an optical potential is also related to the imaginary part of the potential as follows (Friedman and Okada, 2013):

$$\Gamma_{st} = -2 \frac{\int V_{\text{opt}} |\psi|^2 d\vec{r}}{\int [1 - (B + V_C)/\mu] |\psi|^2 d\vec{r}}, \quad (42)$$

where  $B$ ,  $V_C$ , and  $\mu$  are the  $K^-$  binding energy, Coulomb potential, and reduced mass, respectively. The widths are therefore the quantities which are more directly connected to the potential.

Discussions for dedicated experiments to measure the widths of selected kaonic atoms at DAΦNE are undergoing.

### C. Shift and width of the $1s$ state of kaonic helium-3 and kaonic helium-4

Up to now, only x-ray transitions to the  $2p$  level of kaonic helium-3 and helium-4 have been measured. No measurement of transitions to the fundamental  $1s$  level could be performed, mainly due to the extremely small yield expected for a kaon to reach the  $1s$  ground state and, in addition, to a much broader ground state level, as compared to the kaonic hydrogen and deuterium.

The use of the newly developed SDD detectors for SIDDHARTA-2 in coincidence with cadmium-zinc-telluride (CZT) semiconductor detectors, which have an efficiency of

100% for 30 keV x rays (expected energy of the  $K_\alpha$  line of kaonic helium), will drastically reduce the background and eventually allow one to measure the kaonic-helium transitions to the  $1s$  level. The SDDs will detect the  $L$  transitions and the CZT detectors will measure, in coincidence, the very rare  $K$ -transition x rays.

A possible setup might make use of the SIDDHARTA-2 apparatus in the following way: the diameter of the target cell will be increased to make space for additional rows of CZT detectors in between the SDD ones. Moreover, the whole exit window will be covered by CZT detectors. The solid angle, compared to that of SIDDHARTA-2, will be increased by 75%. Monte Carlo simulations are presently being performed for the optimization of the setup, while an experimental proposal at DAΦNE is being prepared.

The determination of the strong-interaction induced shifts and widths of the  $1s$  levels of kaonic helium-3 and helium-4 will provide fundamental information on the antikaon-nuclei interaction, complementing the kaonic-hydrogen and deuterium results.

## VI. CONCLUSIONS AND OUTLOOK

In this review the last 20 years of activities in experimental kaonic atoms physics, defining the modern era in this sector, are summarized. The aim is to present in a unique, compact framework the progress achieved by the broad international community working in this field and pushing forward this research by a continuous and tireless effort.

The physics of kaonic atoms is extremely broad and rich. The lightest kaonic atoms are the only “laboratory” where the strong interaction between kaons and nucleons at lowest energies can be measured, which allows one to extract the antikaon-nucleon isospin-dependent scattering lengths, key ingredients for all models and theories dealing with the low-energy QCD in systems with strangeness. This topic is a not yet fully understood sector, due to the lack of experimental data.

A better understanding of the QCD in strangeness sector at low energies contributes to unveil the mechanism of chiral symmetry breaking, which delivers the mass of almost all visible matter in the Universe. It is also important for shaping the equation of state for neutron stars, taking into account their possible strangeness content.

Kaonic atom studies are the key for a more complete understanding of our fundamental theory describing the way particles interact, giving birth to nuclei and stars. Experimental precision studies of kaonic atoms are, however, very challenging. The main challenge is the necessity to detect a weak signal over a large background. Increasing the signal-to-background ratio has required, on the one hand, the use of novel large area detectors with excellent timing and trigger capabilities, specifically the SDD, and, on the other hand, the use of pure cryogenic gaseous targets, which avoided the strong reduction of signals by the Stark effect. Only with these new techniques could the presented major results be achieved.

A further striking breakthrough in detector development has been recently obtained by the implementation of a new cryogenic detector based on an array of superconducting TES

microcalorimeters. TESs open a new scenario in x-ray high-resolution spectroscopy of hadronic kaonic atoms.

### A. Achievements in the modern era

The most significant achievements in the modern era of kaonic atoms measurements include the following:

*The solution of the kaonic-hydrogen puzzle*, solved by the KpX experiment at KEK and confirmed by the DEAR experiment at DAΦNE. A striking contradiction between the results of three old kaonic-hydrogen measurements and the bulk of the low-energy data concerned the sign of the  $1s$  level shift. A common feature, despite the low quality of the data, was that the sign of the shift and, consequently, that of the real part of the  $K^-p$  scattering length, was positive, which implied an attractive-type strong interaction, bringing to a downward level shift (more bound system). This was in contradiction with the results of the analyses of the low-energy data ( $K^-p$  cross sections for elastic and inelastic processes, branching ratios for  $K^-p$  absorption at rest, and  $\pi\Sigma$  invariant mass distributions), which found a negative real part of the scattering length, corresponding to a repulsive-type strong interaction, bringing to an upward level shift (less bound system).

The KpX experiment was the first experiment which employed a gaseous hydrogen target instead of a liquid one, so to reduce the Stark effect resulting in lower yields of the transitions. The KpX experiment succeeded in observing unambiguously, for the first time, a distinct  $K_\alpha$  x-ray peak. The sign of the  $1s$  level shift turned out to be negative, implying a repulsive-type strong interaction, in agreement with the low-energy data. This definitely swept out the long-standing kaonic-hydrogen puzzle.

The DEAR experiment at the DAΦNE collider of LNF-INFN utilized, like KpX, a gaseous pressurized cooled target and took advantage of the clean beam of monoenergetic kaons coming from the decays of  $\phi$  mesons produced in DAΦNE. The DEAR results confirmed the repulsive-type character of the  $K^-p$  strong interaction and could also identify, for the first time, the pattern of kaonic-hydrogen  $K$  lines, i.e., the  $K_\alpha$ ,  $K_\beta$ , and  $K_\gamma$  transitions.

*The most precise measurement of kaonic hydrogen* existing in literature was performed by the SIDDHARTA experiment at DAΦNE, providing strong constraints to theory. This was made possible by the use of new triggerable x-ray detectors, the silicon drift detectors, characterized by good energy and time resolutions, essential for the background suppression.

*Precise measurements of kaonic helium*: The  $5\sigma$  discrepancy between the experimental results for the  $3d \rightarrow 2p$  transition in kaonic helium, obtained in the 1970s and 1980s, and the theoretical calculations (a measured average of the  $2p$  level shift of about  $-40$  eV versus theoretical calculations around  $0$  eV) has been clarified by the precise measurements performed by the E570 and SIDDHARTA experiments, which found values in agreement with theory. In addition, SIDDHARTA measured, for the first time, the  $2p$  level shift in kaonic helium-3. Finally, SIDDHARTA measured also, for the first time, the widths of the  $2p$  level in kaonic helium-3 and kaonic helium-4.

*The first exploratory measurement of kaonic deuterium*: After performing the measurements of kaonic hydrogen and

kaonic helium-3 and kaonic helium-4, SIDDHARTA made a first exploratory measurement of kaonic deuterium. No evident signal corresponding to the  $K$ -series transitions was found. The upper limits for the total  $Kd$   $K$ -series yield and for the  $Kd$   $K_\alpha$  yield were obtained.

*The measurement of the  $K_\alpha$  yield and the  $K$ -series transitions yields in kaonic hydrogen*: The  $K_\alpha$  yield of kaonic hydrogen was measured, by the KpX and SIDDHARTA experiments, for the first time. The yields of the other  $K$ -series lines were measured by the SIDDHARTA, for the first time.

*The measurements of the  $K$ -series transition yields of kaonic nitrogen and of the  $L$ -series transitions yields of kaonic helium-3 and helium-4*: The transition yields of the  $K$ -series transitions of kaonic nitrogen and of the  $L$  series of kaonic-helium isotopes were obtained, for the first time, by DEAR and SIDDHARTA, respectively.

*The launch of a new detector to perform high-resolution spectroscopy*: The TES-based detector shows unprecedented performances with respect to those of the best silicon drift detectors:  $2$  eV (FWHM) resolution versus  $150$  eV (FWHM), and  $\pm 0.2$  eV precision versus  $\pm 2$  eV. It was successfully employed in the E62 experiment at J-PARC, which concluded the data taking in June 2018.

### B. Outlook

The great success of the modern era in measurements of kaonic atoms set the stage for future planned experiments, which were thought to be impossible to perform until recently. The new breakthroughs in technologies, pioneered by the kaonic atoms community, opened the way to a series of planned future experiments shortly summarized next.

#### 1. First measurement of kaonic deuterium

The kaonic deuterium x-ray measurement represents the most important experimental information missing in the field of the low-energy antikaon-nucleon interaction. Two dedicated measurements are planned, SIDDHARTA-2 at DAΦNE in 2019 and E57 at J-PARC in 2020.

The experimental challenge of the kaonic deuterium measurement is the very small kaonic deuterium x-ray yield, the even larger width, and the difficulty to perform x-ray spectroscopy in the high radiation environments of the two machines.

At DAΦNE and at J-PARC three crucial elements of the experimental setup have been developed: an innovative large area x-ray detector, consisting of new monolithic silicon drift detectors, with good energy resolution and reduced drift time; a dedicated veto system, to improve the signal-to-background ratio; and a dedicated cryogenic lightweight gaseous target system.

SIDDHARTA-2 and E57 aim to perform a kaonic deuterium measurement at a precision level similar to the existing kaonic-hydrogen one.

#### 2. Ultra-high-precision measurement of kaonic helium-3 and kaonic helium-4

The scientific case of the  $2p$  level shift in kaonic helium-3 and kaonic helium-4 is still open: the precision of the

theoretical calculations is at the level of the tenth of eV, while that of the best experimental measurements is at the level of  $\pm 2$  eV.

The E62 experiment at J-PARC has completed the data taking in June 2018. The experiment has employed the new cryogenic TES-based detector, with unprecedented performances, aiming to measure the kaonic helium-4  $2p$  level shift at 0.2 eV precision level.

### 3. First measurements of shifts and widths of the $1s$ state in kaonic helium-3 and kaonic helium-4

No measurements of transitions to the  $1s$  level in kaonic helium-3 and kaonic helium-4 have so far been performed.

The use of the newly developed SDD detectors employed in SIDDHARTA-2, in coincidence with CZT semiconductor detectors, will drastically reduce the background and eventually allow one to measure the kaonic-helium transitions to the  $1s$  level. An experimental proposal is being prepared at DAΦNE.

The modern era of precise kaonic atom measurements fostered a deeper understanding of the antikaon-nucleon and nucleus interactions at threshold, which is fundamental for unveiling the intimate mechanisms at work in the nonperturbative regime of the QCD theory.

The future measurements starting at the facilities delivering kaon beams promise to boost even farther our comprehension of the “strangeness physics,” with implications extending from particle and nuclear physics to astrophysics (the equation of state of neutron stars) with the aim to have a better understanding of how nature works.

### ACKNOWLEDGMENTS

We thank all of our colleagues from the KpX, DEAR, E570, SIDDHARTA, SIDDHARTA-2, E57, and E62 Collaborations. We also thank the KEK, DAΦNE (in particular, Catia Milardi and Mikhail Zbov), and J-PARC teams. Part of this work was supported by the Austrian Science Fund (FWF Grant No. P24756-N20), the Austrian Federal Ministry of Science and Research BMBWK 650962/0001 VI/2/2009, the Ministero degli Affari Esteri e della Cooperazione Internazionale, Direzione Generale per la Promozione del Sistema Paese (MAECI), the StrangeMatter project, the National Institute of Standards and Technology (NIST), and Grants-in-Aid for Scientific Research from MEXT and JSPS (No. 26707014).

### REFERENCES

- Agari, K., *et al.*, 2012, *Prog. Theor. Exp. Phys.* **2012**, 02B011.  
 Akaishi, Y., and T. Yamazaki, 2002, *Phys. Rev. C* **65**, 044005.  
 Bacher, R., P. Blum, D. Gotta, K. H. M. Schneider, J. Missimer, L. M. Simons, and K. Elsener, 1988, *Phys. Rev. A* **38**, 4395.  
 Bacher, R., *et al.*, 1989, *Phys. Rev. A* **39**, 1610.  
 Backenstoss, G., *et al.*, 1970, *Phys. Lett. B* **33**, 230.  
 Baird, S., *et al.*, 1983, *Nucl. Phys. A* **392**, 297.  
 Bamberger, A., *et al.*, 1970, *Phys. Lett. B* **33**, 233.  
 Batty, C. J., E. Friedman, and A. Gal, 1997, *Phys. Rep.* **287**, 385.  
 Batty, C. J., *et al.*, 1979, *Nucl. Phys. A* **326**, 455.  
 Bazzi, M., *et al.*, 2009, *Phys. Lett. B* **681**, 310.  
 Bazzi, M., *et al.*, 2011a, *Phys. Lett. B* **704**, 113.  
 Bazzi, M., *et al.*, 2011b, *Nucl. Instrum. Methods Phys. Res., Sect. A* **628**, 264.  
 Bazzi, M., *et al.*, 2011c, *Phys. Lett. B* **697**, 199.  
 Bazzi, M., *et al.*, 2012a, *Phys. Lett. B* **714**, 40.  
 Bazzi, M., *et al.*, 2012b, *Nucl. Phys. A* **881**, 88.  
 Bazzi, M., *et al.*, 2013, *Nucl. Phys. A* **907**, 69.  
 Bazzi, M., *et al.*, 2014, *Eur. Phys. J. A* **50**, 91.  
 Bazzi, M. (J-PARC E62 Collaboration), 2015, Updated proposal for J-PARC 50 GeV Proton Synchrotron: Precision Spectroscopy of Kaonic Helium  $3\ 3d \rightarrow 2p\ X$  rays [[http://j-parc.jp/researcher/Hadron/en/pac\\_1507/pdf/P62\\_2015-6.pdf](http://j-parc.jp/researcher/Hadron/en/pac_1507/pdf/P62_2015-6.pdf)].  
 Bazzi, M., *et al.*, 2016, *Nucl. Phys. A* **954**, 7.  
 Beer, G., *et al.* (DEAR Collaboration), 2005, *Phys. Rev. Lett.* **94**, 212302.  
 Bernardini, C., *et al.*, 1963, *Phys. Rev. Lett.* **10**, 407.  
 Bertuccio, G., *et al.*, 2015, *J. Instrum.* **10**, P01002.  
 Bianco, S., *et al.*, 1999, *Riv. Nuovo Cimento* **22**, 1.  
 Bird, P. M., *et al.*, 1983, *Nucl. Phys. A* **404**, 482.  
 Bombelli, L., *et al.*, 2011, *Nuclear Science Symposium and Medical Imaging Conference (NSS/MIC)* (IEEE, New York), p. 1972.  
 Bragadireanu, M., *et al.*, 2001, DEAR Technical Note IR-37.  
 Burbidge, G., and A. de Borde, 1953, *Phys. Rev.* **89**, 189.  
 Burleson, G. R., *et al.*, 1965, *Phys. Rev. Lett.* **15**, 70.  
 Camac, M., A. D. McGuire, J. B. Platt, and H. J. Schulte, 1952, *Phys. Rev.* **88**, 134.  
 Campbell, J. L., L. M. Donald, T. Hopman, and T. Papp, 2001, *X-Ray Spectrom.* **30**, 230.  
 Chatellard, D., *et al.*, 1997, *Nucl. Phys. A* **625**, 855.  
 Cieply, A., E. Friedmann, A. Gal, D. Gazda, and J. Mares, 2011a, *Phys. Rev. C* **84**, 045206.  
 Cieply, A., E. Friedmann, A. Gal, D. Gazda, and J. Mares, 2011b, *Phys. Lett. B* **702**, 402.  
 Conversi, M., E. Pancini, and O. Piccioni, 1945, *Phys. Rev.* **68**, 232.  
 Conversi, M., E. Pancini, and O. Piccioni, 1947, *Phys. Rev.* **71**, 209.  
 Davies, J. D., *et al.*, 1979, *Phys. Lett. B* **83**, 55.  
 Day, T. B., and G. A. Snow, 1960, *Phys. Rev. Lett.* **5**, 112.  
 de Borde, A., 1954, *Proc. Phys. Soc. London Sect. A* **67**, 57.  
 Deser, S., M. L. Goldberger, K. Baumann, and W. Thirring, 1954, *Phys. Rev.* **96**, 774.  
 Doriese, W. B., *et al.*, 2016, *J. Low Temp. Phys.* **184**, 389.  
 Doriese, W. B., *et al.*, 2017, *Rev. Sci. Instrum.* **88**, 053108.  
 Doring, M., and U. G. Meißner, 2011, *Phys. Lett. B* **704**, 663.  
 Egger, J.-P., D. Chatellard, and E. Jeannot, 1993, *Part. World* **3**, 139 [<http://inspirehep.net/record/1306971/files/part.world.3.1.139-147.pdf>].  
 Faber, M., *et al.*, 2011, *Phys. Rev. C* **84**, 064314.  
 Fermi, E., and E. Teller, 1947, *Phys. Rev.* **72**, 399.  
 Fiorucci, G., *et al.*, 1990, *Nucl. Instrum. Methods Phys. Res., Sect. A* **292**, 141.  
 Fitch, V., and J. Rainwater, 1953, *Phys. Rev.* **92**, 789.  
 Friedman, E., 2012, *Hyperfine Interact.* **209**, 127.  
 Friedman, E., and A. Gal, 2007, *Phys. Rep.* **452**, 89.  
 Friedman, E., and A. Gal, 2012, *Nucl. Phys. A* **881**, 150.  
 Friedman, E., and A. Gal, 2013, *Nucl. Phys. A* **899**, 60.  
 Friedman, E., and A. Gal, 2017, *Nucl. Phys. A* **959**, 66.  
 Friedman, E., A. Gal, A. Cieply, J. Hrtankova, and J. Mares, 2017, *Proceeding of Science*, arXiv:1711.11371.  
 Friedman, E., and S. Okada, 2013, *Nucl. Phys. A* **915**, 170.  
 Fry, W., 1951, *Phys. Rev.* **83**, 594.  
 Gal, A., 2007, *Int. J. Mod. Phys. A* **22**, 226.  
 Gallo, A., *et al.*, 2006, *Conf. Proc.* **C060626**, 607 [<http://accelconf.web.cern.ch/AccelConf/e06/PAPERS/MOPLS029.PDF>].

- Gatti, E., and P. Rehak, 1984, *Nucl. Instrum. Meth. Phys. Res.* **225**, 608.
- Gatti, E., and P. Rehak, 2005, *Nucl. Instrum. Methods Phys. Res., Sect. A* **541**, 47.
- Gazda, D., E. Friedman, A. Gal, and J. Mare, 2007, *Phys. Rev. C* **76**, 055204.
- Gazda, D., E. Friedman, A. Gal, and J. Mare, 2008, *Phys. Rev. C* **77**, 045206.
- Gazda, D., E. Friedman, A. Gal, and J. Mare, 2009, *Phys. Rev. C* **80**, 035205.
- Gotta, D., 2004, *Prog. Part. Nucl. Phys.* **52**, 133.
- Grant, C. E., *et al.*, 2004, *Proc. SPIE* **5501**.
- Hashimoto, T., *et al.*, 2015, *Prog. Theor. Exp. Phys.*, **2015**, 061D01.
- Hashimoto, T., *et al.*, 2017, *J. Phys. Soc. Conf. Proc.* **17**, 072001.
- Hauser, P., *et al.*, 1998, *Phys. Rev. C* **58**, R1869.
- Hirenzaki, S., Y. Okumura, H. Toki, E. Oset, and A. Ramos, 2000, *Phys. Rev. C* **61**, 055205.
- Horiuchi, W., *et al.*, 2017, arXiv:1712.09492.
- Horvath, D., and F. Entezami, 1983, *Nucl. Phys. A* **407**, 297.
- Hoshino, T., S. Ohnishi, W. Horiuchi, T. Hyodo, and W. Weise, 2017, *Phys. Rev. C* **96**, 045204.
- Hrtankova, J., and J. Mares, 2017, *Phys. Rev. C* **96**, 015205.
- Ikeda, Y., Tetsuo Hyodo, and Wolfram Weise, 2011, *Phys. Lett. B* **706**, 63.
- Ikeda, Y., Tetsuo Hyodo, and Wolfram Weise, 2012, *Nucl. Phys. A* **881**, 98.
- Iliescu, M., 2003, DEAR Technical Note IR-48.
- Iliescu, M., 2009, SIDDHARTA Technical Note IR-1.
- Irwin, K., and G. Hilton, 2005, Eds., *Cryogenic Particle Detection*, Topics Appl. Phys. (Springer, Berlin/Heidelberg), Vol. 99, pp. 63–152 [[https://link.springer.com/chapter/10.1007/10933596\\_3](https://link.springer.com/chapter/10.1007/10933596_3)].
- Ishiwatari, T., 2007, SMI Internal Report.
- Ishiwatari, T., *et al.*, 2004, *Phys. Lett. B* **593**, 48.
- Ishiwatari, T., *et al.*, 2006, *Nucl. Instrum. Methods Phys. Res., Sect. A* **556**, 509.
- Ito, T. M., *et al.*, 1998, *Phys. Rev. C* **58**, 2366.
- Iwasaki, M., *et al.*, 1997, *Phys. Rev. Lett.* **78**, 3067.
- Izycki, M., *et al.*, 1980, *Z. Phys. A* **297**, 11.
- Jensen, T., 2003a, DEAR Technical Note IR-46.
- Jensen, T., 2003b, DEAR Technical Note IR-45.
- Jensen, T., 2004, *Frascati Physics Series* Vol. XXXVI, pp. 349–354, DAΦNE 2004: Physics at meson factories—Frascati, June 7–11, 2004 [<http://inspirehep.net/record/672481/files/Frasc%20Phys%20Ser%2036%20349.pdf>].
- Jensen, T., and V. Markushin, 2003, *Lect. Notes Phys.* **627**, 37.
- Kim, J. K., 1965, *Phys. Rev. Lett.* **14**, 29.
- Koike, T., 2007, in preparation.
- Koike, T., T. Harada, and Y. Akaishi, 1996, *Phys. Rev. C* **53**, 79.
- Lechner, P., *et al.*, 1996, *Nucl. Instrum. Methods Phys. Res., Sect. A* **377**, 346.
- Markushin, V., 1994, *Phys. Rev. A* **50**, 1137.
- Martin, A. D., 1981, *Nucl. Phys. B* **179**, 33.
- Meißner, U. G., U. Raha, and A. Rusetsky, 2004, *Eur. Phys. J. C* **35**, 349.
- Meißner, U. G., U. Raha, and A. Rusetsky, 2006, *Eur. Phys. J. C* **47**, 473.
- Milardi, C., *et al.*, 2007, *2007 IEEE Particle Accelerator Conference (PAC)* (IEEE, New York).
- Milardi, C., *et al.*, 2009, *Int. J. Mod. Phys. A* **24**, 360.
- Mizutani, T., C. Fayard, B. Saghai, and K. Tsushima, 2013, arXiv:1211.5824.
- Okada, S., *et al.*, 2007, *Phys. Lett. B* **653**, 387.
- Okada, S., *et al.*, 2016, *Prog. Theor. Exp. Phys.* **2016**, 091D01.
- Patrignani, C., *et al.* (Particle Data Group), 2017, *Chin. Phys. C* **40**, 100001.
- Quaglia, R., *et al.*, 2015, *IEEE Trans. Nucl. Sci.* **62**, 221.
- Raeisi, M. G., and S. Z. Kalantari, 2009, *Phys. Rev. A* **79**, 012510.
- Raimondi, P., D. Shatilov, and M. Zobov, 2007, LNF-07-003-IR, arXiv:physics/0702033.
- Ramos, A., and E. Oset, 2000, *Nucl. Phys. A* **671**, 481.
- Russell, J. E., 1978, *Phys. Rev. A* **18**, 521.
- Sakitt, M., *et al.*, 1965, *Phys. Rev.* **139**, B719.
- Sako, H., 2010, *J. Power Energy Systems* **4**, 218.
- Sato, M., *et al.*, 2008, *Phys. Lett. B* **659**, 107.
- Shevchenko, N., 2012, *Nucl. Phys. A* **890–891**, 50.
- Siems, T., *et al.*, 2000, *Phys. Rev. Lett.* **84**, 4573.
- Smith, S. J., *et al.*, 2012, *J. Low Temp. Phys.* **167**, 168.
- Takahashi, H., *et al.*, 2015, *J. Radioanal. Nucl. Chem.* **305**, 803.
- Tatsuno, H., *et al.*, 2016, *J. Low Temp. Phys.* **184**, 930.
- Tomonaga, S., and G. Araki, 1940, *Phys. Rev.* **58**, 90.
- Trueman, T. L., 1961, *Nucl. Phys.* **26**, 57.
- Uhlir, J., *et al.*, 2015, *J. Synchrotron Radiat.* **22**, 766.
- Ullom, J. N., and D. A. Bennett, 2015, *Supercond. Sci. Technol.* **28**, 084003.
- Varidel, D., *et al.*, 1990, *Nucl. Instrum. Methods Phys. Res., Sect. A* **292**, 147.
- Vignola, G., *et al.*, 1996, *Conf. Proc. C930517* [<http://accelconf.web.cern.ch/AccelConf/e96/PAPERS/ORALS/TUX02A.PDF>].
- von Egidy, T., and F. J. Hartmann, 1982, *Phys. Rev. A* **26**, 2355.
- Wiegand, C. E., and R. H. Pehl, 1971, *Phys. Rev. Lett.* **27**, 1410.
- Yamagata-Sekihara, J., S. Hirenzaki, and E. Hiyam, 2015, private communication.
- Yamazaki, T., and Y. Akaishi, 2007, *Phys. Rev. C* **76**, 045201.
- Yao, W. M., *et al.* (Particle Data Group), 2006, *J. Phys. G* **33**, 1 [<http://pdg.lbl.gov/2006/>].
- Zmeskal, J., 2008, *Prog. Part. Nucl. Phys.* **61**, 512.
- Zobov, M., *et al.*, 2010, *Phys. Rev. Lett.* **104**, 174801.